

UC Berkeley

UC Berkeley Electronic Theses and Dissertations

Title

Cavity and Microwave Experiments on Electron Plasma

Permalink

<https://escholarship.org/uc/item/8wj8j69m>

Author

Hunter, Eric

Publication Date

2019

Peer reviewed|Thesis/dissertation

Cavity and Microwave Experiments on Electron Plasma

by

Eric Hunter

A dissertation submitted in partial satisfaction of the

requirements for the degree of

Doctor of Philosophy

in

Physics

in the

Graduate Division

of the

University of California, Berkeley

Committee in charge:

Professor Joel Fajans, Chair

Professor Jonathan Wurtele

Professor Philip Marcus

Fall 2019

Abstract

Cavity and Microwave Experiments on Electron Plasma

by

Eric Hunter

Doctor of Philosophy in Physics

University of California, Berkeley

Professor Joel Fajans, Chair

A new technique for rapidly generating a sequence of target plasmas in a Penning-Malmberg trap is presented and applied in the first demonstration of cavity-resonant cooling in a plasma [51, 76]. This “reservoir” technique further enables the *in situ* magnetic field to be measured to high precision by microwave ECR spectroscopy [50]. A precision antihydrogen gravity experiment being constructed at CERN will rely on this method, as there is no other method with comparable absolute, spatial, and temporal resolution which can be implemented in the Penning-Malmberg trap. These cavity and microwave measurements require accessing new regimes with the plasma parallel energy analyzer, to which end the sensitivity of the latter technique has been increased twenty-fold [52].

Contents

Contents	i
List of Figures	iii
List of Tables	vi
List of Symbols and Values for a Typical Plasma	vii
1 Introduction	1
1.1 The Berkeley Experiment	2
1.2 The ALPHA Experiment at CERN	3
2 Apparatus	5
2.1 Penning Trap	5
2.2 Electronics	10
2.3 Magnets	15
2.4 Vacuum	18
2.5 Cryogenics	24
3 Diagnostics	29
3.1 Imaging	30
3.2 Faraday Cup	31
3.3 Temperature Diagnostic	34
3.4 Photomultiplier	41
4 Plasma Reservoir	45
4.1 Hot Targets for Cavity Cooling	46
4.2 Cold Targets for Magnetometry	47
5 Cavity cooling	52
5.1 The Purcell Effect	53
5.2 Cooling in the Copper Cavity	54
5.3 Theoretical Advances	57

5.4	Cooling in the Titanium Cavities	64
5.5	Applications	78
6	Precision ECR Magnetometry	86
6.1	Initial Applications	86
6.2	Mapping the ALPHA Trapping Fields with the Reservoir Technique	88
6.3	Higher Order Effects	89
6.4	ECR in ALPHA-g	95
7	Distractions	98
7.1	Stimulating Longitudinal Waves	98
7.2	Monitoring the Slosh and Breathing Modes	104
7.3	Resistive Cooling	106
7.4	Mirror EVC	109
A	LabVIEW VI's	113
B	Historical Penning-Malmberg Trap Experiments	114
C	Electrode Potential Solver	116
	Bibliography	120

List of Figures

1.1	Electrode stack with source (right), plasma (middle), and detector (left)	2
2.1	Penning Malmberg traps at Berkeley	5
2.2	Cavity 1, Cavity 2, and Cavity 3	7
2.3	An electrode painted with colloidal graphite	8
2.4	Evidence for mode coupling between Cavity 1 and Cavity 3	9
2.5	Irises and the curve which justifies them	10
2.6	Faraday cage for electrode HV cable breakout	11
2.7	FFT's of the quiescent voltage on a typical electrode	12
2.8	Solidworks drawing of the MCP	14
2.9	Microwave horn and synthesizer	14
2.10	Dark box at the end of the experiment	14
2.11	Summary of RRR tests	16
2.12	Measurement of the cryogenic resistance of the gradient coil	16
2.13	Calculated field due to the gradient coil, verified using ECR	17
2.14	Superconducting solenoid reacting to the gradient coil	18
2.15	UHV assembly being prepared for insertion in the magnet bore	20
2.16	Solidworks model of the UHV, coldbar, and alignment carriage	21
2.17	Circuit analogy for a vacuum system	22
2.18	The most difficult joint in the experiment	26
3.1	Expansion curve for $N = 10^7$ electrons at $B = 0.3$ T	31
3.2	30 s egun emission characteristic	32
3.3	Filling the trap with 30 V of plasma	32
3.4	Using the biased MCP to count charge	33
3.5	Rule of thumb for the dump rate.	36
3.6	Extraction trace for a hot, $N = 3 \cdot 10^6$ e ⁻ plasma	38
3.7	Extraction trace for a cold, $N = 3 \cdot 10^6$ e ⁻ plasma	38
3.8	Expanded version of previous figure, showing temperature fit	38
3.9	Extraction trace acquired using original SiPM	43
3.10	Plasma images acquired while dumping slowly to measure the temperature	43
3.11	SiPM trace for 100 trapped electrons	44

4.1	Repetitive pulsed extraction from a positron plasma at UCSD	46
4.2	Sequence steps from the first reservoir sequence	47
4.3	Typical T, N for about 70 scoops from a hot reservoir	47
4.4	Sequence steps from a recent reservoir sequence	48
4.5	Parameters of the reservoir plasma after SDREVC	48
4.6	Typical T, N, r_p for 120 scoops from a cold reservoir	50
4.7	Target plasma L and λ_D found using the Poisson solver	51
5.1	The fill factor and measured cooling rate for low order modes in Cavity 2	54
5.2	Section view of the first cavity experiment	55
5.3	T vs. B near TE_{13x} in the original bulge	56
5.4	Plasma temperature for variable B and z at modes with nodes	57
5.5	Plasma temperature for variable B and t , cooling at TM_{031}	58
5.6	Graphical representation of the thermodynamic rate equations	60
5.7	Plasma-cavity overlap in the frequency domain	62
5.8	Mode splitting when the superradiant power approaches the cavity dissipation	63
5.9	Cooling at TE_{122} as a function of position and gradient	65
5.10	Three important well shapes for Cavities 1 and 2	65
5.11	Temperature vs. time at TE_{111} as a function of N , well shape, and ΔB	67
5.12	Cooling rate vs. spread in cyclotron frequencies	68
5.13	Cooling rates for $30 \cdot 10^6$ electrons compared to theory predictions	69
5.14	Illustration of an apparent temperature threshold	70
5.15	Motion of the knee in T vs. t for five different wellshapes	71
5.16	Plasma parameters L/λ_D and ω'_z determined at $T = T_{th}$ for five well shapes	71
5.17	Γ vs. N at TE_{121} in Cavity 1 and TE_{141} in Cavity 2	72
5.18	N dependence of the poorly understood cooling suppression	73
5.19	T vs. B at TE_{141} in Cavity 2.	73
5.20	T_f vs. N in Cavity 1 and Cavity 2	75
5.21	T_f vs. H for $7.5 \cdot 10^6$ electrons in Cavities 1 and 2	76
5.22	Complete magnetic field scan showing the mode structure for all three cavities	77
5.23	Cooling rate and final temperatures reached at 0.155 T in Cavity 2.	78
5.24	T vs. B at TE_{111} with variable gradient	79
5.25	TE_{111} in the cylindrical section downstream of Cavity 1	81
5.26	No-bulge resonances found near 1 T using the plasma modes diagnostic	81
5.27	Cavity resonances found in ALPHA-2 using the reservoir technique	83
5.28	Scanning through the TE_{14x} with the reservoir in ALPHA-2	84
6.1	Schematic of the Plasma Modes Diagnostic	87
6.2	The first ECR heating peak measured in the experiment	87
6.3	T vs. f for single plasmas exposed to microwaves in Cavity 2 at low field	88
6.4	Reservoir ECR compared to Modes ECR	89
6.5	Maps of the trapping fields in ALPHA-2	90

6.6	Broad microwave heating scan at 19.6 GHz	91
6.7	Rotation frequency scan for a needle-shaped plasma	92
6.8	Simultaneous ECR spectra for needle and pancake plasmas	94
6.9	Linear fits to the $m = 0, 1, 2$ peak locations in the simultaneous spectra	95
6.10	Chukman's cartoon of the magnetic bottle from which antihydrogen is to escape	95
7.1	Bounce resonant heating of a few million electrons	99
7.2	Plasma heating attributed to noisy Lakeshore 218 controllers	100
7.3	Induced noisy emission during temperature dump	101
7.4	Extraction traces showing effects of plasma rotation and electrode noise	102
7.5	Relaxation of non-thermal electrons	103
7.6	Cartoon comparing the dipole (slosh) and quadrupole (breathing) modes	105
7.7	Observed correlation between dipole frequency and number of plasma electrons	105
7.8	Schematic of the LRC circuit	107
7.9	Calculated fraction of current which flows through the parallel resistor	107
7.10	Mock-up electrode-inductor tank circuit	108
7.11	Transfer function of the mock-up tank circuit	108
7.12	Finding the LRC resonance with Modes.vi	109
7.13	Cartoon of a plasma being evaporatively cooled under a magnetic field gradient	111
7.14	Experimental demonstration that EVC works better using a gradient	111
C.1	How to calculate the potentials due to finite length electrodes	117
C.2	Block diagram of the analytic potential calculator	118
C.3	LevMar fits using 5 flat electrodes to model Cavities 1 and 2	119

List of Tables

1.1	ALPHA's results with antihydrogen	3
2.1	Bulge geometry	8
2.2	Properties of the wire used for the gradient coil	15
2.3	Standard vacuum conductance formulae	22
2.4	Heat budget for the cold UHV	27
2.5	Shrink budget for the UHV	28
3.1	Properties of the PCO Sencam	31
3.2	Typical parameters for charge measurement with the Faraday cup	33
5.1	Comparing TE_{121} in Cavity 1 and TE_{141} in Cavity 2	73
6.1	Numerical results for representative target plasmas from Fig. 6.8	93
7.1	Estimated LRC circuit parameters for resistive cooling	108
7.2	Measured target plasma parameters suggesting a Mirror-EVC effect	110
B.1	Normal modes of a pure electron plasma	114

List of Symbols and Values for a Typical Plasma

B	Magnetic Field	1 T
ν	Parallel collision rate	$5 \cdot 10^4 \text{ s}^{-1}$
$\nu_{\perp\parallel}$	Anisotropy relaxation rate	$8 \cdot 10^3 \text{ s}^{-1}$
N	Number of electrons	10^6
n	Number density	$5 \cdot 10^7 \text{ cm}^{-3}$
T	Temperature	100 K
ω_r	Rotation frequency	$2\pi \cdot 400 \text{ kHz}$
ω_z	Bounce frequency	$2\pi \cdot 10 \text{ MHz}$
ω_p	Plasma frequency	$2\pi \cdot 60 \text{ MHz}$
ω_c	Cyclotron frequency	$2\pi \cdot 28 \text{ GHz}$
r_w	Electrode radius	20 mm
r_p	Plasma radius	1 mm
L	Plasma length	10 mm
λ_D	Debye length	0.1 mm
r_L	Larmor radius	0.0002 mm
b	Distance of closest approach	0.0002 mm
v_t	Thermal velocity	$4 \cdot 10^4 \text{ m s}^{-1}$
v_z	Parallel velocity	10^5 m s^{-1}

Chapter 1

Introduction

This thesis extends the work on pure electron plasmas initiated by Malmberg [62] to include new regimes in parameter space where tests may be performed at a level of precision with few precedents in plasma physics (10^{-8}). As is typical in these devices, a superconducting solenoid provides a field $B\hat{z}$ such that the plasma electrons circulate in the x - y plane close to the trap axis, while bouncing axially within the electric potential valley $V(r, z, t)$ determined by the voltages applied to a series of cylindrical electrodes. The plasma can be split (Chapter 4), cooled (Chapter 5), and heated (Chapter 6). One can measure the plasma shape, the number of electrons and their temperature (Chapter 3), as well as the energy distribution and mode structure (Chapter 7).

This thesis presents tools for obtaining and diagnosing cryogenic electron plasmas in regimes previously inaccessible. In particular, the work includes

1. increasing the sensitivity of the parallel energy analyzer to detect the energies of single plasma electrons,
2. using this sensitivity to extend the range of the temperature diagnostic to plasmas with several orders of magnitude fewer electrons than it was previously possible to diagnose,
3. cooling 10^6 electrons to wall temperature at 0.155 T,
4. cooling the same number of electrons at 0.962 T at a rate of 4.1 s^{-1} , eighteen times faster than the free-space cooling rate at that field,
5. rapidly producing sequences of 120 “pancake” plasmas (from a single reservoir plasma) which skirt the plasma regime despite containing only 10^3 electrons,
6. using these plasmas to perform magnetic field diagnostics to a relative precision of $2.5 \cdot 10^{-8}$.

1.1 The Berkeley Experiment

The above results were obtained in an experiment at Berkeley dedicated to Cold electron Research (CeRes) [76]. The blue arrows and blue ellipse in Fig. 1.1 represent the flow during a typical experimental cycle. First a BaO-coated disk is heated by flowing about 1 A through a 1 Ω tungsten filament. Free electrons stream from the surface into the experiment forming something like a sabre. The end of the sabre is pinched off and the current to the source is extinguished. What remains is a plasma, in the shape of a 1 mm-thick cigar, rotating rigidly. The electrons in the plasma bounce along the z axis and orbit their gyrocenters at the cyclotron frequency, the highest frequency to which the plasma is sensitive ($\omega_c/2\pi \sim 10$ GHz). Although the cyclotron motion is very small ($r_L \sim 1 \mu\text{m}$), it is very efficient at absorbing microwave radiation: a 1 ms, 1 mW pulse of microwaves can heat the plasma from 100 up to 10,000 K (Chapter 6). The presence of a cavity changes the set of microwave radiation patterns which can appear in the experiment. Perhaps surprisingly, this can greatly increase the spontaneous emission rate, cooling the plasma faster and to a lower final temperature (Chapter 5).

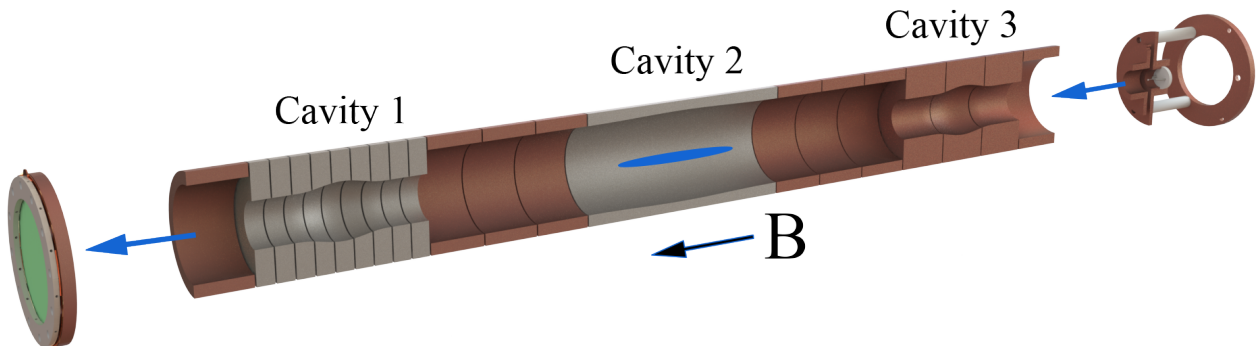


Figure 1.1: Electrode stack with source (right), plasma (middle), and detector (left)

At the end of each cycle the plasma is dumped out onto an electron amplifier, the microchannel plate (MCP). The MCP is followed by a phosphor screen, which converts the incident electron signal into light. If an image of the plasma is desired, the dump is fast ($5 \mu\text{s}$). The light signal is recorded by a fast camera to obtain a z -integrated density profile $n(r)$. If the plasma temperature is desired, the dump is slow (100 ms). A photomultiplier counts each arriving electron via the approximately 100 photons it produces in the phosphor screen. By looking at how many electrons escape as a function of how low the potential on the downstream gate has fallen, one can reconstruct the energy distribution $f(E)$, and thus find the temperature, T , of the plasma. These diagnostics are described in more detail in Chapter 3.

1.2 The ALPHA Experiment at CERN

The ALPHA (Antihydrogen Laser Physics Apparatus) experiment is the immediate beneficiary of the work at Berkeley. Several of the innovations described in this thesis have already been implemented at CERN, and more are envisioned for the next run. ALPHA performs precision measurements comparing antihydrogen to hydrogen.¹ These include charge neutrality, microwave spectroscopy, and laser spectroscopy tests of standard model predictions² at the 10^{-6} to 10^{-12} level (Table 1.1). The reservoir-ECR method developed at CERN as part of this thesis work permits independent, fast, in-situ mapping of the magnetic field and microwave intensity, which will contribute to the uncertainties in such spectroscopy figures.

Measurement	Relative Precision
1s-2s transition	$2 \cdot 10^{-12}$
1s-2p transition	$5 \cdot 10^{-8}$
Hyperfine splitting	$4 \cdot 10^{-4}$
Antihydrogen charge	$7 \cdot 10^{-10}$

Table 1.1: ALPHA’s results with antihydrogen

These results have been published in Nature [2, 3, 6, 5].

In 2018 the author participated in the construction of ALPHA-g, a new experiment oriented vertically so the antihydrogen can be released into free fall and travel the greatest distance possible before encountering matter and annihilating. The distribution of annihilation locations can be used to infer the gravitational coupling, m_g , which pulls antihydrogen either towards the earth or away from it. Unlike the previous experiments which *benefit* from reservoir ECR, ALPHA-g can *only* operate at its design precision of $\delta m/m < 1\%$ with this method of measuring the field $B(z, t)$. This is because the antihydrogen is to be released by reducing the 1 T mirror fields above and below it to zero in only one minute. To map such fields requires

- i Many measurements per second, because of the 100 s rampdown time
- ii Very short plasmas, because of the ~ 1 T/10 cm gradient

¹To date, ALPHA has not attempted to repeat its antihydrogen measurements with ordinary hydrogen in the same or a similar trap, relying instead on simulations and accepted values from other experiments.

²The quantum Lagrangian density, an expression describing something like the energy of the known elementary particles in various circumstances, is mathematically identical with itself after inverting space, time, and the signs of the particles’ charges. The assertion that any acceptable (i.e. local, Lorentz invariant, and unitary) theory has this property is called the CPT theorem (Charge, Parity, Time). If antihydrogen were found to be in any way different from hydrogen, the CPT theorem would be invalidated, and the standard model would have to be revised.

- iii Understanding of the resulting bounce structures
- iv 10^{-6} precision ($\delta B/B$) at the escape points.

The reservoir method is able to meet these requirements. No other scheme exists which would satisfy any of them.

All of ALPHA's experiments require that the antihydrogen formed by combining positron and antiproton plasmas be trapped in a 0.5 K ($50 \mu\text{eV}$) magnetic bottle³ Antihydrogen formed from antiprotons with greater energy escapes immediately. Despite years of optimization and a nearly 5 K trap, ALPHA plasmas are seldom less than 15 K *after* evaporative cooling, and 99.9% of the antiatoms escape as soon as they are formed.

Alex Povilus built the original cold electron plasma experiment at Berkeley with an intention to investigate the possibility that colder plasmas might be obtained by increasing the cooling rate. His quantum mechanical model predicted that if the electrode stack were capped to form a closed cylindrical cavity and the magnetic field adjusted so that the electron cyclotron frequency $\omega_c = \omega_\lambda$, a natural frequency of the cavity, the electrons in the plasma would radiate much faster. The truth as well as the limitations of this conjecture have been thoroughly catalogued (Chapter 5), and there is little doubt that this technology would greatly increase the antihydrogen trapping rate if installed in ALPHA-g.

³ $\boldsymbol{\mu} \cdot \mathbf{B} \approx 50 \mu\text{eV}$ for the positron magnetic moment $\mu \approx \mu_B$ and $B \approx 1 \text{ T}$.

Chapter 2

Apparatus

The machine used in the majority of this work was first commissioned by Alex Povilus for studying plasma cooling in a conducting cylinder with magnetically operable endcaps [76]. Later the electrode stack was modified to include a set of electrodes shaped more like a standard radiofrequency cavity and not requiring endcaps [31]. Following the development of the method described in Chapter 4, cavity resonant cooling of a plasma was observed for the first time under those electrodes [77]. These preliminary observations led to the design of two new cavities, along with sweeping upgrades to the cooling, electronic, and vacuum systems which could proceed in parallel with the machining of the titanium cavities.

In addition to describing these improvements, this chapter is intended to be a resource for the next operator of the experiment. It includes some non-essential details such as supplier names, locations of sensors, rules of thumb, and references to technical data.

2.1 Penning Trap

The electrode stack (Fig. 2.1) is the part of the experiment which the plasma sees. It must be a clean, cold, and electrically quiet place if the plasma is to relax to a low temperature equilibrium. By

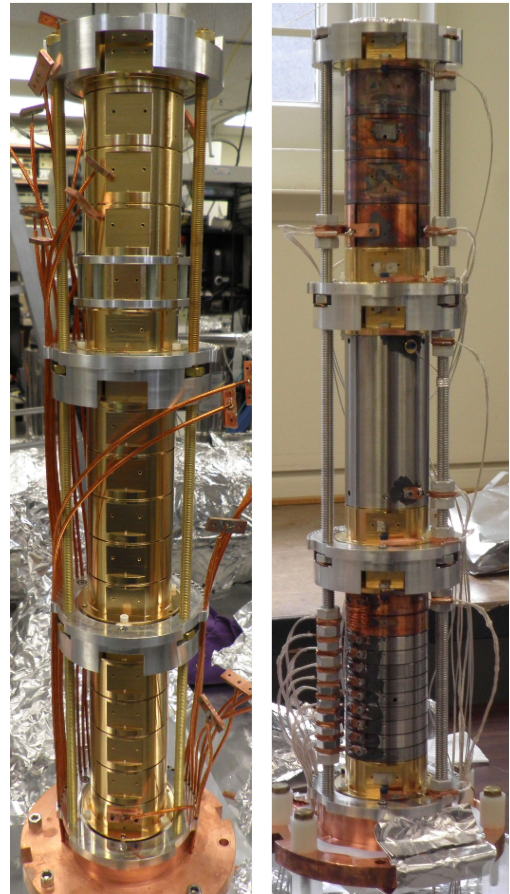


Figure 2.1: Penning Malmberg traps at Berkeley. Left: original version (2013) of the electrode stack. Right: final version (2016) prior to insertion.

“clean” is meant both that the electrode walls must contain no dust or other charge-trapping impurities (Section 2.1), and that the system must be able to be completely evacuated of residual gas (Section 2.4). Some experiments achieve electrode temperatures around 4 K by enclosing their electrode stack in a tight-fitting metal envelope surrounded by liquid helium. The electrodes cool via conduction through copper wires and bars leading to a 4 K refrigerator (Section 2.5). To reduce unwanted noise appearing on the electrode voltages used to manipulate the plasma, very slow high-voltage amplifiers have been introduced ($RC \sim 10$ ms). In addition, thorough investigations of noise sources and shielding in the lab have been performed (Section 2.2).

Microwave Cavities

Even an open metal pipe supports standing waves or “normal modes.” As in optics, the abrupt change in impedance at the pipe exit reflects the waves, causing those with the right spatial frequency to interfere constructively, accumulating wave power in the pipe at a regularly spaced set of loci called “antinodes.” Early experiments by Dehmelt et al. [40] showed that a single electron radiates much faster when the electron is gyrating at the same frequency as one of these normal modes.

Alex Povilus wanted to try this with a plasma. Dehmelt used a closed, hollow cylinder for increasing the quality factor (Q) of the modes, but that design is incompatible with many Penning trap experiments, particularly ALPHA, which requires transport of charged particles between different trap stages, often separated by several feet for the purpose of isolating vacuums and electronics. Alex proposed adapting the magnetically operable “flappers” which the group had recently begun testing for keeping microwaves *out* of the atom trap at CERN. These could in principle close the ends of the electrode stack, forming a high- Q cavity, whenever particles didn’t need to pass through [76]. Unfortunately, the design suffered numerous setbacks. The large amount of current required to actuate the flapper led to burnt out leads and excessive heat in the cryogenic vacuum. The eddy currents were not properly accounted for and led to long closing time and incomplete closing and opening.

Concurrent with frustrating flapper R&D, collaborators at the University of British Columbia offered a low-tech solution: go back to the open pipe model, but with a gradual bulge carved into the inner surface of the electrodes [32]. As reflection is then accomplished over several wavelengths, less power is mixed into propagating (TEM) modes, and the quality factor is increased. As shown in Fig. 2.2, the mode can be entirely trapped in this way.

Figure 2.2 displays a section view of the bulged cavities. Cavities 1 and 2 were cut from grade 5 titanium alloy with a resistivity $\rho \approx 1.5 \cdot 10^{-6} \Omega \text{ m}$ at 10 K. Cavity 3 is made of copper. To increase its cryogenic resistivity, collaborators at the University of British Columbia (UBC) electroplated the inner surface using an axial wire source with a nichrome-like colloidal suspension. Their method was found to produce a $1 \mu\text{m}$ thick layer of amorphous Ni_xCr_x , corresponding to $\rho \approx 1.5 \cdot 10^{-6} \Omega \text{ m}$ for microwaves having frequency 10 GHz or higher. Lower frequency waves can reach the cryogenic copper underneath, where

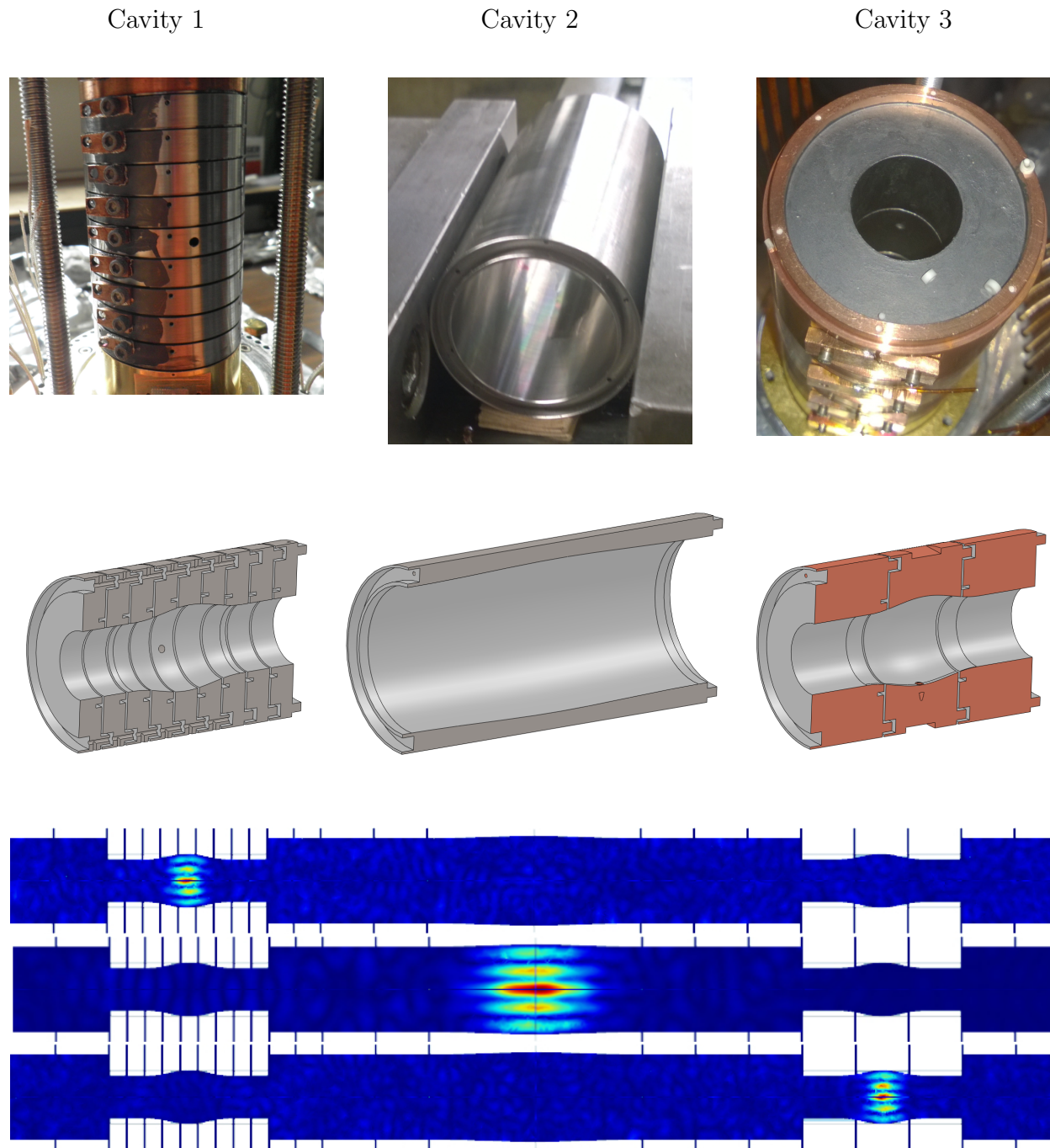


Figure 2.2: Cavity 1, Cavity 2, and Cavity 3. Photos were taken in 2016. Solidworks renderings use a paler gray to suggest the colloidal graphite antistatic coating, visible in the photo of Cavity 3. At the bottom TE_{131} is displayed for each cavity as simulated in COMSOL. Simulated frequencies 34.127, 19.592, 34.000 GHz respectively. While COMSOL nominally treats the space between the electrodes (blue combs, most noticeable above and below Cavity 1) the same as the space inside the trap, it seems to struggle at the corresponding 1 mm length scale.

charges can circulate with negligible dissipation ($\rho < 10^{-9} \Omega \text{ m}$)¹. The bulge profile is a simple cosine curve; see Table 2.1.

In 2015, with only the copper cavity (now called Cavity 3) installed, the cooling enhancement was found to depend strongly and non-intuitively on the position and length of the plasma with respect to the cavity mode. This motivated the design of the short gray cavity, Cavity 1. Its $\frac{1}{3}$ " long electrodes² permit a complete position scan with plasmas as short as 5 mm (compared to 20 mm or more in the copper cavity). While Cavity 1 was being machined, Nathan Evetts and Walter Hardy were prototyping the four inch long “thinwall” cavity, Cavity 2, at the engineering shop at UBC. This cavity has very low δr , which is important for compatibility with ALPHA’s electrodes³ and very high $\frac{l}{\delta r}$, which COMSOL and HFSS simulations suggest leads to very effective mode trapping at frequencies above about 10 GHz. Nathan has confirmed the general trend with real models [32].

Each cavity is also given an antistatic coating made of colloidal graphite particles suspended in alcohol⁴. The colloidal graphite solution may be applied with a fine paint brush, resulting in a completely opaque layer which is yet only a few microns thick when measured with a dial indicator on the milling machine. This is also the scale of minor imperfections in the paint job; see Fig. 2.3. Given that no flaking has been observed, even after cryogenic cycling and removal from the trap (top right panel of Fig. 2.2), it seems advisable to err on the side of too thick rather than too thin a coat.

The microwave mode structure of Cavity 3 was thoroughly investigated by UBC collaborators using simulations and transmission measurements through the ports. This work is described in Ref. [32]. They found that putting ports into Cavity 2 ruined the mode confinement. It seems that low δr bulges are more easily perturbed by alternate current paths,

Cavity	r_0	δr	l
1 and 3	10	2	30
2	20	1	100

Table 2.1: Bulge geometry. $r = r_0 + \frac{1}{2}\delta r(1 - \cos(2z/l))$, where $z = l/2$ is the center of the cavity. All units are in millimeters.



Figure 2.3: An electrode painted with colloidal graphite. Using a paint brush instead of aerosolizing the graphite can produce splotchiness, but these features are only a few microns deep, so they seem to be harmless.

¹The cavity walls must be resistive. Ideally, energy radiated by the plasma has no way of leaving the system except to be dissipated by the motion of charges in the cavity walls.

²Such short electrodes require proportionately higher precision. To keep the tilt angle below 1 mrad over a $\frac{1}{3}$ " electrode requires three ‘tenths’ precision, which is what the Berkeley shop achieved.

³The “walls” of the magnetic bottle confining the antihydrogen are produced by an octopole wound on a stainless pipe with wall thickness around 1 mm, inside which the electrode stack fits snugly. Radially speaking, the electrodes and pipe are dead space between the magnets and the antihydrogen. Sufficiently energetic antihydrogen can climb partway up the walls of the magnetic bottle and annihilate on the electrodes. The electrodes are made as thin as possible—currently about 1.5 mm.

⁴EMS 12660. In the absence of such a coating, the electrode surface may become locally oxidized and trap stray charges. These produce patch potentials which can drive plasma expansion [17].

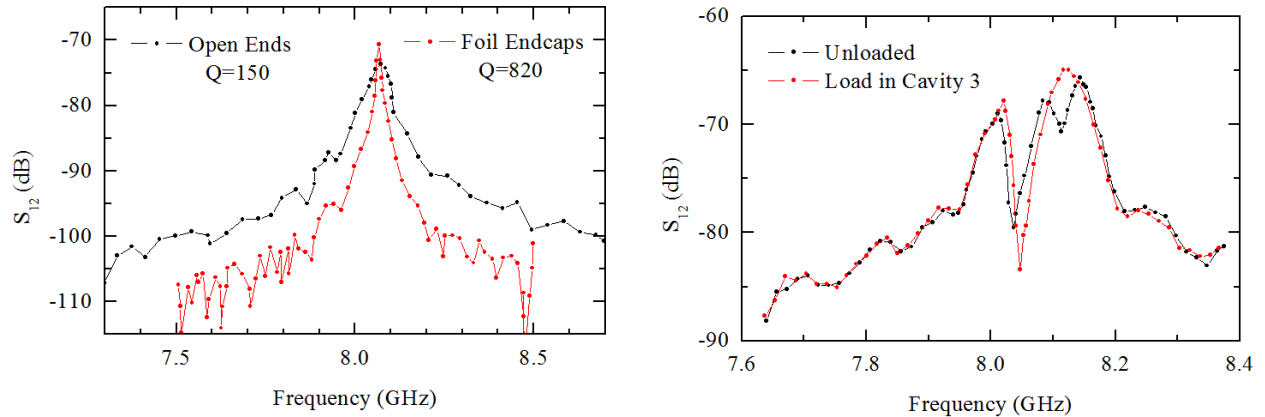


Figure 2.4: Signs of axial leakage from TE_{111} in Cavity 1. Left: Q is greatly improved by closing the ends of the stack in z with copper foil. Right: With all electrodes assembled, coupled modes manifest as multiple peaks in the transmission spectrum S_{12} (three peaks instead of one). To confirm that Cavity 3 was really coupling to Cavity 1, Nathan put his finger into Cavity 3, resulting in the second and third peaks detected in Cavity 1 pulling together into one broad peak. This suggests that the first peak comes from microwave power localized somewhere else in the stack.

for they found it possible to perform a transmission measurement in the final portless cavity using flat leads which snake in along the cavity wall. Such leads may distort the mode, but they probably do not alter the topology of the induced currents.

Cavity 1 was bench tested in the partly assembled electrode stack at Berkeley,⁵ using two radial ports to perform a transmission measurement S_{12} . This was an opportunity to investigate power loss paths from the TE_{111} and TE_{131} cavity modes. Most of these tests only included Module 1, containing the bottommost six inches of electrodes, with free space on both ends of the pipe. Neither mode leaks radially: wrapping the cavity in copper foil secured with hose clamps didn't change Q . The radial chokes designed by Evetts [31] are doing their job. On the other hand, the Q of TE_{111} was greatly improved by adding copper foil endcaps to the ends of Module 1, implying significant leakage down the pipe for this mode; Q of TE_{131} was only increased about 40%. After adding the remaining two Modules, the axial leakage from TE_{111} in Cavity 1 was sufficient to couple it to TE_{111} in Cavity 3. See Fig. 2.4.

The bulge structure is more effective at trapping higher frequency modes. The lower frequency modes have lower Q and have a spatial intensity pattern which tends to spill out of the bulged area. This has been confirmed on the bench and in simulation. Bulged cavities should therefore be well complemented by a pair of irises, which block low frequency radiation. This can increase the Q of lower order modes, just as blank copper endcaps were

⁵The Siddiqi Group graciously provided over an hour of time on their 40 GHz network analyzer in Campbell Hall.

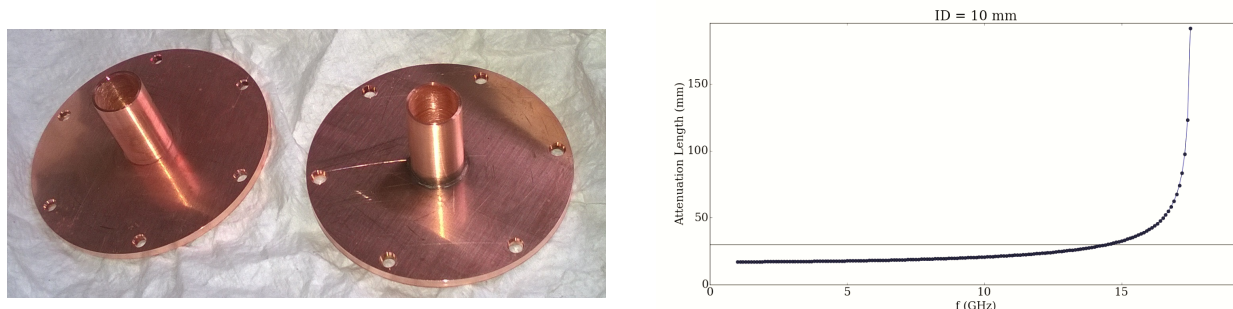


Figure 2.5: Irises and the curve which justifies them. The irises were machined by the author in the student shop at 0.001" precision. The apertured endcaps were soldered to 1 cm ID, 1" long OFHC copper tubes, which theoretically attenuates the 8.1 GHz radiation from TE_{111} by about 80%. It would not have been wise to make the aperture smaller (radially) or longer (axially) due to the risk of interfering with plasma insertion or extraction. The horizontal line in the figure on the right is at one inch, indicating that radiation of frequency $\omega < 2\pi \cdot 14$ GHz is attenuated by at least one factor of e . The copper was cleaned with lemon juice and salt, then acetone. The surfaces facing the egun and MCP were polished with Simichrome, and the surfaces seen by transiting plasma were painted with colloidal graphite.

shown to do. This idea fortunately arose when there was still enough time to include such parts in the assembly. See Fig. 2.5 for details. There is another reason to incorporate irises into a system containing bulge cavities. Whereas normal modes are trapped by the bulge geometry, for other modes the cavity is still essentially an open pipe. The cavities do not prevent unwanted microwave radiation from entering the trap. The irises do block radiation of sufficiently low frequency, about 10 GHz and below.

2.2 Electronics

The plasma is very sensitive to stray electric and magnetic fields. The heavy copper can surrounding the Penning trap is a good Faraday cage for frequencies above 10 Hz or so⁶, but this armor is pierced by many wires to the outside world, in particular the electrode HV lines and the Lakeshore temperature sensors. Noise can ride right in on those lines.

This section is mostly about reducing noise in the experiment. It also covers some new functionality introduced for doing microwave sweeps and testing electrode connections.

⁶Or much less for solenoidal fields. The B field from the gradient coil takes about 4 s to finish seeping into the trap.

Noise

The effect of electrode noise on minimum plasma temperature is presented in Chapters 5 and 7, Figs. 5.20 and 7.2. Significant plasma heating occurs for noise levels below 1 mV_{pp} . It is therefore necessary to address the challenge of delivering 150 V biases to the electrodes with something like 0.0001 V_{rms} noise.

At the Winter School for Trapped Charged Particles in Chamonix, Stefan Ulmer mentioned that his former group had once managed to cool an electron to 80 mK [72]. Ulmer was asked how this could possibly be achieved in the presence of electrode noise. The answer is that they can't do anything fun with the electron. Their trap uses effectively DC signals, so their amplifiers can incorporate four-pole lowpass filters with time constants on the order of a second. In contrast, the amplifiers used at CERN, and previously at Berkeley, have time constants of a few μs .

In 2016 Joel began to produce some nice slow HV amps for biasing Faraday cups at CERN. He graciously accepted a request that he, his son, and some of the undergrads produce 15 more of these units for biasing the electrodes at Berkeley. The slow amps are great. They can easily be calibrated to better than 1 part in 10^3 , have negligible drift if used responsibly, and satisfy the 0.0001 V_{rms} criterion with a rise time of about 25 ms . This is fast enough to do loading, Tdiag, SDREVC, reservoir sequences, in short everything except the fast dump (for FC or imaging), for which a reed relay is used.

Nice amplifiers are necessary but not sufficient for a low noise system. Cable length was reduced and operator responsibility was improved by consolidating all lab equipment on one side of the room. Lakeshore and egun cables which were not shielded were replaced. A Faraday cage was formed at the junction shown in Fig. 2.6. The latter came after many failed attempts to remove pickup from the lines. At length it was observed that the shields of the electrode cables were only connected on one side. Shields don't work at high frequency unless they are connected on both sides.

Nice amplifiers and good shielding are necessary but still not sufficient for a low noise system. For one thing, the PCB's in the filterboxes like to develop bad grounds or leaky capacitors. This problem can be difficult to diagnose. A bigger issue is the Lakeshore temperature sensors, which offer noise a bypass into the electrode stack (notice the CX's attached directly to Electrode 1 and Cavity 2 in Fig. 2.1). Just about everything with a

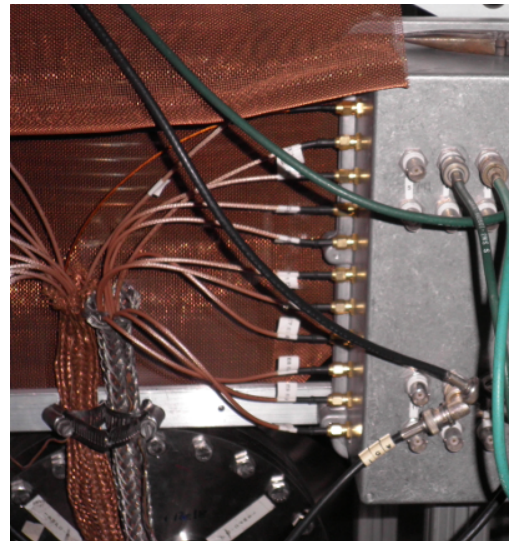


Figure 2.6: Faraday cage for electrode HV cable breakout. Copper and steel braids are hose-clamped at the aluminum crossbar and the feedthru flange below. The copper screen can be left up. The important thing is that the ground for the shields is the same at both sides.

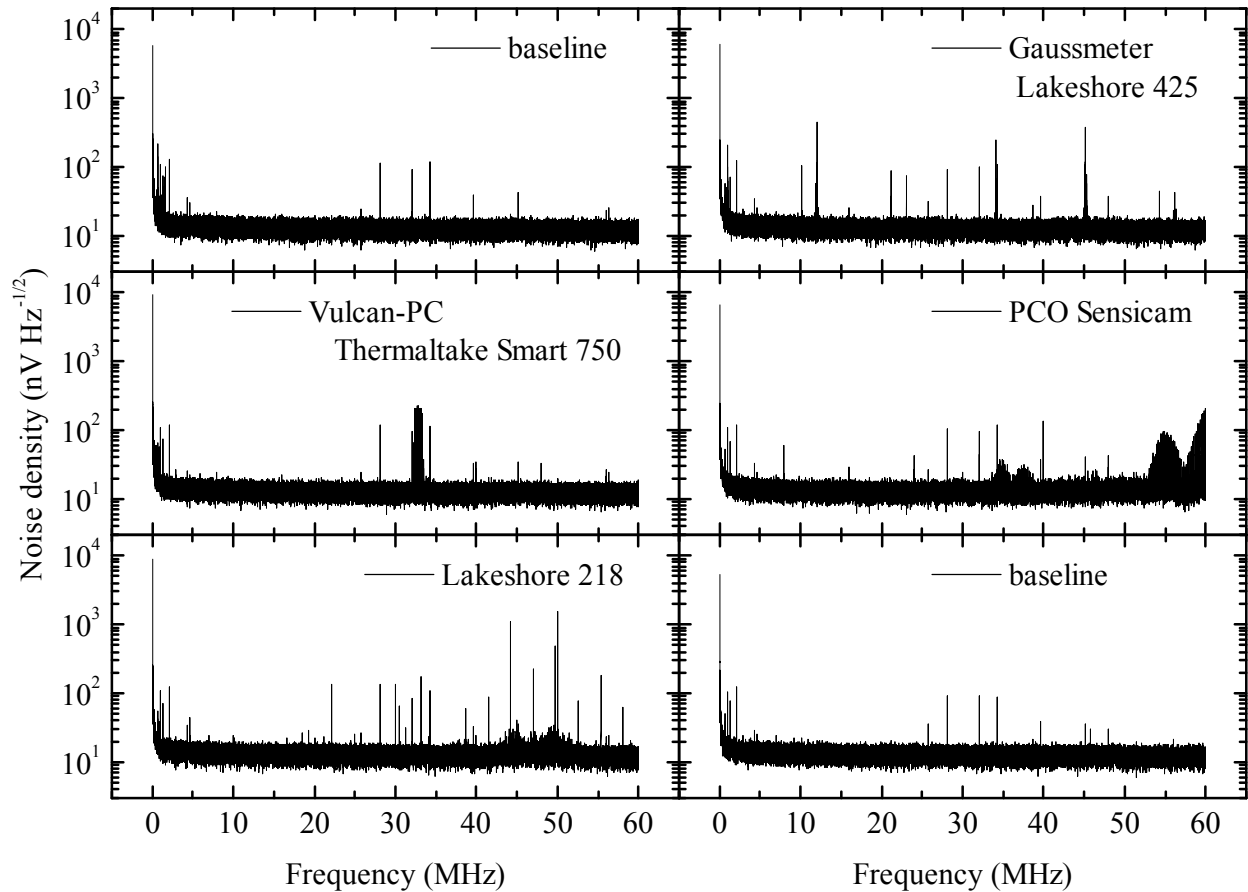


Figure 2.7: FFT’s of the quiescent voltage on a typical electrode. According to the hypothesis that the noise is entering the experiment on the Lakeshore CERNOX lines, the voltage inside is probably greater than what one can measure externally. Traces were acquired sequentially going down the left column then down the right. The “Lakeshore 218” is the CERNOX controller, and the Thermaltake is a PC power supply. A typical noise peak here has a linewidth around 1 kHz and an amplitude 100 – 1000 $\text{nV Hz}^{-1/2}$. For reference, the 1 mV broadband noise applied in Fig. 5.20 is equivalent to about 200 $\text{nV Hz}^{-1/2}$, which amounts to the same power obtained by integrating over the typical heating peak width in Fig. 7.1 (30 – 50 kHz). In other words, many of these peaks are large enough to produce significant plasma heating if they come into resonance with the dipole mode. As is discussed in Chapter 7, that is just what happens during many routine operations such as Tdiag.

switching power supply has something to say to the plasma through this channel, most of all the Lakeshore controllers themselves (see Fig. 2.7). There’s really one solution here: depower and disconnect the Lakeshores from the experiment in order to reach the lowest plasma temperatures.

The high voltage for the MCP and phosphor screen needs to be clean too. While these

elements are probably far enough away from the stack that they don't contribute to plasma heating, noise on these HV lines limits the sensitivity when counting charge in Faraday cup mode. One also finds that quieter supply leads to fewer horrifying events when operating an HV device close to a spark-threshold.

The SRS ps350's have been pitched, in favor of a pair of linear, low-noise Bertan 230's. These power supplies go to 30 kV and are ramped either manually (phosphor) or using an analog signal (MCP back), so careless operation could easily ruin the detector.

Egun Feedback

Sometimes not much is changing about the experiment from cycle to cycle, as for instance during a long magnet ramp or microwave cue. It is then possible to automatically adjust the egun heater current, based on the number of electrons counted at the end of the previous cycle, to get a consistent number of electrons each cycle without input from the user. Purely proportional feedback is sufficiently fast and robust in most circumstances where automated feedback can be relied upon at all.

When the temperature varies significantly from cycle to cycle, as for a cooling curve, the number of electrons read on the slow charge accumulator (see next Chapter) will vary, being artificially low for hot plasmas. In this case it is often possible to "coast" for a while at the last feedback setting. At the beginning of a typical day, the egun current must be decremented by $4 \cdot 10^{-4}$ A per cycle, $2 \cdot 10^{-4}$ A for most of the day, and close to 0 after a very long day. The time evolution of the egun-can temperature indicates that this is not a pure heating effect; the temperature takes days to reach equilibrium. The decrease in heater current required for a given emission, over the course of a typical day, is more likely due to burning off impurities and perhaps reactivating the cathode.

Microwaves

The Penning-Malmberg trap at Berkeley differs from the ones at CERN by being nearly air-tight. The egun side is closed, and the MCP assembly is snug in the entry tube at the other end (Fig. 2.8). At CERN, microwaves are delivered through a horn aligned with the trap axis (the horn can be translated into the position otherwise occupied by stick or MCP). At Berkeley, the MCP is always in the way. The horn (Fig. 2.9) is also a little off-axis because it is mounted on top of the camera (Fig. 2.10). Perhaps surprisingly, it is not difficult to get enough power in to heat the plasma. Because the MCP is mostly glass and empty space, it is nearly transparent to microwaves [95]. The horn at Berkeley is also designed for peak transmission around 12 GHz, making it much bigger than the one at CERN. This may make alignment less critical.

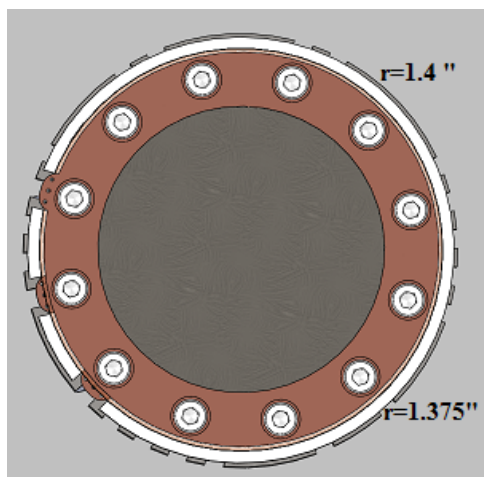


Figure 2.8: Solidworks drawing of the MCP, with outer radius and slot radius marked. The experiment has to be pumped through these tiny gaps. The author does not endorse this choice.



Figure 2.9: Microwave horn sitting on the hp8673d synthesizer used for most of the microwave work in this thesis. Horn was designed and built by the undergraduate Ryan Mcpeters.

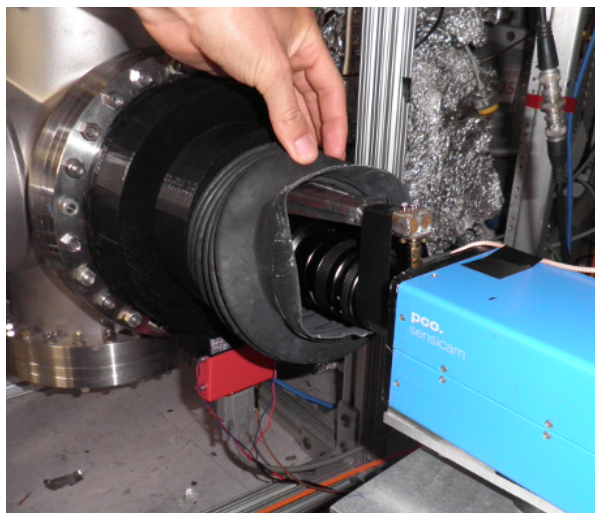
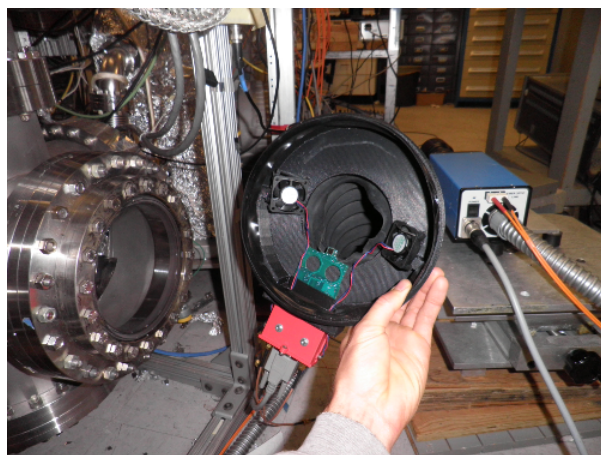


Figure 2.10: Dark box at the end of the experiment. The plasma hits the MCP/phosphor assembly 10.6" upstream from the vacuum window. Photo on the left shows the inside with fans and SiPM (6 mm black square at the top of the PCB). Photo on the right shows how horn, camera, and SiPM can be mounted simultaneously in a light-tight arrangement that still allows easy access for camera focusing.

2.3 Magnets

This section details the design and performance of a cryogenic dipole coil, which was of pivotal importance in the cavity studies and some usefulness in the microwave work as well. The end of the section includes a calibration of the inductive response of the superconducting solenoid to the new coil.

Thermal load

Estimates are given here for the amount that the gradient coil heats up the experiment. The residual resistivity ratio (RRR) and magnetoresistance affect these numbers and will be discussed immediately after.

Static Hookup Rate: This is the thermal leak with no current running. Assuming the two wires are well sunk to the 1st stage of the coldhead, and that this is 50 K,

$$H_{\text{hkp}} = 2\Theta A/L = 37 \text{ mW}. \quad (2.1)$$

Joule Heating in the Hookup Wires: This is the heating from driving current through the two 1 m long leads. Assume $I = 1$ A and $RRR \sim 1/5$ nominal at $T = 50$ K,

$$H_{R100} = 2I^2 R_L / (RRR/5) = 2 \text{ mW}. \quad (2.2)$$

Joule Heating of the Coil: This is heat generated by current in the copper electromagnet. Assuming $I = 1$ amp and $RRR \approx 1/4$ nominal due to magnetoresistance in the 1 T field (see below),

$$H_{\text{dip}} = I^2 R / (RRR/4) = 400 \text{ mW}. \quad (2.3)$$

Wire gauge	G	22 AWG
Current rating (data sheet)	I_{max}	5.5 A
Wire diameter	D	$6 \cdot 10^{-4}$ m
Area	A	$2.9 \cdot 10^{-7}$ m ²
Length	L	1 m (hookup), 300 m (coil)
Lengthwise resistance	R_L	$0.064 \Omega \text{ m}^{-1}$
Measured magnet resistance	R	20 Ω
Residual resistivity ratio	RRR	200
Thermal integral, 50-10 K, OFHC	Θ	$5 \cdot 10^4 \text{ W m}^{-1}$

Table 2.2: Properties of the wire used for the gradient coil, now in SI units.

In order to reduce the expected Joule heating in the magnet, a study was made of the properties of various wire samples and preparations in order to obtain the lowest cryogenic resistance, i.e. high RRR. 4-wire capsules were set up for dunking in a liquid helium dewar. These were then baked. The wire resistance was measured in air, liquid nitrogen, and liquid helium. The wires tested were all 24 AWG, having 19 strands (m16878/5 bee), 7 strands (m16878/4 beb), and 1 strand (Accuglass 112615). The mil-spec wire came with Teflon insulation, versus Kapton for the Accuglass wire. The wire from Accuglass had higher RRR (see Fig. 2.11). Accuglass wire was also superior in an earlier test using 30 AWG wire. Because of its stiff Kapton insulation, the Accuglass wire may suffer less cold-working during hookup and insertion into the dewar. Kapton has another advantage: it may be safely baked to 250 °C (perhaps much more [27]). The Accuglass wire was used for the copper dipole. It was baked harder than the samples used in the earlier test: 250 °C for over three hours. Also, because of the rigid form, strain-relieved leads, and increased care accompanying final installations, the dipole coil wires were scarcely touched after baking, whereas the test samples are inevitably cold worked on their way into the dewar. Finally, the dipole wire is much longer than the wires used in the tests, which reduces errors due to hookup and partial thermalization of leads. These factors may account for the significantly greater RRR measured for the copper dipole *in situ* and cryogenic, which exceeded 600 (Fig. 2.12).

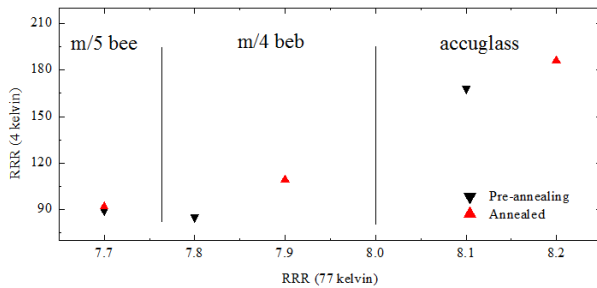


Figure 2.11: Summary of RRR tests. The test samples were annealed at 200 °C for two hours, but were not on a rigid form, so probably underwent some cold working on their way down the neck of the helium dewar. Resistance was determined by 4-wire measurement with a Tenma sourcing 15, 30, 60 mA and a Keithley-2001 measuring the voltage; compared to the Keithley’s built-in 4-wire functionality this method (3 data points at different I) results in less statistical fluctuation and eliminates the worst sources of systematic error.

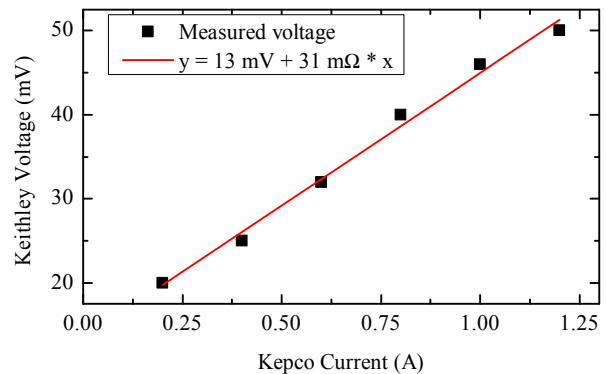


Figure 2.12: Measurement of the cryogenic resistance of the gradient coil. The resistance at 9 K is about 31 mΩ. The room temperature resistance was measured with a 2-wire DMM on bench and *in situ*; the resistance was $20 \pm 1 \Omega$ in both cases. For the data in the figure, a 4-wire measurement was required because of the greatly reduced resistance at 9 K.

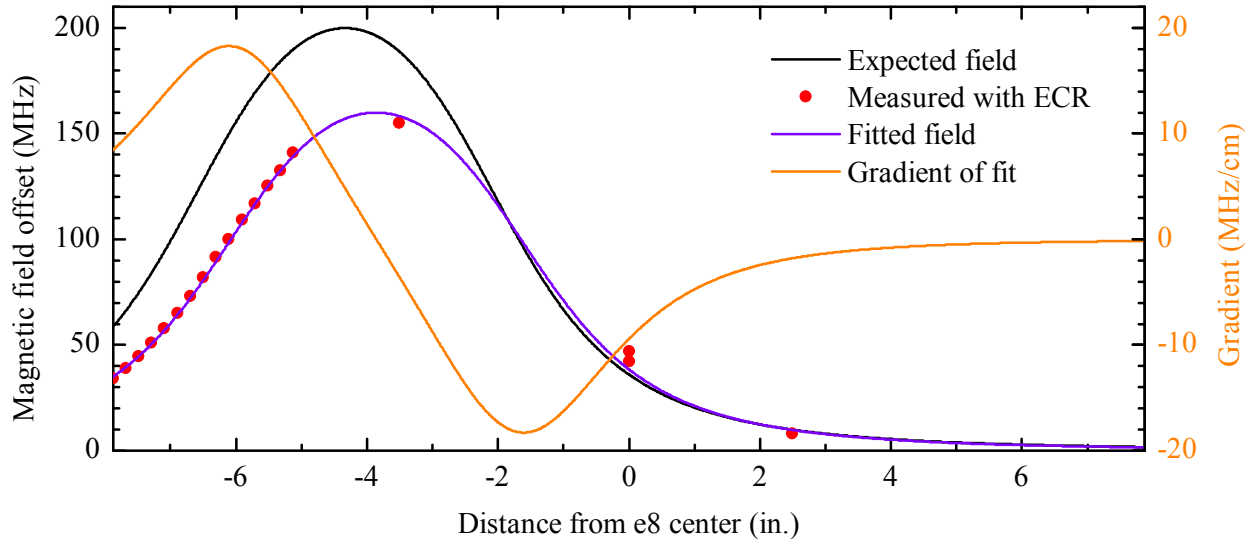


Figure 2.13: Calculated field due to the gradient coil, verified using ECR. The field and gradient produced by passing 1 A through the copper electromagnet are shown. The titanium nine-segment cavity is centered at about -6.5 in.

Cryogenic copper can develop a significant magnetoresistance in the strong fields of a Penning-Malmberg trap. This lowers the effective RRR . At $B = 1$ T and $T \approx 10$ K, the effective RRR is lower by a factor of four [49]. The effect is less severe at higher temperature.

Coil field and field gradient

The on-axis magnetic field for a solenoid of length l and radius r is in Jackson [54].

$$B(z) = \frac{\mu_0 I}{2l} \left(\frac{z}{(z^2 + r^2)^{1/2}} + \frac{l - z}{((l - z)^2 + r^2)^{1/2}} \right) \quad (2.4)$$

Putting this into Mathematica, one finds that a $5 \cdot 2.54$ cm long coil with $4.6 \cdot 2.54$ cm diameter and 900 turns running at 1 amp can achieve $\Delta B/B \sim 10^3$ and create an extra field up to about 6 mT. The field and gradient are plotted in Fig. 2.13.

When measured using ECR, the peak field at 1 A was found to be slightly lower than expected. This is probably a result of fewer-than-expected turns of wire. Fortunately, the cryogenic resistance of the wire was also much lower than suggested by single-wire tests (next section). This made it possible to run continuously at 2 A while only increasing the electrode temperature by a fraction of a degree.

Mutual inductance

Since the coil is going inside a 26 H superconducting solenoid, changing the current in the coil will induce a change in the solenoidal current, which changes the background magnetic

field according to $B_s = I_s/40.1 \frac{\text{A}}{\text{T}}$. Any infinitesimal emf induced in the superconductor will immediately lead to a negating supercurrent:

$$0 = \mathcal{E} = L_s \dot{I}_s + M_{sc} \dot{I}_c \rightarrow \Delta I_s = -\Delta I_c \cdot \frac{M_{sc}}{L_s} \quad (2.5)$$

To evaluate this expression, use the rule for loop inductance $L = \Phi/I$. For the mutual inductance, it is convenient to use Φ_{cs} , the flux in the coil due to the homogeneous solenoidal field:

$$M_{sc} = M_{cs} = \frac{N_c \Phi_{cs}}{I_s}, \quad (2.6)$$

where $N_c \approx 900$ is the number of turns in the gradient coil. The flux is just the background magnetic field B_s times the area of the coil $A_c \approx 0.011 \text{ m}^2$ for a coil of radius $r \approx 6 \text{ cm}$. Combining equations,

$$\begin{aligned} 40.1 \frac{\text{A}}{\text{T}} \cdot \Delta B_s &= \Delta I_s = -\Delta I_c \cdot \frac{A_c/40.1 \frac{\text{A}}{\text{T}}}{26 \text{ H}} \\ \rightarrow \Delta B_s &= -\Delta I_c \cdot 2.3 \cdot 10^{-4} \text{ T}, \end{aligned} \quad (2.7)$$

one finds that the background field should change by about 0.5 mT when running the coil at its maximum field of about 10 mT at 2 A. This agrees with the observations in Fig. 2.14. For these measurements and in general, total magnetic field is measured by an external Lakeshore Gaussmeter, calibrated using the known current through the solenoid and the conversion factor given above.

2.4 Vacuum

Electron plasmas require a very good vacuum. Pressure higher than 10^{-9} mbar usually causes significant expansion due to collisions between plasma electrons and residual gas. This process looks like a random walk to the wall for electrons, with step size $r_L \sim 2 \mu\text{m}$ and step rate $\nu_g \approx n_g \sigma v_t \sim 1 \text{ s}^{-1}$ at 10^{-9} mbar, where n_g is the neutral gas density and $\sigma \approx 3 \cdot 10^{-20} \text{ m}^2$ [59]. Collisions with neutrals can produce ions, which can drive instabilities, leading to more expansion and more concomitant heating. Collisions also interfere with other mixing processes relevant for the cavity resonant cooling studies.

A good vacuum system provides a respectable base pressure in a reasonable pumpdown time. The outside of the 98 lb ultra-high-vacuum (UHV) system is shown being leak checked in Fig. 2.15. For reference, Fig. 2.16 displays the Solidworks model of the UHV, along with

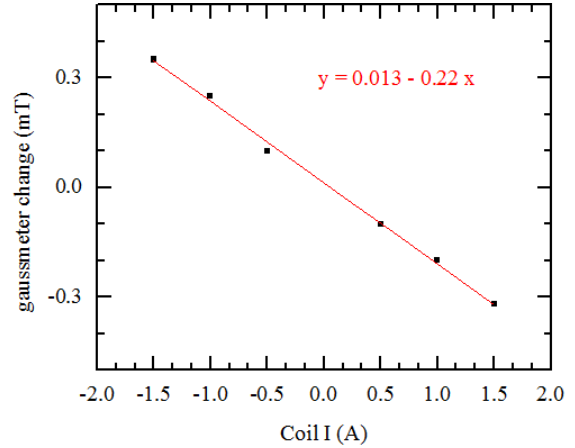


Figure 2.14: Superconducting solenoid reacting to the gradient coil. The slope, -0.22 mT A^{-1} , is within 5% of the first principles estimate Eq. 2.7.

mechanical and thermal service. Some of the functionality referred to elsewhere in this chapter is summarized in the caption to Fig. 2.16.

Although the material in this section is not novel, the author's experience indicates that it is too often ignored in the construction of modern experiments to be ignored in this thesis.

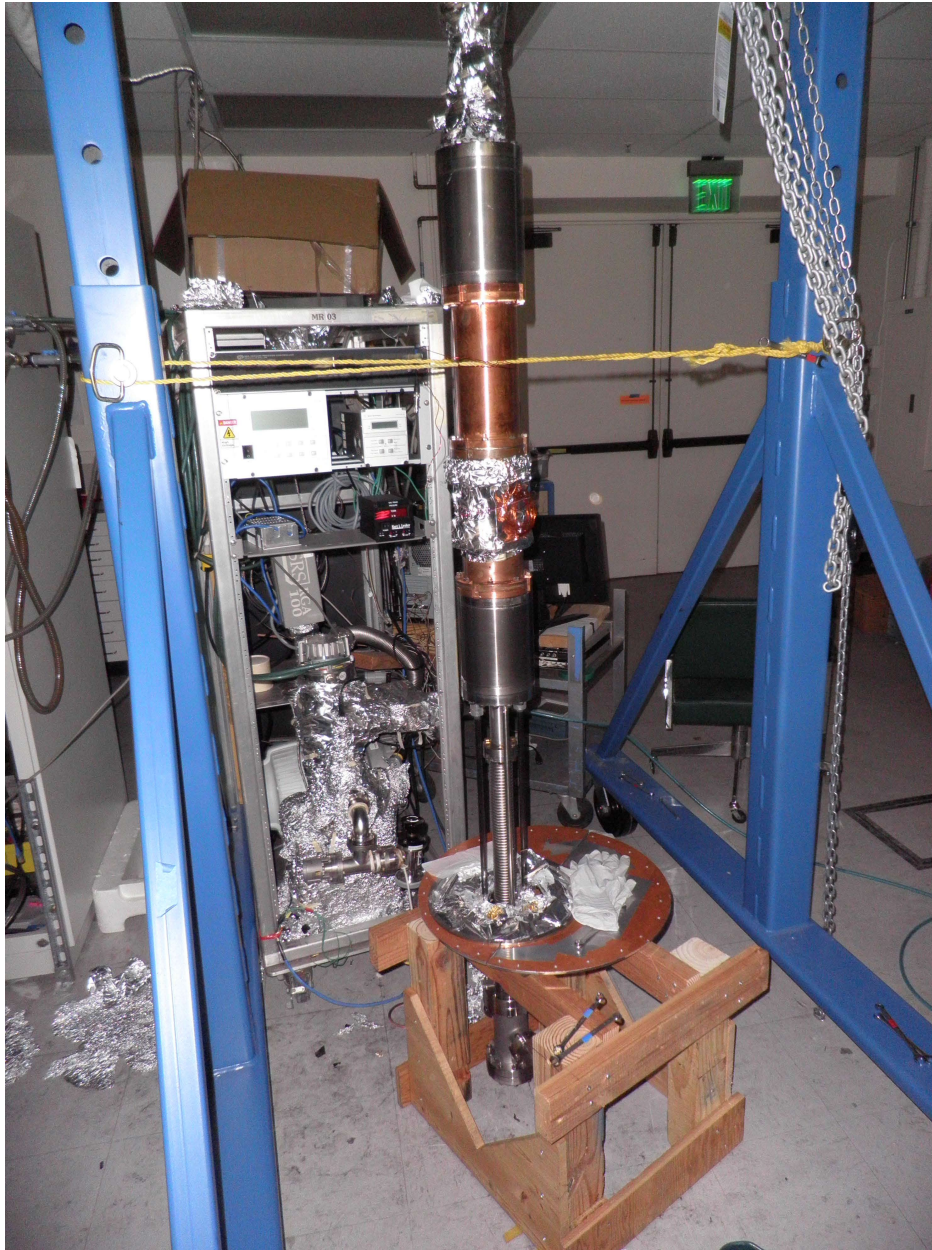


Figure 2.15: UHV assembly being prepared for insertion in the magnet bore. First it must be pumped, leak checked with alcohol, baked, and leak checked with helium. The vertical arrangement allows these processes to occur with symmetric pressure applied to the helicoflex seals. The electrode stack is inside the two copper cans in the middle, one of which is partly covered by foil which protects the gradient coil. The egun is the foil bundle at the very top of the figure, and the MCP, not yet inserted, will go in the final cross just above floor-level.

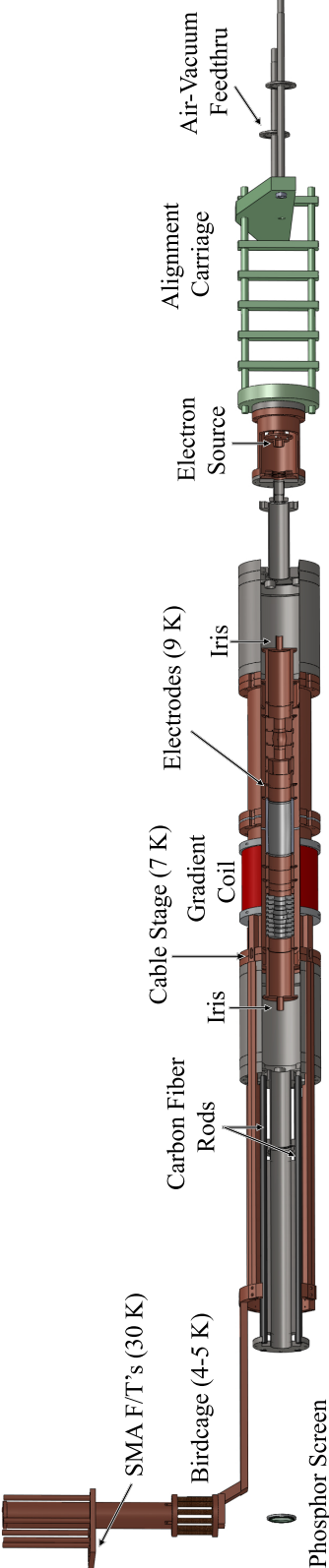


Figure 2.16: Solidworks model of the ultra-high vacuum system (UHV). A $3 \cdot 2.54$ cm cut is taken out of the central region to show electrodes and surfaces seen by the plasma. Some of the UHV (on the left, enclosing the phosphor screen) is omitted for clarity. The coldhead (not shown) is above the copper manifold at the extreme left. The electrodes are cooled by the high voltage cables which bias them. These cables are sunk to the coldhead's 1st stage at "SMA F/T's" and to the 2nd stage at "Cable Stage," inside the UHV. The cryogenic UHV is supported by insulating materials: on the left by carbon fiber rods (where the central bellows holds vacuum), on the right by a G-10 structure. The carbon fiber rods attach on the left to the 77 K nitrogen shield. The G-10 "Alignment Carriage" passes to air through two $0.5 \cdot 2.54$ cm steel rods welded to KF-40 blanks which seal the isolation vacuum. These blanks connect to flexible bellows, permitting 10 mm adjustment in any direction (20 mm travel).

Pumps and Leaks

Here is a short list of (perhaps subconscious) misconceptions occasionally encountered:

1. Better vacuum is achieved by buying a bigger pump
2. A low pump speed just means pumpdown will take longer
3. Ion pumps bake themselves
4. Blind holes become irrelevant in a cryogenic system

The basic equation governing the pressure p in a vacuum system is

$$dp/dt = Q/V - pS/V, \quad (2.8)$$

$$\implies p(t) = Q/S + (p_0 - Q/S) e^{-\frac{S}{V}t} \quad (2.9)$$

where Q is the leak rate in mbar l s⁻¹, V is the chamber volume in l, p_0 is the pressure at any reference time $t = 0$, and S is the pumping speed in l s⁻¹. Here S is not merely the pump speed S_p . Instead, $S^{-1} = S_p^{-1} + S_m^{-1}$, with S_p the speed of the pump and S_m the speed of the manifold connecting the pump to the chamber. Conductances add reciprocally, just like in electronics. In fact the general vacuum problem has a simple circuit analog, which is shown in Fig. 2.17.

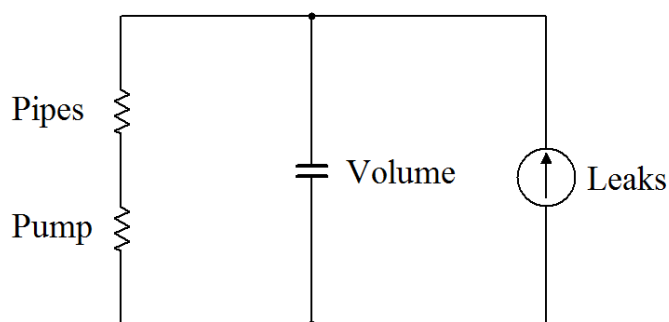


Figure 2.17: Circuit analogy for a vacuum system, mathematically equivalent to Eq. 2.8. In this analogy the reciprocal of conductance S^{-1} is taken as a resistance, the leak rate Q becomes a current source, the volume V becomes a capacitance, and the pressure p is the resulting voltage at node (2). Getting a good vacuum is equivalent to getting the charge off that capacitor.

Aperture	$9 \cdot D^2$
Short Tube	$\frac{12 \cdot D^3/L}{1+4D/3L}$
Long Tube	$12 \cdot D^3/L$

Table 2.3: Molecular flow, room temperature conductances S in l s⁻¹. D and L are the inner diameter and length in cm. From Ref. [91].

According to Eq. 2.8, p will never be lower than Q/S . If $S/V < 1$, no amount of waiting will result in good vacuum. If the pump system includes KF-40 components, S is most

likely limited by the conductance of these components (S_m), not by the speed of the pump attached to them. Approximate formulae for conductance are given in Table 2.3.

Regarding the ion pumps misconception, old ion pumps can be revitalized if they are big enough that one can get in there with a screwdriver and take them apart. They will be full of black flakes which accumulate over time via microsparks on the electrode structure. All this can be put in a sonic bath and, if necessary, worked over with the Dremel. The plates which erode under ion bombardment can be flipped around; the other side is made of the same stuff. In general, it's true that an ion pump gets hot when it's first turned on, but proper attention, including use of the often built-in external heater circuit, results in lower ultimate pressure.

Blind holes are a class of the bigger problem of virtual leaks. Virtual leaks due to offgassing from a dirty surface do get better at low temperature. Indeed at sufficiently low temperature dirt may have a helpful, gettering effect. This is not true for virtual leaks due to blind holes, that is, holes which accept a screw but don't go all the way through the material, so that a dead air space is created. This is especially problematic in a low conductance system like ours, where the vacuum is not good prior to cooldown. In this situation virtual leaks make it impossible to begin the cooldown at a low pressure. Cryogenic gettering surfaces are simply saturated rather than supplying ongoing support. Elimination of blind holes is one reason nearly every part in the UHV was brought to the shop at some point in 2016.

More advice

Kim Wipes may be cheap but for UHV work Texwipes are superior because they don't produce dust. Folks at CERN prefer an orange sponge-like material because it is easy to remove if it partially disintegrates on the part being cleaned.

Denatured alcohol should not be used in the UHV. Pure ethanol and acetone are the best. Several large bottles of denatured alcohol were brought into the lab under the previous administration. This error is the source of a certain nasty and persistent residue on the copper of Cavity 3 (cf. Fig. 2.1).

When Conflat hardware cannot be used, indium may be the best choice for cryogenic UHV seals.⁷ A popular alternative used at CERN and at Berkeley is the Helicoflex seal from Technetics. These seals are as expensive as their lead time is long. They are also prone to failure if there is the slightest thing wrong with the sealing surface. The UHV leaks when it goes cryogenic because of these seals. Fortunately it is already in a pretty good cryogenic isolation vacuum. Another frustration regarding these seals is that the bolt pattern on the copper nipples was understuffed by about a factor of two, requiring an unreasonable load on the 8 bolts for which holes exist. The nipples would need to be remade from scratch to overcome this design problem. These are not little nipples: the job would be worth a few thousand dollars plus shop time. It seemed better to go on murdering bolts, hoping they don't strip too early to get some kind of a seal.

⁷This statement is based on indium sales literature, along with the purportedly widespread use of indium

2.5 Cryogenics

The plasma cannot be colder than the electrodes⁸. The best thing for cooling a large experiment is liquid helium, which guarantees $T \approx 4$ K for all adjacent surfaces— provided the heating rate is low enough that one can accumulate liquid at all. This is what is used by the ALPHA experiments at CERN. At Berkeley the experiment is cooled by a closed cycle refrigerator (CCR) with helium gas as the working fluid. This is cheaper, simpler to maintain, and more sustainable, but has a severe operational disadvantage. For a liquid helium system, a heat load of several watts will burn lots of helium (1.4 L/hr per watt) but should not increase the electrode temperature more than a degree or so, and may be acceptable. Whereas in a system such as ours, cooled via a copper manifold connected to the 4 K stage of a CCR, such a load significantly increases the equilibrium temperature of the experiment. By addressing heat leaks and improving the copper manifold in 2016, the equilibrium electrode temperature was reduced from about 14 K to 9.0 K. These few degrees make a big difference:

1. The dominant component of the residual gas is typically molecular hydrogen, which freezes onto the walls at about 10 K. This gas can drive plasma expansion and decohere the center-of-mass cyclotron mode at the heart of the cavity and microwave work.
2. Colder positron and antiproton plasmas combine to form more trappable antihydrogen (Chapter 1). In ALPHA-2, when the plasma is 15 K, two times more trappable antihydrogen is produced during mixing, compared to when it is 25 K. A 9 K plasma should be better still. It is important to show that it is possible to produce and accurately diagnose such a plasma at $B = 1$ T and below. In particular, given that the parallel energy analyzer is only accurate to $\delta T/T \approx 10\%$, effects which do not raise the plasma temperature by more than a few degrees can only be studied using a plasma with $T \sim 10$ K or less.

Heat flow in the experiment

The equilibrium electrode temperature is determined by the temperature of the sources of heat (300 K and 77 K) and cold (4 K), and the coupling of the electrodes to these sources. It is mathematically the same problem as was addressed in Section 2.4. If one only cares about the final temperature, one can neglect capacitive effects and treat the system as a voltage

in the chemistry department for making cryogenic seals and the glib confidence of an indium seller. Grooves have been added to the UHV to accommodate indium, but to date cooldown has only been attempted using the Helicoflex seals, since it is known that they basically work, and the cost of failure is so high.

⁸One can temporarily achieve lower plasma temperatures using active techniques such as adiabatic expansion, which increases the plasma length, or evaporative cooling, which increases the plasma radius and throws away particles. In both cases the plasma will heat right back up as the plasma is no longer in equilibrium with its thermal bath. Nor is the new geometry likely to be stable. Even where these compromises are acceptable, it is best to start with the coldest possible plasma.

divider. In this analogy, a thermal bath acts as a battery, and the conductance equivalent of a heat-carrying element equals $\frac{\text{Area}}{\text{Length}}$ of that element, times its thermal integral [57] evaluated for the temperature difference across it. In Table 2.4 the conductances and consequent heat loads (currents) are estimated this way. The total input power comes to about 500 mW. This power must flow from the experiment to the 4 K coldhead through a copper manifold or “coldbar.”

The combined area/length of the cooling manifold, summed in parallel, $|A/l|_{tot} \approx 0.06$ cm. Thus, 500 mW will flow through the coldbar when the thermal integral (for OFHC copper) is about 10 W cm^{-1} . This occurs for a temperature $T = 7\text{--}8$ K at the UHV (and 4 K at the coldhead). That prediction is close to the measured electrode temperature $T = 9.0$ K. The 1–2 K discrepancy might be accounted for by the 1 K drop measured across part of the coldbar known as the “birdcage,” a highly problematic joint which must flex under contraction at a 90° angle (see Fig. 2.16). Many enjoyable days elapsed while prototyping new birdcage assemblies with Warner Carlisle.⁹ The wire-bundle assembly shown in Fig. 2.18, which is currently used, drops at most 1.5 K according to sensors on copper elements immediately upstream and downstream of it.

The final temperature quoted above is largely the result of efforts in 2016 to reduce heat loads and increase the conductance of the coldbar. In addition to the work done on the birdcage, many of the coldbar elements were re-machined from fresh stock to be thicker, have more surface area at joints, and have fewer joints. Joints were made with brass screws which compress more when they get cold, or, where steel could not be replaced, titanium spacers were inserted (titanium shrinks less than steel). Coldbar pieces were annealed at 250°C for several hours to improve RRR, which it turns out is relevant for thermal transport too. Non-essential UHV lines were removed. Electrode lines were sunk to the first stage of the cryocooler via an apron of SMA feedthrus, then isolated from the UHV by breaking the shield and replacing with thin wires. Stainless steel support rods were replaced with carbon fiber and structurally reinforced G-10 (see Fig. 2.16). UHV electrode cables were clamped to the cold a centimeter away from each electrode, as these are the electrodes’ only thermal connection (clamping can be seen in Fig. 2.1).

Shrinkage

Things shrink when they get cold. From 300 K to 10 K, most metals shrink by a few parts in 10^3 . Thermal contraction seems to have been neglected in the original design of the experiment. This is the second reason that almost every part in the UHV was in the shop in 2016.

⁹There is room for further development here, perhaps more than anywhere else in the coldbar. It was never determined whether the wires were making more than a superficial connection after being melted into the cones dug into the top and bottom solid pieces. But 1.5 K is pretty good considering what came before was made of rigid rods and consequently would have dropped much more after bending reduced the contact area to effectively the screws making the joint...though this was not measured.



Figure 2.18: The most difficult joint in the experiment to design, build, or install. Though several other designs were considered, this one is close to the original, but able to flex when the coldbar contracts. OFHC wire from MWS was wrapped on a 2" form on the lathe, wrapped in tape, then sliced down the middle to obtain equal length segments. These segments were rolled straight on a desk using paperweights and undergraduate labor, then washed in acid followed by alcohol, dried, and stuffed individually into holes in the copper base (left photo). Several hundred segments are shown. After fitting the bundles through another copper piece on top, both sides are copper welded in the main shop and then milled flat in the student shop (right photo) to allow for a good thermal joint. Notice the arc of missing material at N-NE, which added to the suspicion that the weld was not as deep as desired. The joint on the bottom is done blind, with gloves and a tiny allen wrench, through the opening in the birdcage "bars" visible on the left, in the presence of sensitive electrode and Cernox lines. This needs to be done without upsetting the indium foil in the bottom joint until it is compressed.

Element	Material	Θ [W/cm]	$\frac{\text{Area}}{\text{Length}}$ [cm]	Heat Load [W]
Gradient coil leads	Copper	500	$2 \times 0.0037/100$	0.04
Electrode leads	Copper	500	$23 \times 0.00013/100$	0.02
Support Rods	Carbon fiber	$\mathcal{O}(1)$	$2 \times 1/30$	0.08
Support Rods	G-10	1	$2 \times 1/35$	0.07
Lrod Standoffs	G-10	0.1	$4 \times 0.25/0.50$	0.20
Electron Gun	Electricity	N/A	N/A	0.08

Table 2.4: List of warm elements, with their theoretical coupling and thermal burden at the copper UHV can where the coldbar is attached. Grad coil and electrode leads go to first stage of coldhead (30 K, carbon fiber rods and G-10 standoffs go to liquid nitrogen temperature (80 K), and G-10 rods go to room temperature (300 K). The heat load from the egun is an average of I^2R assuming about a thousand plasmas are produced per week.

A “shrink budget” (Table 2.5) was compiled to determine the initial and final lengths of (a) the electrode stack (b) the support skeleton in which each module of six electrodes must float and (c) the copper nipples clamping the skeleton, and inside which an electrode floats. These lengths need to match. Electrodes need a little compression inside their module to hold them in a line. Too much compression may short modules together or break something.¹⁰ The solution is a spring washer, which can maintain some compression both warm and cold. Most spring washers are unacceptably ferromagnetic, but a few, made of beryllium copper, were found and incorporated into the support structure (aluminum skeleton) around the Penning trap.

¹⁰like the ceramic spacers visible in Fig. 2.2. All ceramic parts were replaced with PEEK in 2016.

Object	#	l_1	$(\delta l)/l$ (.001"/1.00")	l_{tot} (1.00")	δl_{tot} (.001")
Cu electrodes	8	0.95	3.3	7.6	25.08
Split ring	2	0.45	3.3	0.9	2.97
Ti 9 electrodes	9	0.283	1.5	2.547	3.8205
Ti 1 electrode	1	3.95	1.5	3.95	5.925
Cu e1	1	0.95	3.3	0.95	3.135
Cu e18	1	0.05	3.3	0.05	0.165
PEEK spacers	21	0.05	10	1.05	10.5
PEEK endwashers	2	0.035	10	0.07	0.7
Al skeleton bot	1	0.22	4.1	0.22	0.902
Al skeleton top	1	0.65	4.1	0.65	2.665
Stack Total				17.987	56
Cu nipple	2	10	3.3	20	66
Cu mateplate	1	0.105	3.3	0.105	0.3465
Al Helicoflex	4	0	4.1	0	0
Cu flange bot	1	-0.7	3.3	-0.7	-2.31
Cu flange top	1	-1.425	3.3	-1.425	-4.7025
UHV Can Total				17.980	59
Al Threaded Rods	3	6	4.1	18	73.8

Table 2.5: Shrink budget for the UHV. The net 0.018" extra shrinkage of the aluminum threaded rods is compensated by beryllium copper spring washers.

Chapter 3

Diagnostics

The diagnostics described in this chapter are destructive. Electrons escape from the trap with about 30 eV of kinetic energy ($1/100^{\text{th}}$ the speed of light) in the direction of \mathbf{B} . They hit the MCP. The resulting charge or light signal is used to infer what the plasma was doing before it was released. One can reliably reconstruct the plasma shape and position (Section 3.1), the number of electrons N (Section 3.2), and the parallel energy distribution (Section 3.3). Traditionally these three diagnostics are done separately on three different plasmas. This requires a high degree of reproducibility, limiting the scope of possible experiments. With the aid of the silicon photomultiplier (SiPM) (Section 3.4) one can usually perform a charge measurement with the Faraday cup (FC) in tandem with a light-signal-based temperature measurement. This enables much more careful study of the N -dependence of, for example, cavity cooling and plasma heating from noise or expansion. Specifically,

- i It is difficult to reproducibly load small numbers of electrons ($N < 10^5$). All of the egun-based loading techniques ultimately depend on a plasma instability¹. N fluctuates from one plasma to the next. Knowing both N and T for the same plasma makes it possible to access N -unstable regimes without including the fluctuation as an uncertainty in N .
- ii The egun emission (A) drifts as it warms up and (B) jumps when patches of accumulated hydrogen burn or flake off its surface [75]. By keeping track of N one can use feedback to stabilize the load². This often permits running the experiment in autopilot for stretches of fifteen minutes or longer.

¹The pinched-off beam or “sabre” of electrons is two-stream unstable on the scale of a few hundred bounce times ($100 \cdot \omega_z^{-1} \sim 10 \mu\text{s}$). The majority of electrons in the sabre are trapped by this instability [42]. The question of how (and how many) such instability-trapped electrons can be retained by the time-dependent trapping potential applied to the electrodes is difficult to address outside of simulation.

²One could do this with the FC only by alternating between counting and Tdiag mode, although it’s rarely attempted. Checking N on every other cycle presents a constant distraction for the operator, is tricky to automate, and what’s worse, is susceptible to an on-off oscillation which introduces a new systematic error and often destabilizes the feedback loop. See Section 3.2 for more details.

For $N > 10^5$, it is possible to run all three diagnostics at once.³ The slow (temperature) dump causes shear instabilities which distort the plasma profile, especially for cold dense plasmas. But the image still contains information. The shape and colors captivate the imagination, providing the mind an anchor in the experiment. The image identifies the plasma. Changes to the shape may alert the operator that not everything is as consistent as the other diagnostics suggest. An experienced operator can estimate T and n from these images based on the feature scale (λ_D) and diocotron trail. Finally, no matter how messy the image, one can readily compute the center of mass to estimate the plasma position in the trap. This could become a part of ECR-based schemes for obtaining the radial dependence of the magnetic field (see Chapter 6).

3.1 Imaging

The source of light for the plasma image is the phosphor screen of type P47, which emits $\mathcal{O}(100)$ photons per incident 4 keV electron [23]. The screen sits $10 \cdot 2.54$ cm upstream of the outermost vacuum window. The light collecting optics are necessarily outside this window. The camera uses an adjustable lens (f/5.6 or so) to focus the image of the entire screen onto a charge coupled device (CCD) (see Table 3.1).

The camera produces a 2D image of the 3D plasma, collapsed in z . Provided the image is sufficiently circular one can use a center finding algorithm to get the radial intensity profile $I(r)$, which is subsequently fit to

$$I(r) = a e^{-\left(\frac{r-r_0}{b}\right)^k} \quad (3.1)$$

using a GPU accelerated Lev-Mar based code [30]. The fit parameter a is proportional to the density of the plasma, while b is an estimate for the plasma radius and r_0 indicates the $x - y$ position of the plasma in the trap. k is a number normally ranging from 2 to 6. n is high for cold plasmas which better approximate the “top-hat”-like profile often derived for $T = 0$. These parameters are used for computing the expansion rate (for example in Fig. 3.1) and for numerical solvers yielding a 3-D density and space charge profile (see Appendix C).

At the highest MCP gain, the camera (see below) should be able to resolve single plasma electrons [75]. This assertion is not consistent with current observations.⁴ At full resolution, the position and radius of plasmas with $N > 10^5$ may be reliably determined. $N \approx 10^4$ plasmas may be imaged by setting the CCD to bin pixels during readout ($8\times$ vertically and horizontally).

³This would not be possible without the SiPM even if N and T were both obtained with the FC. The FC works best for Tdiag with low phosphor voltage (to reduce microphonic noise) and very high MCP gain (causing saturation).

⁴The phosphor performance has probably declined after 6 years of service. Another screen recently installed at in ALPHA-g had previously been used in ALPHA-2 and was found to be much dimmer than the brand new ones.

Pixels	1376×1040
Readout noise (rms)	$5 e^-$
QE	50% at P-47 peak
Shutter speed	$0.5 \mu\text{s}$
Repetition rate	10 s^{-1}

Table 3.1: Properties of the PCO Sensicam. To see low- N plasmas requires binning up to $8\times$ in both dimensions (Pixels $\rightarrow 172 \times 130$).

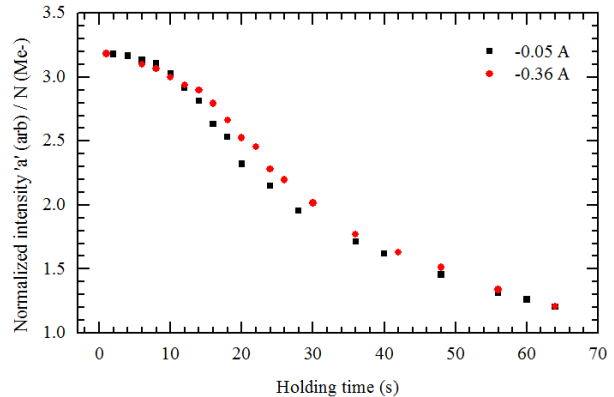


Figure 3.1: Expansion curve for $N = 10^7$ electrons at $B = 0.3 \text{ T}$. Normalizing the fitted intensity a to the measured number of electrons N reduces scatter due to MCP gain fluctuation and cycle to cycle variation in N . Legend values $\{-0.36, -0.05\} \text{ A}$ refer to the current in the gradient coil. The stronger gradient doesn't adversely effect plasma expansion in Cavity 1.

The camera has a fast frame mode allowing control of the delay and exposure to better than 100 ns. This can be used for investigating dump dynamics (see Limitations and Corrections in Section 3.3). The repetition rate of the camera and supporting software is too low to obtain multiple images during a single slow dump. ALPHA has switched to the ANDOR ZYLA which has a rep-rate about five times higher than the Sensicam. That is still too slow to do dump dynamics, but it could be useful for reservoir studies (Chapter 4).

3.2 Faraday Cup

Beam Blocking

If one zeroes all electrode voltages and turns on the egun a beam of electrons should pass straight through the trap and onto the MCP. Connecting the front of the MCP to an oscilloscope allows these electrons to go to the ground in the $1 \text{ M}\Omega$ scope impedance, inducing a voltage drop of $1 - 100 \text{ mV}$, indicating that $1 - 100 \text{ nA}$ of electrons are making it all the way through the experiment. This would represent a small fraction of the total emission current supplied by the circuit maintaining the -30 V egun bias; several microamps of leakage to the egun bias electrodes is normal, although there is significantly less at Berkeley than at CERN because the egun is in a stronger magnetic field. After turn-on, the beam current rises rapidly for about 15 s, then continues to rise less rapidly (Fig. 3.2). The shape of the

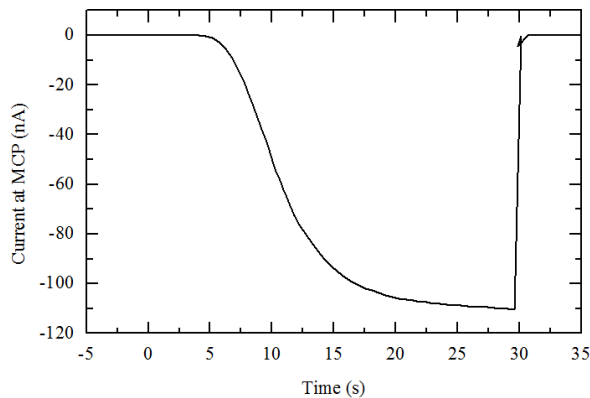


Figure 3.2: 30 s egun emission characteristic. The scope trace shows egun current straight through the experiment as the egun warms up. A steady heater current of about 1.2 A is applied at $t = 0$ and removed at $t = 30$ s. Current takes about 15 s to plateau, and continues to rise less dramatically after. MCP current falls to 1% within 10 ms of egun turnoff.

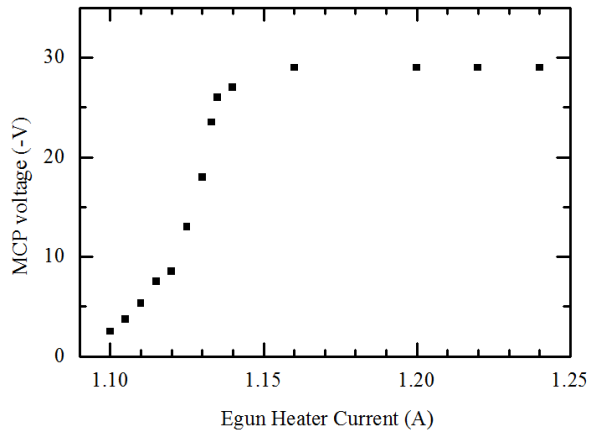


Figure 3.3: Filling the trap with 30 V of plasma. Egun bias is -30 V, MCP is connected to ground through the $1\text{ M}\Omega$ scope impedance. Heating up the filament increases the current to the scope until the MCP voltage approaches the egun bias. The corresponding space charge requires the existence of a two meter long plasma containing three billion electrons (see text).

current vs. time characteristic depends more on how much and how recently the egun has been on. Instead of trying to control this unpredictable behavior, one usually programs the loading sequence such that the egun warms up for 16 s prior to trapping so that the emission is (usually) in the plateau regime.

Since the electrons have approximately 30 eV of kinetic energy along z , applying -35 V to a few electrodes in a row is usually enough to stop them⁵ The scope current falls to zero. This procedure permits *in situ* testing of electrode connections and response time. Its primary usefulness is in determining whether an electrode is floating or partially shorted to another.

Even with all controlled potentials at zero, a beam will not form unless the egun bias $-V_b \geq 5$ V. This threshold value was significantly greater, close to 15 V, prior to the 2016 upgrade. As part of the upgrade all accessible parts of the egun chamber were coated in colloidal graphite. This suggests that the extra energy is required to overcome unintentional potential barriers near uncoated patches of copper, stainless, and aluminum. When such patches oxidize they can trap stray electrons from the egun. This is believed to be worse at low temperature as the wall-trapped electrons lack the energy to tunnel away from the oxidized zone.

⁵The on-axis potential is lower than the applied voltage in the vicinity of other grounded electrodes (see Appendix C). Usually -100 V is applied to a single electrode instead of -35 V to three.

Dump time	5 μ s
Capacitance	5 nF
Parallel Resistance	1 M Ω
Amplifier	sr560
Gain	20
Highpass	100 Hz
Lowpass	10 kHz

Table 3.2: Typical FC parameters which should result in a 5 ms pulse with amplitude 0.6 mV per $10^6 e^-$.

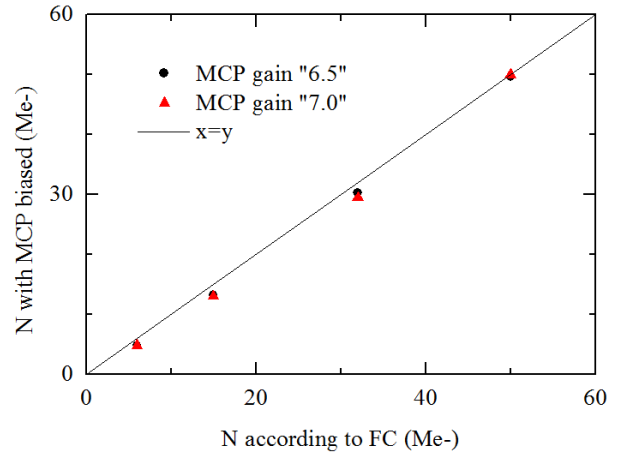


Figure 3.4: Using the biased MCP to count charge. A reproducible load is developed for $N = \{6, 15, 32, 50\} \cdot 10^6$ electrons. The MCP gain is linear and equal to $\{80, 260\}$ at control settings $\{“6.5”, “7.0”\}$.

To the extent that such barriers persist in the trap, the potential required to overcome them should appear as an offset between the asymptote (29 V) and the egun bias (30 V) in Fig. 3.3. In that figure, the measured voltage on the oscilloscope’s 1 M Ω input impedance is proportional to the plasma current ($V = IR$), which increases with filament temperature (controlled by heater current). The current can no longer increase when the voltage at the scope, and therefore at the MCP, exceeds the egun bias. At this point further egun emission must be suppressed by the presence of a plasma with space charge $\phi_0 \approx 30$ V. For the length $L \approx 1.8$ m from egun to MCP, this corresponds to $N \sim 30(\epsilon_0 L/e) \approx 3 \cdot 10^9$ electrons. The above analysis does not account for possible mirroring effects; the magnetic field is $10\times$ weaker at the MCP than at the electrodes.

Charge Calibration

For measuring N directly, the front of the MCP is connected to ground through a capacitance C . A voltage $V = Q/C$ appears on the capacitor when the plasma hits the MCP. The number N of electrons (charge e) is found via $V = Ne/C \approx 32 \mu$ V for $N = 10^6$ and $C = 5$ nF. The plasma is dumped quickly, as for imaging: about 5 μ s using a reed relay. Typical parameters are summarized in Table 3.2. If the circuit were purely capacitive, $V = Q/C$ so smaller C would offer increased sensitivity. In practice C is chosen to be at least 1 nF to reduce the effect of parasitic capacitance on the calibration⁶.

⁶In principle one can determine the parasitic capacitance C_p by repeatedly dumping the same number of electrons and plotting V vs. $C_{tot} = C + C_p$ for several values of C . C_p is typically about 300 pF when

N can still be determined when the MCP is biased for amplification. After using the FC to characterize a set of stable loads with a handful of N values, one can turn on the MCP, now connecting the charge amp to the phosphor line (through a HV capacitor), and measure the charge collected for each load as a function of MCP front-back bias (Fig. 3.4). It is advisable to iterate, switching back and forth between the two systems, to ensure the egun has not drifted. Egun drift is the dominant uncertainty in this calibration. Through software and hardware optimizations one can usually resolve $N \geq 100 e^-$ in this way, *in tandem* with a temperature measurement using the SiPM.

3.3 Temperature Diagnostic

Measuring the plasma temperature T may sound relatively straightforward. Indeed, if the plasma contains heavy ions like Be^+ or Ca^+ , one can unambiguously reconstruct the energy distribution $f(E)$ from the Doppler shift in the laser-induced fluorescence profile [45]. Free electrons, however, are invisible; their laser scattering cross section is smaller by about eight orders of magnitude.⁷ The standard technique for accurately measuring T of an electron (or positron or antiproton) plasma is the dump diagnostic [29]. The temperature of hot, tenuous plasmas may be measured to within a factor of two in most systems with minimal effort. Challenges arise in diagnosing

- i Cold plasmas ($T < 100$ K)
- ii Plasmas which contain too many or too few particles ($N > 10^6$ or $N < 10^4$)
- iii Temperatures with an accuracy better than 50%.

For reference, very brief explanations are given here; longer ones will be given below. Cold plasmas have a limited number of particles in a “Debye” cylinder. Plasmas with too many particles introduce non-negligible space charge corrections. Too few particles are difficult to detect. Accurate temperature measurement requires an accurate model of the on-axis confinement as a function of time.

Meeting these challenges requires extra detector sensitivity; reconstruction of trapping potentials at every instant of the dump; sophisticated fit routines [30]; consideration of equilibration and other timescales; and adiabatic and potentially space charge corrections. This is a lot of work for just one number, but as T is the most used variable in this thesis, it has proven necessary to invest considerable time and often daily attention to improving the scope and validity of the temperature diagnostic (T is also among the most important factors for experiments producing trappable antihydrogen). The following sections review the state of the art as implemented over the last five years at Berkeley.

obtained this way, but as C_p is an effective value which could depend on, for example, MCP temperature, it is safer just to add a nanoFarad or two to the circuit.

⁷The electrons are neither bound to a nucleus nor truly free. The superconducting magnet responsible for their cyclotron motion may be thought of as providing them with a weak attraction to their gyrocenter 10^{-8} times as strong as that of a nucleus. The trapped electrons are like “artificial atoms”, “visible” at

Thermalization

Electron-electron collisions allow the plasma to explore “configuration space,” where it rapidly settles on the maximum entropy distribution

$$f(E) \propto e^{-E/kT}, \quad (3.2)$$

also known as the Boltzmann distribution. The plasma is said to be “thermalized” and $f(E)$ may be justly characterized by the single number T . Loosely speaking, one can use the slow dump diagnostic to measure $f(E)$ and fit the data to an exponential function to obtain T . Before discussing the meaning of f and E in the trap, or the details of the dump procedure, it is logical to review the collective dynamics leading to thermalization.

The collisional thermalization rate $\nu \approx nvb^2 \approx 100 \text{ s}^{-1} \cdot T[\text{eV}]^{-3/2} \cdot n[10^8] \approx 10^5 \text{ s}^{-1}$ or $\nu^{-1} \approx 10 \text{ } \mu\text{s}$ for typical density $n \approx 10^8 \text{ cm}^{-3}$ and temperature $T \approx 100 \text{ K}$. But the plasma takes far longer than $10 \text{ } \mu\text{s}$ to thermalize. There are several complications to consider.

- i This is the unmagnetized collision rate $\nu_{\parallel\parallel}$ which applies to exchange of energy in the z direction due to collisions from bounce motion in the z direction. Purely 1D two-body collisions cannot thermalize the plasma because the two colliding electrons simply exchange velocities; $f(E)$ does not change. 1D three-body collisions can change the distribution function, but the three-body rate is not well defined [11].
- ii 3D (magnetized) collisions mix transverse and axial energy at the rate $\nu_{\perp\parallel}$. In general $\nu_{\perp\parallel} \leq \nu_{\parallel\parallel}$, being much lower when the magnetic field is so strong that $r_L < b$. This was first shown by O’Neil and Hjorth [70] and demonstrated experimentally by Beck and Fajans [12].
- iii Any of the collisions discussed above only mix energy locally, at the site of the collision. Energy diffuses to different radial locations in the plasma at the long-range rate $\nu_{LR} \approx \nu \cdot (\lambda_D/r_p)^2$, as shown by Dubin and O’Neil [26] and demonstrated experimentally by Hollman et al. [46].
- iv The plasma temperature is not well defined until thermalization is complete, but it is being used to estimate a typical electron speed $v_t = \sqrt{kT/m}$. An open question is to what extent thermalization of the high E part of f often takes longer. For example, the experiments in Chapter 7 suggest that high E electrons produced by RF noise can take 1 s or more to relax back into the Maxwellian.
- v Geometry driven instabilities and electrode noise can cause resonant heating, permanently or intermittently interrupting the above processes (see Chapter 7).

There is no reason that thermalization should occur faster than the slowest of the timescales indicated above. Depending on plasma and trap parameters, the plasma may not be characterizable by a single temperature T until it has been trapped for many collision times. This

frequencies 10^8 times smaller than optical radiation: they scatter microwaves. It is possible that information about $f(E)$ could be extracted from microwave spectra; see Chapter 6.

is often an inconveniently long time for the cavity cooling studies, and has contributed to erroneous estimates of the cooling rate in prior work [76].

Dump Rate

Now suppose that the plasma has thermalized and is just sitting in the trap cooling down. At some point one wants to know T . The effect of cyclotron cooling is to remove energy from all but a handful of transverse degrees of freedom at a nearly equal rate Γ which is typically of order 1 s^{-1} . It was shown above that thermalization happens a thousand times faster than this. Thus the electron energy distribution remains nearly thermal as the plasma cools: $f(E) \propto \exp[-E/kT]$, with T decreasing slowly in time. In order to avoid extra cooling during the dump diagnostic, the dump rate must be faster than the cooling rate. The entire process must take 100 ms or less.

The conventional wisdom is that the dump rate dV/dt must be faster than collisions but slower than the bounce frequency ω_z [11]. See Fig. 3.5. Although this rule of thumb is often stated, it has not been verified by experiment. The two extremes are discussed individually below.

$$\nu_{\perp\parallel} \ll \frac{1}{T} \frac{dV}{dt} \ll \omega_z$$

dense hot plasma $\longleftarrow \bullet \longrightarrow$ short cold plasma

Figure 3.5: Classic rule of thumb for the dump rate. Arrows indicate the plasma regime in which the indicated time scale is supposedly problematic.

Evaporative cooling: The first 10% of particles which escape have the highest energy. The plasma will begin to rethermalize to a lower T within $\nu_{\perp\parallel}^{-1}$ (or perhaps faster via 3-body collisions), causing undesired evaporative cooling. In order to obtain three e-foldings of temperature information before the distribution changes significantly requires $3k_B T = \Delta E = e\Delta V = \nu_{\perp\parallel} \cdot dV/dt$ or $dV/dt \approx 3 \text{ V ms}^{-1}$ for typical density and $T \approx 1 \text{ eV}$. This is comparable to the dump speed at Berkeley, but ALPHA dumps can be a factor of ten slower. In practice the high rate quoted is seldom necessary. With the current detection system one can easily detect the first few $k_B T$ -worth of electrons, which constitute a negligible fraction of the total energy of the plasma.⁸

Bounce time: It takes a finite amount of time for a given electron to “go find out” that the confining potential has changed. In the worst case, the electron will be moving away from the barrier just as it falls to that electron’s escape energy. The electron must then

⁸Even in experiments where this is not true, other limits to the validity of the extraction data will arise before evaporative cooling becomes important, such as the diocotron instability due to the center of the plasma coming out before the rest. Nevertheless, Cassidy et al. [16] have claimed that the apparent variation of T with dump rate may be useful for determining $\nu_{\parallel\parallel}$.

perform one last round trip across the plasma “for nothing” and come out late. It will be counted with the electrons which escaped with an energy $\sim dV/dt \cdot \omega_z^{-1}$ lower than its own. That is the usual story. But if this were all that happened, the net effect would be to smear and delay the entire distribution by the same amount. What is actually observed, as $(1/T) dV/dt \rightarrow \omega_z$, is a dump wave [67]. Evidently the dominant factor limiting the dump rate is not the mechanism described above. Rather, it seems that the center-of-mass bounce motion of the whole plasma (also at ω_z) periodically reduces the effective confining potential as the whole plasma rides up over the hill.

The theory-based constraints on dump rate usually given are of less immediate interest to the experimentalist than the following hardware-based constraints.

Digitizer speed: The 100 MS/s digitizer used at Berkeley can acquire ten data points per e-folding in the example just given. Digitizers as slow as 1–2 MS/s are often used for Tdiag and necessitate much slower dump ramps.

Memory: Acquiring that quickly means that a 10 ms trace will contain 10^6 samples or about 10 MB of data—taking a shorter trace would require optimized timing, with each optimization only valid for a certain range of N and a certain $V(t)$. A 10 MB trace can take seconds to manipulate using LabVIEW. The reservoir ECR implementation foreseen for the mirror ramps in ALPHA-g will require much faster processing, possibly a few milliseconds (see Chapter 6). One might gain sufficient speed by using an AB trigger (A = dump marker, B = rising edge of extraction signal) to record only the most interesting 1% of the trace. But one inevitably finds reasons to regret throwing away data.

Pileup: Less sensitive detectors, like the Faraday cup, benefit from a higher dump rate $(1/T)dV/dt \gg \tau^{-1}$, where the forgetting time $\tau = RC$ for the faraday cup. The ensuing pileup is necessary to boost the signal out of the noise.

Electrode noise: Noise on the electrodes can stimulate intermittent, bounce-resonant plasma emission during the dump (see Chapter 7). Dumping faster usually ameliorates this effect by reducing the amount of time the particles are resonant with a noise peak.

Measuring $f(E)$

The distribution function f determines the shape of the extraction signal. $f(E)\Delta E$ is approximately the fraction of plasma electrons having energy in an interval of width ΔE close to E . The smaller the interval chosen, the better $f(E)\Delta E$ estimates this fraction (think of the standard bars on a smooth curve figure from Calculus I). As the blocking potential falls, electrons begin to escape (Fig. 3.6). Those with more energy (farther left on the graph) escape earlier. For a hot plasma that’s all there is to it: the plasma current nicely reproduces the distribution function in Eq. 3.2. For the data in Fig. 3.7, the extraction begins to deviate significantly from $f(E)$ at about 0.63 V or about 10 μs after the arrival of the first electron. By this time electrons containing close to two decades (four e-foldings) of temperature information have arrived. That is sufficient for a fit with an uncertainty $\delta T/T \approx 20\%$ despite the fact that less than 0.1% of the plasma has been extracted (Fig. 3.8).

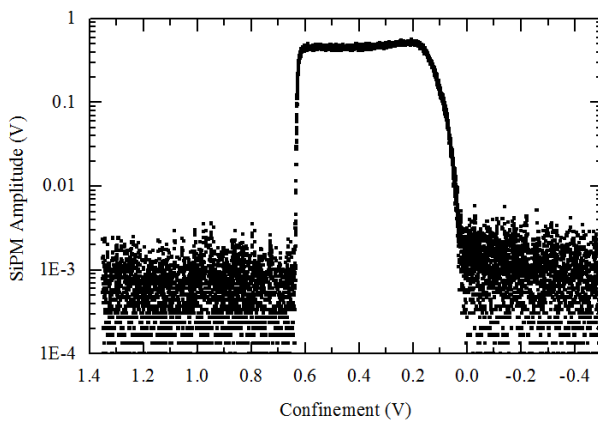


Figure 3.7: Extraction trace for a cold, $N = 3 \cdot 10^6 e^-$ plasma. This is the “same” plasma as in Fig. 3.6 after 8 s of resonant cooling.

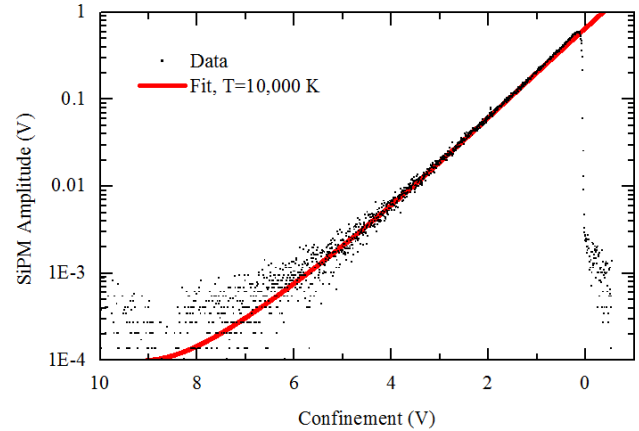


Figure 3.6: Extraction trace for a hot, $N = 3 \cdot 10^6 e^-$ plasma. y axis is the voltage on the SiPM detector, which has a forgetting time $\tau < 1\mu s$ or 1 mV on this scale (see next section). It is thus a good approximation to instantaneous plasma current.

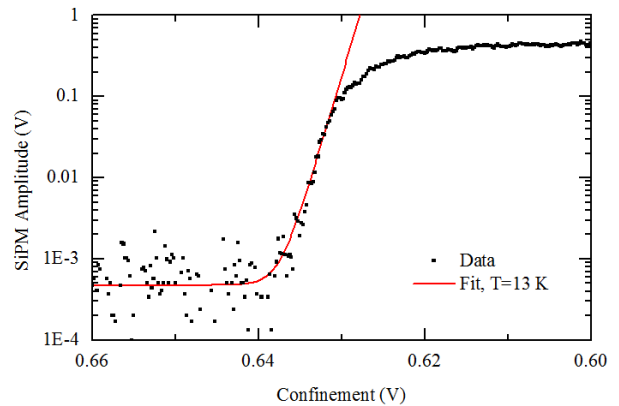


Figure 3.8: Expanded version of previous figure, showing temperature fit. Fits are obtained using variable ROI endpoints, then averaged, weighted by $1/\chi^2$ (see text). The weighted deviation is about 3 K.

After this point the extraction signal flattens, and particles escape at a nearly constant rate. Here are two hypotheses to explain the flattening effect.

- i The plateau represents a balance where the space charge is falling almost as fast as the blocking potential [29]. This is a plausible and robust mechanism because (a) it is consistent with the analytic model of Evans [30] predicting the point at which space charge depletion should cause the extraction curve to begin to fall, (b) the mechanism achieves the observed stability via a feedback loop, (c) something of this kind must be happening since electron arrivals continue until the well is no longer able to trap them.
- ii Electrons near the axis escape first, so that the plasma becomes hollow. The diocotron instability repopulates the core, from which particles continue to escape, but the instability is rate limited, perhaps by the conditions producing the instability in the first place.

The first hypothesis is believed to dominate in most parameter ranges. The effect invoked by the second hypotheses does often seem to contribute to the extraction profile, but apparently not until much later in the dump (cf. Fig. 7.4). Both hypotheses are consistent with the near-absence of flattening for hot plasmas (Fig. 3.6), which are often log-linear all the way to the end.

Software Implementation

T is determined by repeatedly fitting the rising part of the extraction trace, looking for the best place to cut off the latter part of the data. This should be where χ^2 is minimized for the model

$$I(t) = G \cdot f(E(t)) \frac{dE}{dt} \propto a + be^{ct} \quad (3.3)$$

where I is the current in a photomultiplier looking at the phosphor screen. This is proportional to the plasma current hitting the MCP. The fit parameter a is a DC offset, b is the response to a single plasma electron, and $c = (e/kT)(dV/dt)$. The routine calls a GPU-accelerated exponential fitter [30] for each of about 100 window selections. The resulting fits are combined, weighted by $1/\chi^2$. With reasonable initial guesses for a , b , and c the entire routine takes about a second. Unfortunately the fitter requires some ROI-selection parameters to be tuned before it can be unleashed on a batch of traces with no further human input. The most problematic of these parameters is the ROI-stop trigger, taken somewhere between 10% and 100% of the peak amplitude. Cold plasmas are prone to developing “ears” (see Chapter 7) and require a much lower threshold, while hot plasmas may have poorly thermalized high-energy tails, requiring this threshold to be set as high as possible.

Limitations and Corrections

Several complications remain to be addressed. The model given above does not account for them. They appear as correction factors and limits to the usable ROI.

Space Charge

The exponential increase in escaping charge vs. time may continue, for a hot plasma, until all of the particles have escaped. For a cold plasma, the exponential is soon flattened and the extraction typically enters a “constant current” mode. It is useful to determine the parameter values for which this should be a problem, and in particular to estimate how the effect can change the apparent temperature.

The electrostatic potential seen by the electrons $\Phi = \phi_t + \phi_s$, where ϕ_t is the trapping potential due to the voltages on the electrodes and ϕ_s is the space charge potential due to the presence of other plasma electrons. At $r = 0$, the space charge potential $\phi_s \approx \phi_0 = (-Ne/4\pi\epsilon_0 L)(1 + 2 \ln(r_W/r_p))$ for a long cylindrical plasma, as can be shown using Gauss’s law.

This means that a confined electron plasma is, to first order, sitting on top of a DC offset proportional to the number of electrons in the plasma. The energy required by an electron to leave the well changes during the dump ramp at the rate $-dE/dt = e d(\phi_t + \phi_s)/dt < e d\phi_t/dt$. Escaping charge reduces $|\phi_s|$, making the dump effectively slower. The temperature will appear higher by approximately T times $\Delta\phi_s/\Delta\phi_t \sim (\Delta N/N)(\phi_0/\Delta\phi_t)$, where the Δ correspond to the time Δt when the first few kT of particles are arriving (for example $\Delta\phi_t \sim 3kT$).

A subtler source of nonlinearity has to do with the spatial dependence of ϕ_s . Davidson showed that at equilibrium the exponent in the Boltzmann factor is nearly constant for all r and z inside the plasma, implying constant density [22]. A constant density cylinder of electrons changes the electric potential near $r = 0$ by $\Delta V \approx \phi_0 + (r/2\lambda_D)^2 kT$. The electrons within a few Debye lengths of $r = 0$ are, for the purpose of escaping along z , sitting at a total potential energy $-e\Delta V$ which is higher by $\mathcal{O}(kT)$ than for those which are many Debye lengths away. The highest energy electrons at $r = 0$ escape first. Then the electrons at $r = 0$ with $1 kT$ less of energy will escape, along with electrons at $r \sim \lambda_D$ which have the same energy as those at $r = 0$ which escaped earlier. In other words, in analyzing $\Phi(r, t)$ along z it is possible to conflate a spatial effect with the time-dependent effect desired. Evans worked out an analytic expression describing this process [30]. That expression was used by Evans to quantify the absolute limit on the usable range of Tdiag. The limit occurs in the case where there are too few particles in the Debye cylinder to produce enough log-linear data for a good fit and corresponds to a temperature

$$T = 8 \text{ K} \left(\frac{1 \text{ cm}}{L} \right) \left(\frac{0.1}{\epsilon} \right)^2 \quad (3.4)$$

where ϵ is the desired fractional uncertainty in T and L is the plasma length. This expression assumes the signal to noise is high enough that every electron is counted. For a 4 cm plasma, $T < 2 \text{ K}$ cannot be determined to better than $dT/T = 10\%$ using only the linear part of the extraction. Since this limit is based on shot-noise statistics, it could be improved somewhat by averaging several plasma traces together.

Both the sources of nonlinearity just described tend to make dN/dt smaller. They must consistently appear as deviations of I downward, compared to Eq. 3.3, as more charge is extracted. To the extent that one can identify the slope of the linear region (on a log scale) before it the curve is perturbed significantly downward, the space charge correction does not affect the measured T .

The foregoing explains why higher sensitivity (to see the earliest escaping particles) is so valuable for measuring low T . The lower the T , the smaller are both $\Delta\phi_t$ and λ_D , discussed above. As T is reduced, the onset of space charge corrections occurs earlier. Ultimately a limit should be reached (Eq. 3.4) where even the most sensitive detector cannot reliably measure the plasma temperature. This limit is at least a factor of 2 lower than the temperatures measured in this thesis.

Adiabatic Expansion

The plasma expands in z as the blocking potential falls. The fractional change in length $\Delta L/L \sim 1$ and is slow compared to the bounce: $L(dL/dt)^{-1} \sim 10 \text{ ms} \gg 100 \text{ ns} \sim \omega_z^{-1}$. Thus, before including the effect of collisions, this process should conserve the first adiabatic invariant $j = \oint v_z dz \approx 2Lv_z$. Since $Lv_z = \text{cst.}$ for all v_z , changing L scales the whole velocity distribution the same way as the thermal velocity $v_{\parallel t} = \sqrt{kT_{\parallel}/m}$. Then $L^2v_{\parallel t}^2 = \text{cst.}$ or $L^2T_{\parallel} = \text{cst.}$ In differential form $2L dL T_{\parallel} = -L^2 dT_{\parallel}$ for changes in T_{\parallel} in response to changes in L . As long as the density or temperature is not too low and the magnetic field is not too great, a 10 ms dump will be slow compared to $\nu_{\perp\parallel}$. In this case the energy added to or removed from T_{\parallel} will be immediately mixed into the two other degrees of freedom T_{\perp} . One can then modify the differential form of the adiabatic invariant: $(1/3) \cdot 2L dL T = -L^2 dT$ since 1/3 of the motional degrees of freedom shares the change with the other 2/3. Integrating this expression gives the usual result for a three-dimensional⁹ adiabatic expansion $T_i = T_f(L_f/L_i)^{2/3}$, or in words, the initial (*in situ*) temperature is the final (measured) temperature times a power of the ratio of the initial and final lengths. If $L_f/L_i = 2$, the temperature will appear to be 6 K even though the plasma was 10 K prior to the dump. Determining this correction factor (10/6 in this case) requires knowledge of the initial and final plasma length. L_f can be read off from a plot of $\Phi(z)$ if the final space charge offset ϕ_{0f} is known; it can usually be measured simultaneously with T using the SiPM. L_i and ϕ_{0i} cannot be deduced from the extraction trace, but if N and r_p are known one can find them using a self-consistent numerical solver (Appendix C).

3.4 Photomultiplier

A major advance in the sensitivity of the temperature diagnostic grew out of Alex Povilus's idea to use the light from the phosphor screen as the time-dependent signal. The ef-

⁹For the lowest N plasmas studied in this thesis the density can fall to $n \leq 10^6$ and the exponent is somewhere between 3-D and 1-D values, 2/3 and 2.

fort began with a photodiode project which the author shared with an undergraduate shortly after joining the lab. Eventually the team hit on the right combination of circuit topology and Fresnel optics to obtain a factor of 2 greater sensitivity than the Faraday cup with the new system. The author had worked extensively with photomultiplier tubes (PMT's) as an undergrad and soon replaced the photodiode with a venetian-blinds PMT, and later a silicon photomultiplier (SiPM). The resulting system is better. At full MCP gain, the sensitivity of the SiPM is typically 1–2 orders of magnitude greater than that of the FC. The new detection system also enables characterization of the plasma in ways not convenient or not possible with the Faraday cup.

All data taken after 2015 used the SiPM instead of the standard Faraday cup readout. 2015 data (including the first cavity cooling results) was taken using a PMT. Thus, the majority of the data presented in this thesis benefits from the new diagnostic tool.

The SiPM enables the measurement of lower temperatures. It also enables temperature measurement for plasmas with over an order of magnitude fewer electrons. This is the primary function, and it shall be presented in a forthcoming article.¹⁰ But there are other benefits to using the SiPM. Figs. 3.9, 3.10, and 3.11 showcase some of the bonuses of the SiPM diagnostic. These include:

- (Fig 3.9) It is possible to operate the MCP at fairly high gain without saturating the SiPM. This is because the SiPM measures plasma current and not integrated plasma charge (like the capacitor in the Faraday cup diagnostic). The SiPM signal provides the complete history $dN/dt(t)$, instead of just the first few e-foldings. The extra information can be used, for example, to calibrate the confinement potential as a function of time. When the confinement potential reaches zero and no plasma remains in the trap, the SiPM signal should drop abruptly to zero. Although the time-dependent confining potential in the trap can be determined externally if the electrode voltages are well-calibrated and filtering effects are properly accounted for, still, the SiPM measurement provides a fast, reliable answer. It also allows one to test the hypothesis that no plasma remains in the trap when the confinement is nominally zero. Exceptions have been observed.
- (Fig. 3.10) The camera is often used in tandem with the SiPM (not possible with an optimized Faraday cup), providing information about the plasma location and shape. While the slow dump, used for Tdiag, can cause distortion of the plasma image due to the diocotron instability, these images still provide a lot more information than a blank screen. In the image shown, the plasma appears smaller than it actually is because during a slow dump electrons tend to escape within a few Debye lengths of $r = 0$. In the case of a plasma whose radius is comparable to the Debye length, the slow-dump image can faithfully reproduce the fast-dump image. If the plasma is very dense, cold, or off-axis, there will be extra features in the image due to the diocotron instability. However, if the camera shutter is timed so that only the first 10% of escaping particles are imaged, accurate position information should still be obtainable.

¹⁰As is also the case for the forthcoming article on ECR, any unpublished data that is anticipated to appear in print will not be presented here.

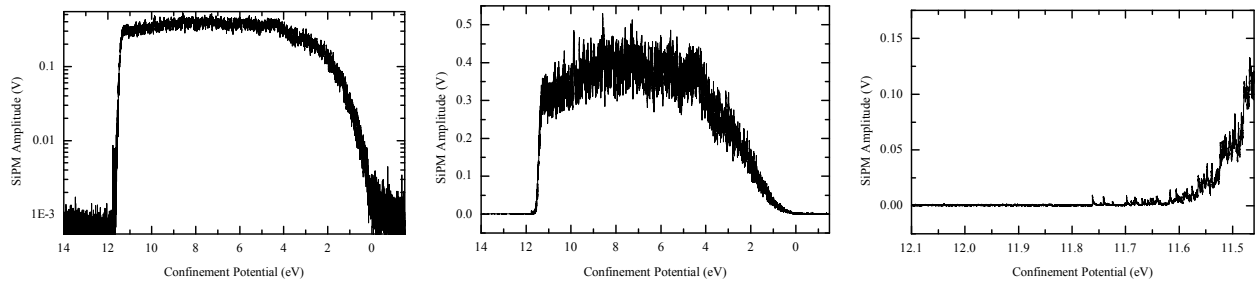


Figure 3.9: Extraction trace acquired using original SiPM (October 2015). Left panel demonstrates the unambiguous identification (in time) of the well-bottom as the moment when charge stops arriving and the signal falls to zero. Middle panel is the same trace on a linear scale. Right panel is a portion of the same trace with expanded linear scale showing the arrival of the first few plasma electrons.

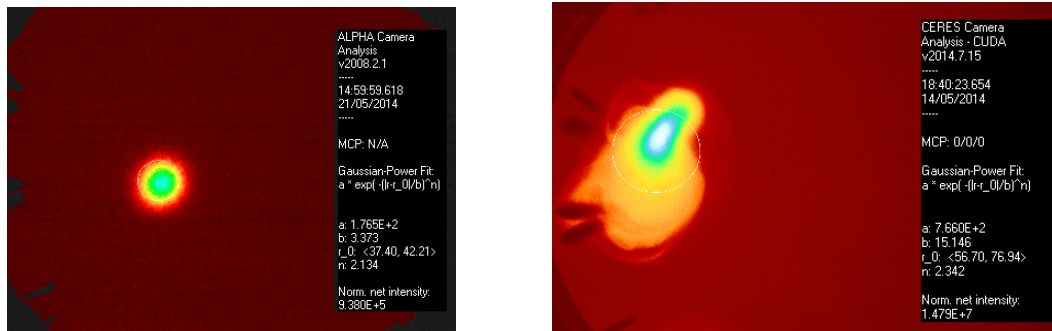


Figure 3.10: Plasma images acquired while dumping slowly to measure the temperature. The slow extraction allows plasma instabilities to develop during the dump. This distorts the image. However, some information, such as approximate plasma size, density, and position in the trap, is often still retrievable. The image on the left was obtained by Alex Povilus. The image on the right displays some signs of instability during the slow dump.

(Fig. 3.11) The SiPM can detect single plasma electrons. In Fig. 3.9 a few very small hits can be seen prior to the exponential rise. Given the work in Ref. [16], one should not assume immediately that these correspond to individual electrons. Fig. X3 displays the SiPM signal for a very slow extraction of very few electrons. $N \approx 100$ was measured simultaneously using the Faraday cup with the MCP at full bias, as discussed at the end of Section 3.2. The SiPM records approximately 60 isolated spikes. This number represents the excess over background using pulse height analysis, and is observed to vary by about \sqrt{N} in multiple extractions, as expected for Poisson statistics. Thus, while in our implementation the SiPM doesn't record every isolated plasma electron which hits the MCP, it does record roughly half of them. This is due to the small number of photons, roughly five, which arrive at the SiPM per plasma electron. The sensitivity could be improved with more advanced optics if necessary.

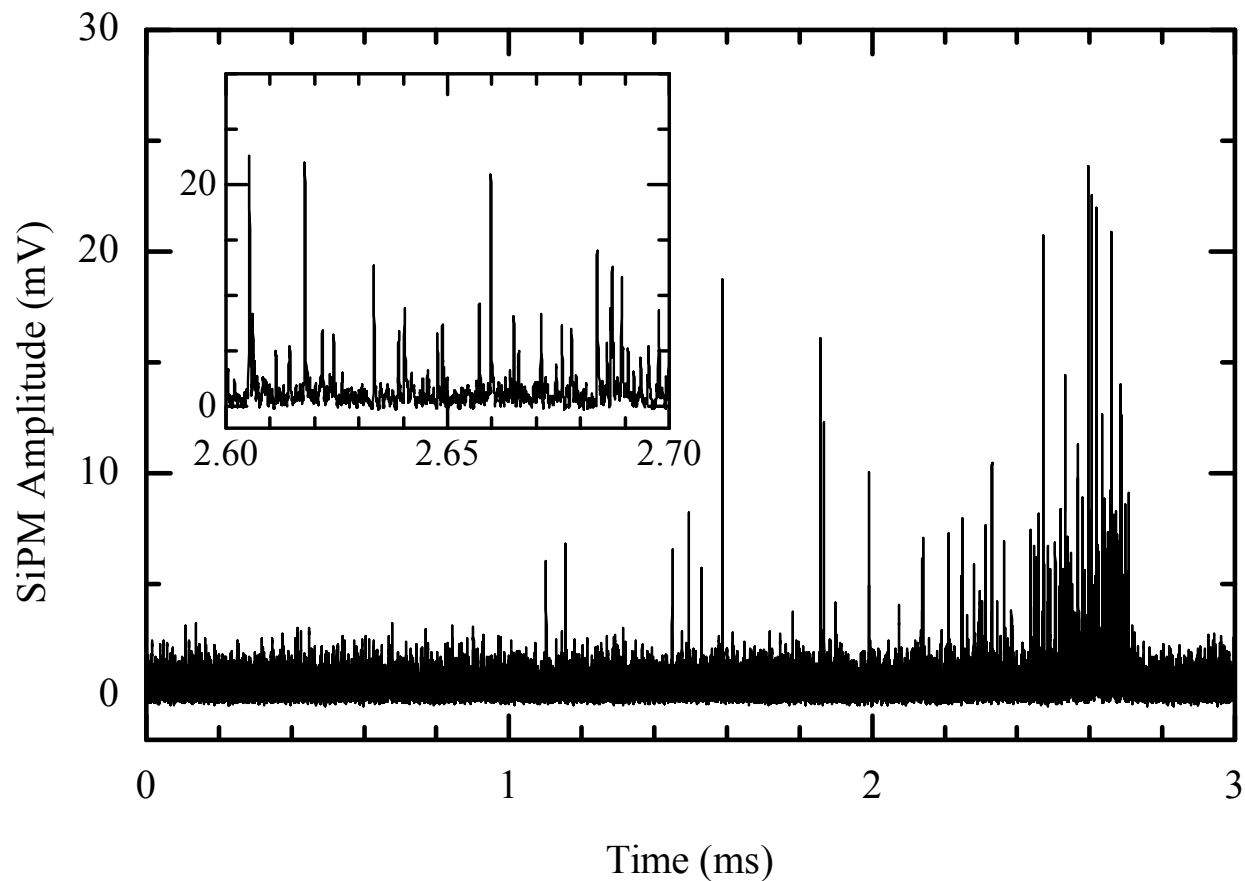


Figure 3.11: The last low- N trace of 2019. The energy distribution may eventually relax to a Maxwellian (see Section 7.1), but it is clearly influenced by Poisson statistics. The inset shows that for this trace the events seem to remain well separated. However, there is a hint of correlation at the level of 2–3 electrons, which also appears in the pulse height analysis (see forthcoming paper).

Chapter 4

Plasma Reservoir

This chapter reports a technique for quickly generating a sequence of small “target” plasmas by repeatedly pinching off the end of a large “reservoir” plasma. Doing so greatly improves the data taking rate relative to the standard catch, hold, dump cycle where the plasma is “caught” from the hot filament of the egun.

There are additional advantages to using the egun less often. The egun compromises the vacuum, both as a long-term source of slowly released thermal energy, and as a short-term emitter of hot gas during plasma loading. Because of the latter effect, even a well-tuned loading protocol can abruptly stop working, requiring egun parameters to be adjusted in a guess-and-check fashion. Another problem is that the ES-015 and similar models require about 16 s of power before they begin to approach operating temperature in the cryogenic environment. During this time electrons slowly accumulate, bouncing $\mathcal{O}(1\text{ m})$ between a region of high field and good vacuum, the trap, and the opposite of that, the egun chamber.

The Fajans Group has recently developed two distinct responses to the loading problem. One of them, called SDREVC, is the focus of another thesis [15]. SDREVC is a way to get a cold, reproducible plasma starting from a problem plasma with at least as many particles as the desired final state. The method can only produce plasmas with at least 10^6 particles or so¹ and typically requires an extra 20 s of prep time².

For taking data quickly there is another approach called the plasma reservoir: use the egun to produce one reservoir plasma, then extract many smaller plasmas from the reservoir. In an experimental scan, each target plasma is briefly subjected to slightly different conditions (magnetic field, well depth, microwave frequency) before it is dumped and the next one extracted from the reservoir. One can thereby obtain over a hundred data points in a minute, the time it previously took to obtain one or two points. The data is also more consistent because all the targets come from a single reservoir in a sequence of nearly identical electrostatic perturbations.

¹Below $N = 10^7$ the plasma becomes increasingly sensitive to the details of the well it finds itself in; a successful SDREVC protocol has not been reported for $N < 2 \cdot 10^6$ leptons.

²For many applications the extra time is not an inconvenience, for example if one is waiting for positrons to accumulate somewhere else.

This technique originated at Berkeley in March 2015. That October the BASE collaboration at CERN published an article [84] entitled “A Reservoir Trap for Antiprotons.” Unlike the plasma reservoir, BASE’s reservoir of 100 antiprotons works in the single particle regime and serves a different purpose: conserving a precious resource, antiprotons, which can be removed from the reservoir one particle at a time.

The predecessor and likely the inspiration for the reservoir technique was the repeating positron beam experiment of Weber et al. at UCSD [94]. Fig. 4.1 appeared in Surko’s presentations at the 2012 Winter School for Trapped Charged Particles at Les Houches, a triennial event regularly attended by members of BASE and ALPHA. The San Diego group repeatedly extracted but did not recapture a sequence of 20 beams of charge having nearly identical radial density profiles. They did this with a fast pulser on a confinement gate in an effort to avoid collisional effects and produce a short bunch. The mathematical analysis of this process is identical with that used to describe particle release in the plasma temperature diagnostic [30].

In the following sections, the use of the reservoir technique for locating cavity resonances will be described, followed by the modifications to the protocol which are useful for doing ECR magnetometry.

4.1 Hot Targets for Cavity Cooling

The original, quick and dirty reservoir protocol will be described here. Fig. 4.2 displays the sequence of on-axis potentials comprising the essential steps. The reservoir plasma is held in a deep well while the target catch well is formed; the reservoir is elevated until it begins to spill out the side; the target well is deepened to catch some of the escaping electrons. The reservoir must be raised a little higher each time to compensate for its diminishing space charge. This protocol pulls the hot tail out of the reservoir and into the target well, but keeps the reservoir itself hot by the repeatedly exposing it to poor confinement conditions.

The resulting target plasmas have about 1 eV (average kinetic energy per electron) and typically $1-3 \cdot 10^5$ particles (Fig. 4.3). It is not clear what makes this the “right” amount to extract with the hot-target method, but the sequence isn’t reliable otherwise. If one tries to scoop too few electrons into the target, the reservoir crashes: scoops get progressively hotter

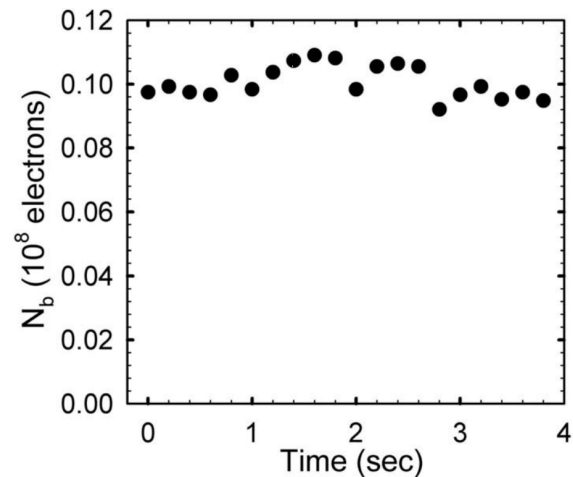


Figure 4.1: Repetitive pulsed extraction from a positron plasma at UCSD. Was this the inspiration for both groups which subsequently developed charged particle reservoirs? Figure from Ref. [94].

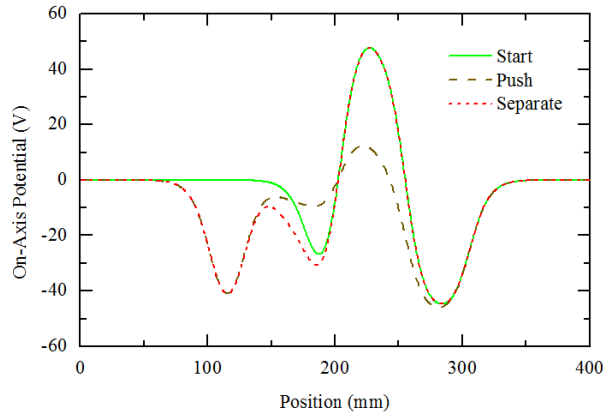


Figure 4.2: Sequence steps from the first reservoir sequence, producing hot target plasmas with $N \sim 10^5$. The reservoir is pushed to a more negative potential until it spills over into a shallow target well. For each successive scoop, the reservoir has to be pushed further to compensate for decreasing space charge.

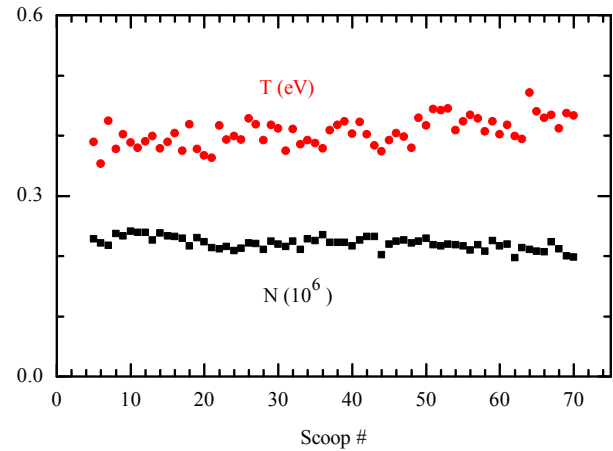


Figure 4.3: Typical T , N for about 70 scoops from a hot reservoir. The first few scoops are tossed because the reservoir needs to be “excited” before N and T can stabilize. This is not the case for a cold reservoir, Fig. 4.6.

and rarer until there is nothing at all. Conversely, large scoops tend to be colder and swiftly deplete the reservoir.

For some cavity modes, 10^5 electrons is still too much (unless at a node or under a gradient; see next chapter). On one of Nathan’s visits to Berkeley he resolved to modify a reservoir sequence to obtain targets in the $10^4 - 10^5$ range. By adding a larger barrier which reduced particle loss during the transfer step, a somewhat stabler reservoir resulted, making it possible to skirt the low- N edge more closely.

4.2 Cold Targets for Magnetometry

Initializing the target with a high T maximizes the signal-to-noise for the cavity measurement because one is looking for cooling. The opposite is true for microwave heating: target plasmas should start out as cold as possible. Reducing the target temperature benefits ECR in multiple ways, which shall be discussed shortly.

A hot target may be evaporatively cooled to produce a cold one. This was the method employed in earlier reservoir ECR sequences at CERN. Efforts to minimize the duration of the EVC step accidentally led to the discovery of a new effect, called Mirror-EVC (see Chapter 7). EVC is not ideal because it expands the target and takes more time than other parts of the sequence.

It is better to start with a cold reservoir³ and scoop out plasmas in a way that does not

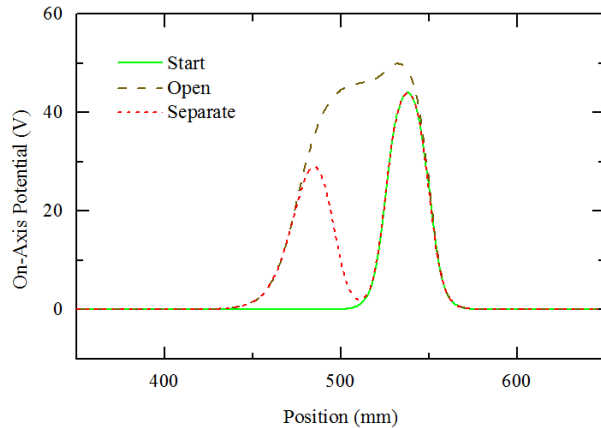


Figure 4.4: Sequence steps from a recent reservoir sequence, producing cold target plasmas with N tunable from 10^4 to 10^6 electrons. Instead of being pushed, the reservoir is gently expanded into a biased well which holds most of it away from the target side. Tuning how much is held ‘away’ prior to the separation step determines N of the target. For each successive scoop, the bias on the left is made more positive by a constant amount, for example, 0.050 or 0.025 V per scoop in the sequence behind Fig. 4.6

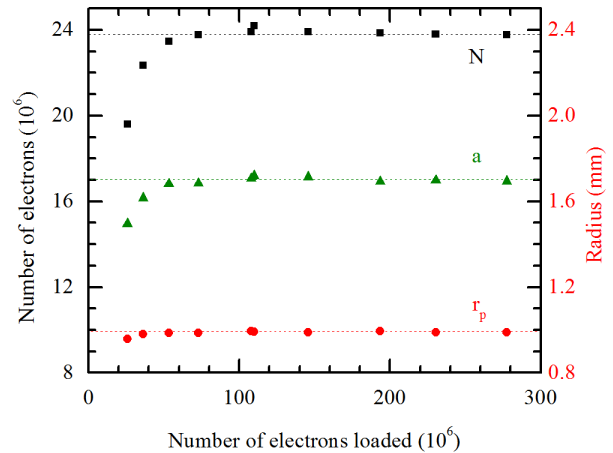


Figure 4.5: Parameters of the reservoir plasma after SDREVC. The fitted image intensity $a \propto n$, the plasma density. The small fluctuation in a and N for the data point at $x = 110$ may be due to drift in the MCP gain rather than actual variation in the produced plasma: notice that this does not effect r_p . Dotted lines of zero slope are shown for reference.

add excess energy to the reservoir or the target. Fig. 4.4 shows the sequence of steps used to do this.

For use on ALPHA it is necessary that the method be robust; one can’t be adjusting the potentials every week if a parameter is drifting. The reservoir itself became the product of an SDREVC protocol. Later at Berkeley, it seemed that the SDREVC step was worth implementing because of the premium on reproducibility for precision magnetometry runs. This required a modification of Carruth’s technique for use at a lower magnetic field than the 1 or 3 T which are customary at CERN, where cyclotron cooling provides the damping necessary for the rotating wall technique. SDREVC is performed at Berkeley without the benefit of cyclotron cooling by adding an initial $\mathcal{O}(1 \text{ s})$ EVC step to reduce the reservoir-to-be from $N \sim 2 \cdot 10^8$, $T \sim 1 \text{ eV}$ to $N \approx 8 \cdot 10^7$, $T \approx 0.05 \text{ eV}$, then performing SDREVC

³For a diocotron-related study, it was necessary to produce targets with very low N , but still high enough n for imaging. A colder reservoir was found to produce targets with smaller radius r_p . Although this did not constitute a systematic study, the findings were consistent with the scaling $\min\{r_p\} \propto \sqrt{T_{res}}$. This suggests the lower bound on r_p is a few λ_D ; cf. [30], [94], and the discussion of shielding in Chapter 3 for why this might be.

with more aggressive evaporation, ultimately removing all but the coldest $3 \cdot 10^7$ particles. As shown in Fig. 4.5, this worked for all N produced by the egun provided $N > 10^8$ or so.

In addition to producing colder, denser targets, the cold, SDREVC reservoir is also better behaved and easier to model. The number of extracted electrons is approximately proportional to the voltage step and can be tuned easily between $N < 10^4$ and $N > 10^6$ electrons per scoop.

In Chapter 6 the reader will see that shorter plasmas are better for precision ECR magnetometry. By starting with a cold reservoir and also evaporatively cooling the target, one can reach very low temperatures (see Fig. 4.6). If such a target is moved carefully into a deep well, it may enter an unusual regime for electron plasmas where the aspect ratio (L/r_p) < 1 . The laser-cooled-ion-plasma community refers to plasmas with this geometry as pancake plasmas. Figure 4.7 displays results obtained using the Poisson solver discussed in Appendix C which show that $L \propto \sqrt{T}$ for $N \sim 10^3$ electrons. The potentials used by the solver correspond to two of the well shapes used in Chapter 6.

To get from the EVC well to the deep wells considered here requires significant longitudinal compression. A natural question is whether, after throwing away so many electrons and then adiabatically heating the target via compression, the remaining object is still a plasma. In fact, if done correctly EVC reduces T much faster than N or n (because the hottest 10% of particles carry more than 10% of the total energy). 3D adiabatic compression in a strong magnetic field also decreases λ_D . This at least is easy to show: $T \propto L^{-2/3}$ while $r = \text{const.}$ so $\lambda_D \propto T^{-1/4}$ for this process. However, by comparing the 30 and 56 MHz curves in Fig. 4.7, one can see that the ratio L/r_p decreases for deeper wells.

Another concern may arise regarding the accuracy of the temperature measured for a pancake plasma. Eq. 3.4 seems to suggest that a 0.01 cm long, 10 K plasma cannot be diagnosed to better than $\delta T/T \approx 10$. In this regard it is fortunate that these plasmas expand significantly during Tdiag.

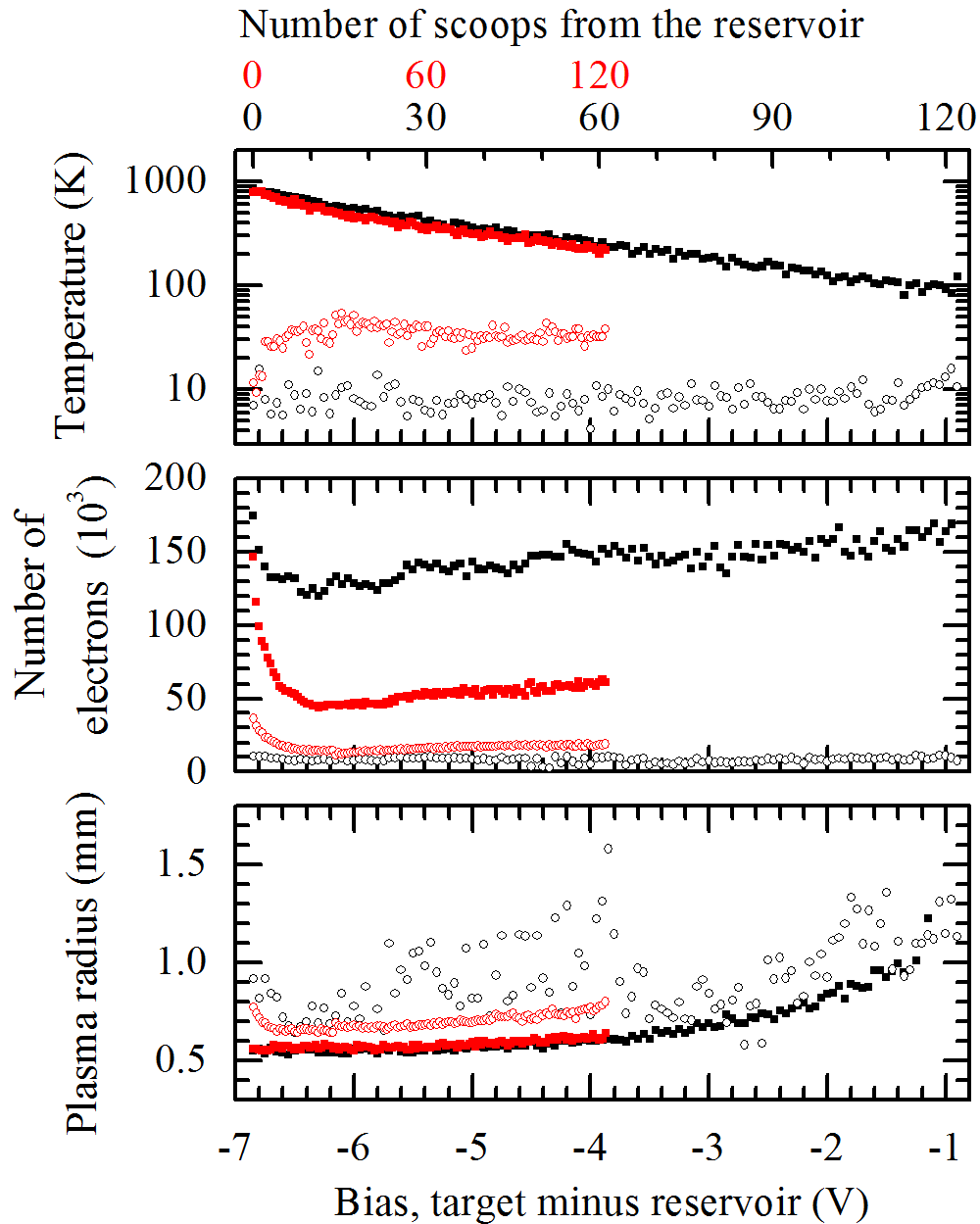


Figure 4.6: T , N , r_p measured for a sequence of 120 target plasmas scooped out of one cold reservoir. The sequence for the red (black) points increments the bias by 0.025 (0.050) V per scoop. Hollow points show the results of the same sequences with an added EVC step. By running shortened versions of these sequences where the reservoir temperature is taken after 10, 20, &c. scoops, it has been demonstrated that the reservoir has the same temperature as the target from start to finish. The images for $N = 10^4$ are dim, making the determination of r_p for those points difficult.

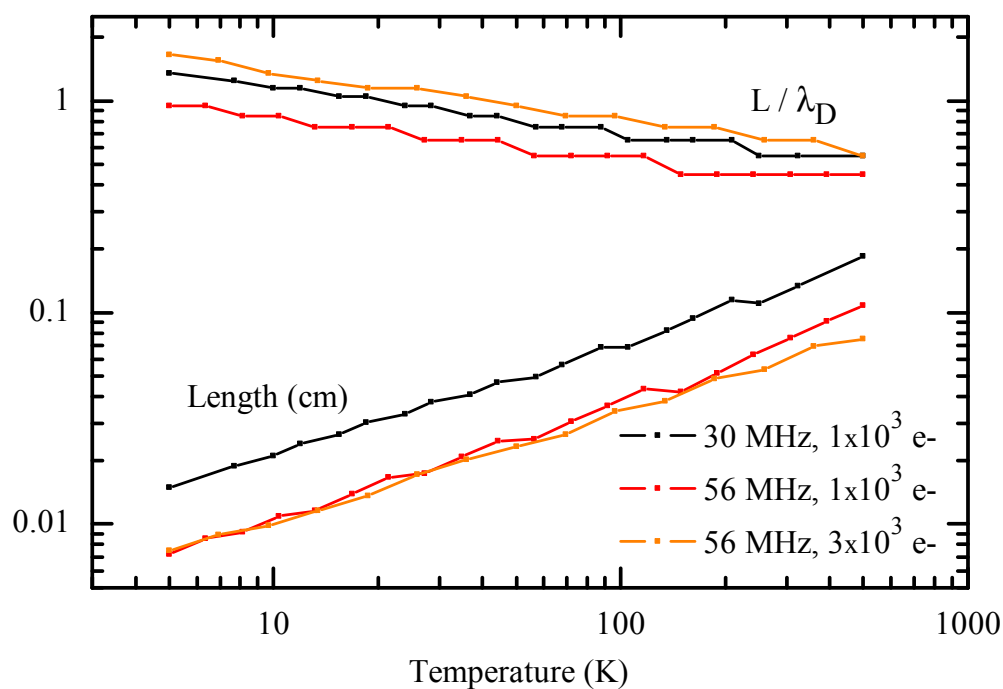


Figure 4.7: Target plasma L and λ_D found using the Poisson solver. N and $\omega_z/2\pi$ are given in the legend, and $r_p = 1$ mm. L vs. T has slope $m \approx 1/2$, or $L \propto \sqrt{T}$.

Chapter 5

Cavity cooling

Cryogenic plasma is unusual. In a quasi-neutral plasma (magnetic confinement fusion, semiconductor etching, arc welding, solar flares) “cold” rarely means less than 1 eV \approx 10,000 K. This is because the electron-ion radiative recombination cross section grows exponentially at low energy [10]. Sub-eV electrons are no sooner formed than they find a positive ion and recombine. The Penning Malmberg trap, on the other hand, usually contains only one charge species, the so-called one-component plasma. Such a plasma may theoretically come to equilibrium at arbitrarily low temperature [63].

The absence of neutralizing ions introduces a new problem for cooling via what plasma physicists call space charge Φ . The electrons all have the same sign, and this means they repel. If their separation increases they gain energy. A simplistic estimate of the resultant Joule heating is $H = VI/C$, where the heat capacity $C = (3/2)Nk_B$, the voltage $V \sim \Phi$, and the current $I \sim \tau_m^{-1}$, where τ_m is the time it takes for the plasma radius to increase by one e-folding. Electron-ion or electron-residual gas collisions will drive plasma expansion if the vacuum is not good. Electron-electron collisions do not directly cause expansion, but in the presence of a small misalignment (a tenth of a degree) between the electrodes’ symmetry axis and the magnetic field, these collisions lead to expansion via both single particle [19] and collective [66] resonant effects. Hence a perfect vacuum does not eliminate plasma expansion. A stronger magnetic field is often found to mitigate expansion ($\tau_m \sim B^2$ [64]), but even $\tau_m \sim 100$ s can lead to significant heating for $N > 10^6$ electrons [21].

Given that some amount of heating is inevitable, the plasma will not reach wall temperature T_w no matter how long one waits. This is easy to show using Newton’s law of cooling:

$$\frac{dT}{dt} = -\Gamma(T - T_w) + H \implies T_{min} = T_w + \frac{H}{\Gamma} \quad (5.1)$$

When $T = T_{min}$, $dT/dt = 0$: the cooling power no longer exceeds the heating power. Once H has been reduced as much as possible, the only way to get a colder plasma is to increase the cooling rate Γ . O’Neil studied this problem in 1980 [69].¹ He calculated that

¹At that time interest centered on the possibility of forming a pure electron crystal [63]. To avoid

Γ could be increased up to a thousandfold by coupling the plasma to a high- Q resonator or tuned circuit. The experiment at Berkeley is the first to implement O’Neil’s idea for plasma cooling. The cyclotron motion of plasma electrons drives an electromagnetic cavity mode, and the mode energy is dissipated via the currents it produces in the resistive cavity walls. A similar arrangement was used to control the emission rate of a single magnetized electron by Gabrielse and Dehmelt [41]. Later experiments by and Tan and Gabrielse seemed to suggest that the temperature of charge clouds containing a few thousand electrons was lower when B was tuned to the cyclotron-cavity resonance [86]. The central idea, that the spontaneous emission rate is higher when the radiating particle is tuned to resonance with a high- Q oscillator, is known more broadly as the Purcell Effect.

5.1 The Purcell Effect

When a charged object accelerates, it radiates² and this means some energy is used to excite a wave. The Purcell Effect is a prescription for making the charges radiate faster by making a certain kind of wave more excitable.

How “excitable” is a wave of a given frequency? In empty space all waves are possible, but there are more waves of short wavelength λ in a given volume than long. In three dimensions (3D), the number W of possible waves of wavelength $\lambda \geq \lambda_0$ which one can fit in a box of side L is $W = 2 \cdot \frac{1}{8} \frac{4}{3} \pi n^3 = L^3 \omega^3 / 3\pi^2 c^3$, where ω is the frequency corresponding to wavelength λ , c is the speed of light, and $n = 2L/\lambda_0$ (in 1D, $W = 2 \cdot n$). Taking $V = L^3$ one can then write $dW/d\omega = V\omega^2/\pi^2 c^3$. This means that in a 3D box, an oscillator which can radiate in some narrow range of frequency $d\omega$ sees far more waves to potentially excite if it is oscillating at high frequency. The spontaneous emission rate Γ is, naturally, proportional to the number of waves which may be excited. This is the origin of the B^2 scaling of the free-space cyclotron cooling rate $\Gamma_0 = 0.24 \text{ s}^{-1} \cdot B^2[\text{T}]$. It also explains why the cyclotron motion is what cools the plasma: the other plasma and single particle modes are at much lower frequency.

Purcell recognized that, since $\Gamma \propto dW/d\omega$, Γ may be increased if a way is found to increase $dW/d\omega$ [79]. This is just what one should expect from coupling the radiating particle to a high- Q oscillator (in his case a tuned circuit). In Purcell’s words, there is then ONE possible wave in the range given by the circuit’s bandwidth, or $dW/d\omega = 1/\Delta\omega$. For a well matched oscillator volume V , this number is always greater than the free-space number given above. The ratio is given by the Purcell enhancement factor $3Q\lambda^3/4\pi^2V$.

quantum-mechanical complications involving the largeness of $\hbar\omega_c/k_B T$ this would require very low magnetic field, where passive cyclotron cooling is completely ineffectual. This is where the Purcell Effect really shines, because it removes the ω_c^2 (or B^2) scaling to be described presently.

²Radiation from a possible neighboring charge could interfere destructively such that neither object radiates. There may be more peculiar exceptions, in particular the case of constant 1D acceleration [36], but these have not been demonstrated in an experiment.

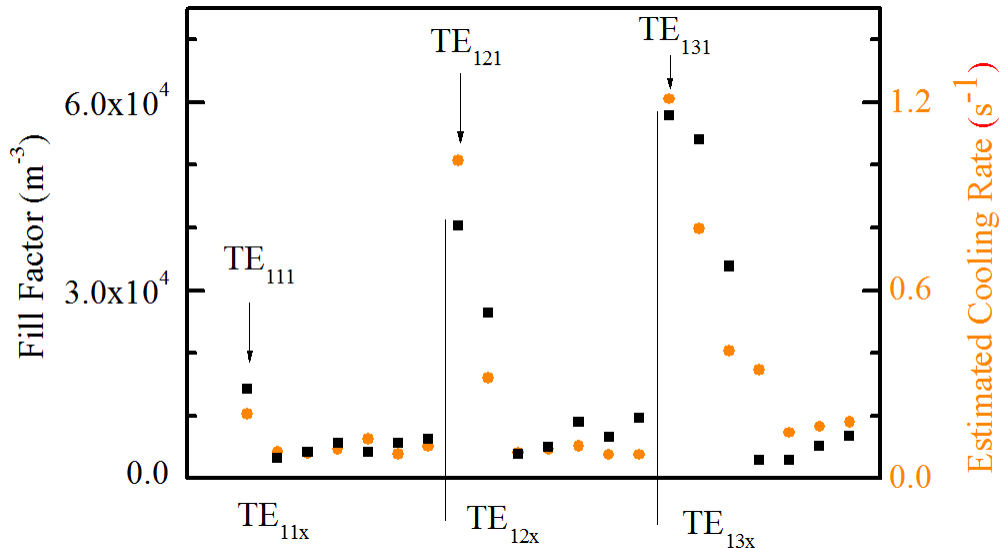


Figure 5.1: The fill factor (squares) and measured cooling rate (circles) for low order modes in Cavity 2. The fundamental is the best confined in each series (smaller mode volume), leading to a greater cooling enhancement. The cooling rate is estimated from the 7 s cooling data in Section 5.4, some of which is clearly saturated.

Purcell assumed the field strength was constant over V and zero elsewhere. A more careful treatment [31] replaces $1/V$ by $E_{\perp}^2 / \int E_{\perp}^2 dV$, where E_{\perp} is the transverse electric field, taken at the position of the radiating particle in the numerator. This spatial overlap or “fill factor” can be varied by changing the position of the plasma. The origin of the fill factor is apparent from the treatment given above. The fill factor arises naturally in an alternate derivation [80] using the fact that the radiated power $P = q\mathbf{v} \cdot \mathbf{E}$ may be Q times higher in a resonant cavity. This is because in a cavity, \mathbf{E} may accumulate to Q times its free-space value.

The treatment above implies that the fill factor $1/V$ should be large for good cooling. Surprisingly the opposite was observed in early experiments at Berkeley (Section 5.2). Later, it will be shown how one can recover at least qualitative agreement with the Purcell-based predictions provided the mixing is good (Section 5.3).

For the sake of clarity, Fig. 5.1 is given here as an example of data (from Section 5.4) which confirms the simple expected correlation between fill factors and cooling rates. The fill factors were calculated for Cavity 2 in COMSOL and cooling rate estimates were made using the data in Fig. 5.22.

5.2 Cooling in the Copper Cavity

The first attempt at cavity cooling was in the geometry shown in Fig. 5.2. The experimental sequence was

- i Scoop a small amount of plasma from the reservoir
- ii Move it into the cavity
- iii Let it cool for 2 s
- iv Measure its temperature
- v Change the magnetic field and repeat³

As described in Chapter 4, the reservoir technique was still empirical and amorphous at this time. Instead of using SDREVC, the operator used whatever the egun provided and simply kept scooping until something came out.⁴ The target plasmas came out hot. Since $T \sim \exp[-\Gamma t]$, one can approximate $\Gamma \approx (1/t)\ln[T_i/T_f]$ where T_i and T_f are the initial and final temperature of the target plasma after t seconds of cooling. Given that $T_f \geq 10$ K, starting at $T_i \sim 10,000$ K rather than, say, 100 K, increases the range of measurable Γ by a factor of five⁵.

Figure 5.3 is a broad scan of the four TE_{13x} modes⁶ accessible with the 40 A power supply. This data is actually quite remarkable because the cooling enhancement is relatively smaller in the conditions where the Purcell model indicates it should be strongest. The TE_{131} , which was engineered to be the highest Q mode, cools hardly at all, while the TE_{132} and TE_{133} cool best when the plasma center is at a field null ($E_{\perp} = 0$), where no interaction is expected.

This position dependence was further investigated with low N at the TE_{123} and with higher N at the TE_{134} (Fig. 5.4). Low- N plasmas cooled better where $1/V$ was larger, as expected (left panel). For higher N (right panel), a near-total suppression of enhanced cooling was observed when the plasma center was at a field maximum, while good cooling with an unexpected lineshape (bunny ears) was found when the plasma center was at a field minimum. The distance between the ears or “lineshape splitting” was found to be approximately twice the bounce frequency ω_z . Evidently the electrons were driving sidebands at $\omega_c \pm \omega_z$. These arise naturally when the plasma center is at a node, for electrons

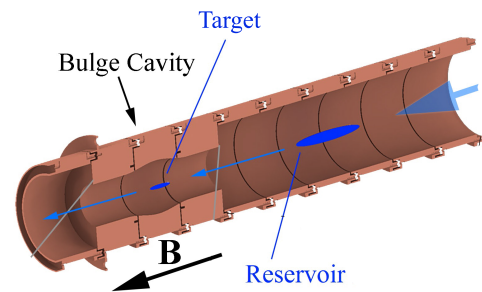


Figure 5.2: Section view of the first cavity experiment (eight more upstream electrodes not shown). The target plasmas were scooped out of the reservoir under the flat electrodes before being moved into the cavity. Similar to Fig. 1 in [77]

³Actually the magnetic field is ramped continuously. Each temperature point is assigned the average field value during the cooling time $t = 2$ s. Since $1/t \ll \Delta\omega_c$ this should not affect the result noticeably.

⁴For scanning cavity resonances (varying B), this method is probably preferable to one which relies on SDREVC, which can take days to tune at a given B .

⁵assuming $dT \propto T$

⁶The lower order modes did not cool as well. In retrospect, this seems to have been because the mixing $\Delta\omega_c \propto B$ when $\Delta\omega_c$ comes solely from inhomogeneity in the background field (more on this in the next section)

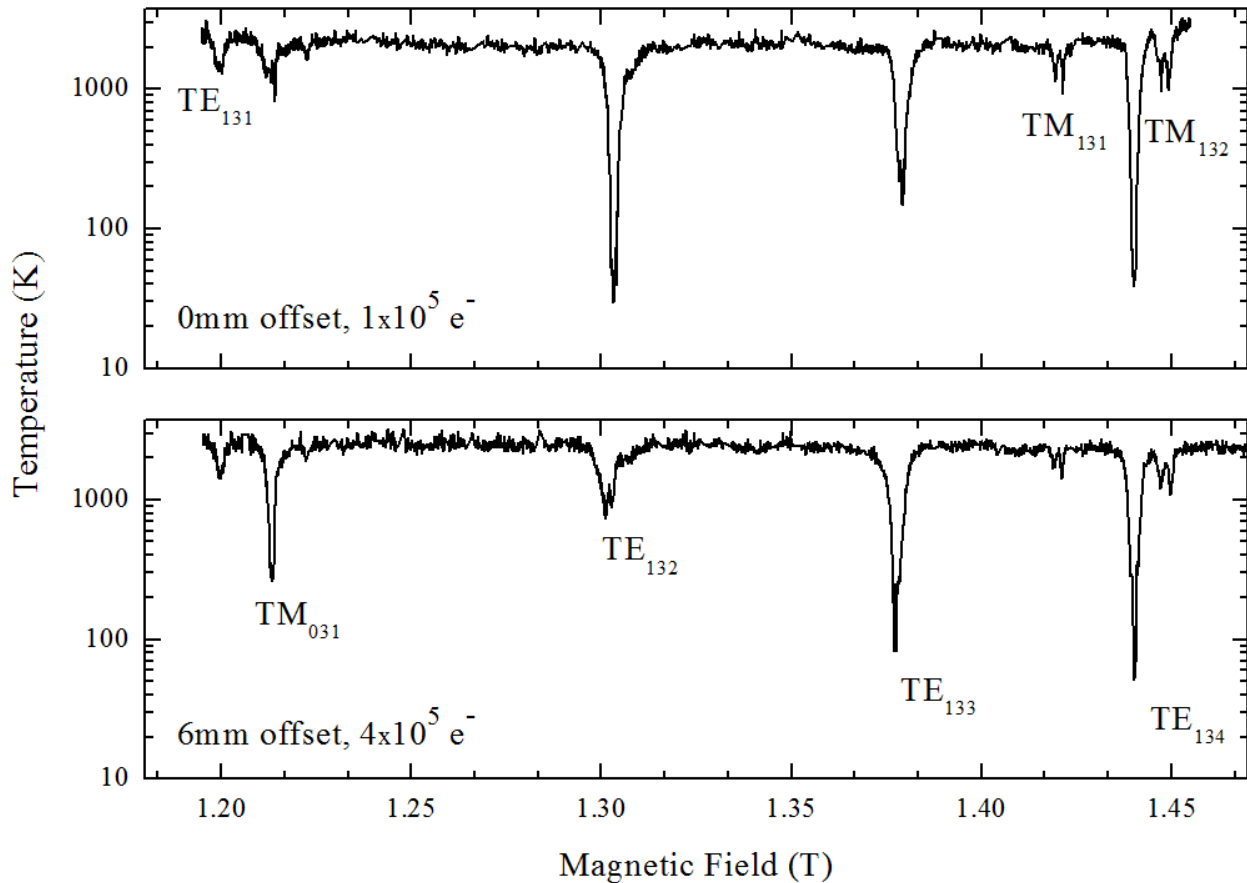


Figure 5.3: Temperature vs. magnetic field for target plasmas cooled two seconds in the copper bulge cavity. An apparently inverse relationship between plasma-cavity coupling and cooling rate is revealed by the systematically lower temperatures for plasmas displaced to a cavity node (0 mm offset for TE_{132} , 6 mm offset for TE_{133}) where coupling is expected to be weak. The targeted mode TE_{131} cools barely at all, indeed is outperformed by the neighboring TM_{031} which should couple very weakly (E_{\perp} vanishes on axis). Similar to Fig. 2 in [77].

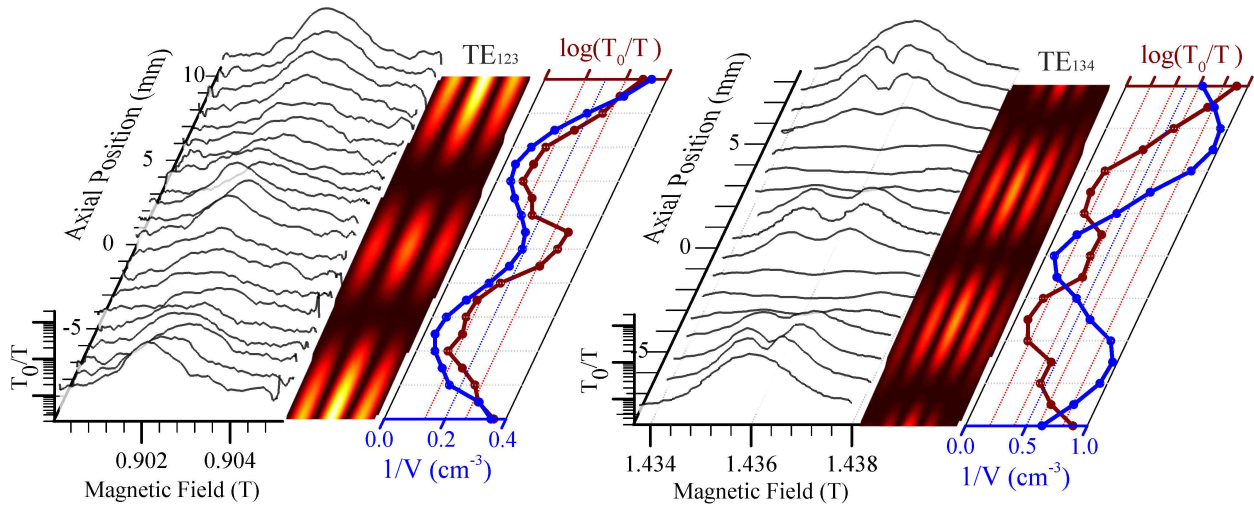


Figure 5.4: Plasma temperature for variable B and z , $N = \{10^4, 10^5\}$ electrons cooling at $\{TE_{123}, TE_{134}\}$. Temperature is plotted as $\ln(T_i/T_f) \propto \Gamma$. The red heat map indicates the axial dependence of the wave field E_{\perp} (extension in x is radial dependence). Cooling is worst where the field is strongest. The split peaks are separated by about 0.001 T or 30 MHz: twice the harmonic frequency ω_z of the confining potential. Similar to Fig. 3 in [77].

bouncing over a node see the microwave field modulated at ω_z (and harmonics). A similar thing happens when microwaves are injected from the outside to heat the plasma (see next chapter).

Evans showed that on a sideband the cooling rate goes like T [30]. At low T the bounce orbit is short, the range of E_{\perp} sampled is small, so there's not much power in the sideband. Perhaps this explains the disappearance of these sidebands as the plasma temperature falls (Fig. 5.5). Or perhaps the sidebands are merely converging as ω_z falls due to $\lambda_D \propto \sqrt{T}$ decreasing and flattening the well. The latter explanation is plausible, but other effects may also contribute (see Fig. 5.15 and discussion).

In general these early cooling results fell short of the expected $\mathcal{O}(Q)$ enhancement. Cavity resonance was only a noticeable improvement over free space cooling for plasmas with $N \sim 10^5$ or fewer electrons, and usually required an unusual arrangement, where plasma-cavity coupling was low because of low spatial overlap or because the plasma was talking on a sideband. Something was blocking the dominant radiation mechanism.

5.3 Theoretical Advances

The problems encountered above are easier to treat using the alternate theoretical description, invoking $P = q\mathbf{v} \cdot \mathbf{E}$. Evidently for P to be large E must be made as large as possible. Out of N normal modes of the plasma, exactly one motional pattern provides the required constructive interference to maximize E . This mode, called the “collective mode,”

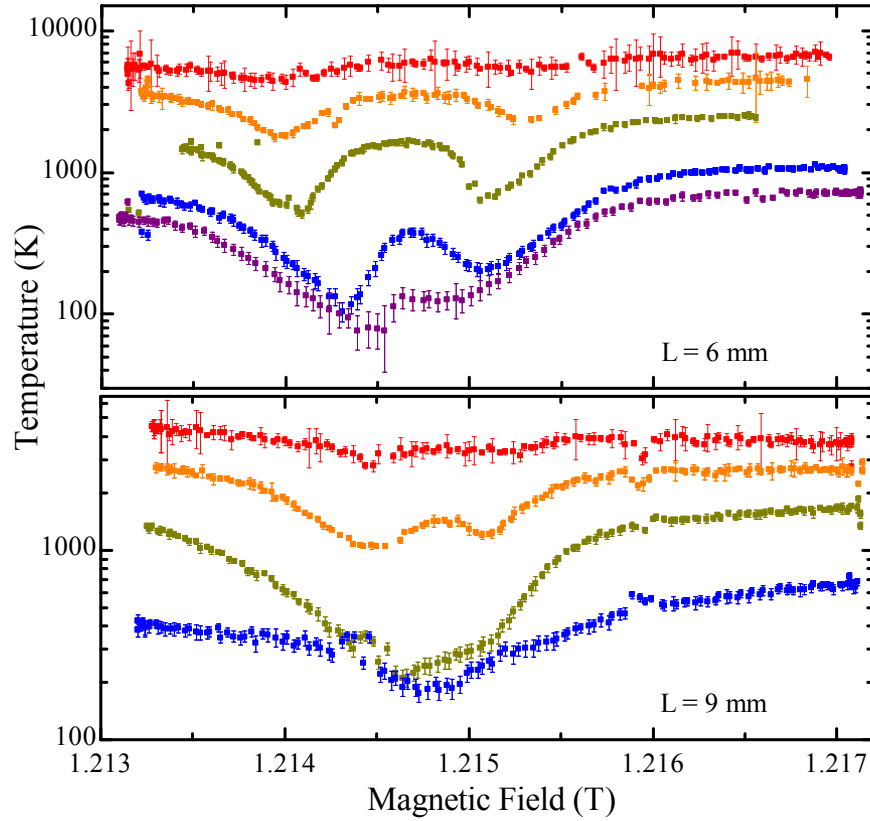


Figure 5.5: Plasma temperature for variable B and t , cooling at TM_{031} . Plasma center is offset 5 mm from cavity center. The colors correspond to 0.1, 0.5, 1.5, 4, and 6 s of cooling (red to purple). Plasma length L is indicated in each panel: the shorter plasma corresponds to a deeper well with a higher bounce frequency and more pronounced splitting. Similar to Fig. 4 in [77].

radiates at the Purcell enhanced rate. Meanwhile the remaining $N - 1$ modes, on the average, neither contribute to E nor benefit from its largeness ($\sum_{i=1}^N \mathbf{v}_i \cdot \mathbf{E}$ is by definition zero for all other modes). Since each mode contains on average $1/N$ of the total plasma kinetic energy, this means that for two electrons, half the energy can be removed this way and the other half is trapped in a weakly radiating mode. For ten electrons the situation is ten times worse. A 10^6 electron plasma swiftly loses 1 ppm of its energy and then stagnates.

In what at first seems to contradict this dismal (and correct) analysis, O’Neil predicted that under some circumstances the plasma should radiate all its energy at the full Purcell enhanced rate. Specifically he showed that the rate of energy loss from the plasma-cavity system

$$-\frac{d\langle H \rangle}{dt} = \frac{kT}{\pi} \int d\Omega \frac{2\nu_p \nu_\lambda}{(\Omega - \omega_\lambda)^2 + (\nu_p + \nu_\lambda)^2} \quad (5.2)$$

where $\Omega = \omega_c$ the cyclotron frequency, $\nu_p \approx N\Gamma_1$, the decay rate of the collective mode, $\nu_\lambda = \omega_\lambda/Q$ the linewidth of the cavity mode, and ω_λ is the cavity mode frequency. This integral has the form

$$\frac{xyz}{x^2 + y^2 + z^2} \quad (5.3)$$

which has a maximum when $x = y = z$ or $\Delta\omega_c \sim N\Gamma_1 \sim \omega_\lambda/Q$. This is called O'Neil's matching condition.⁷

A graphical model of the thermodynamic rate equations is provided in Fig. 5.6. The net energy transfer from plasma to walls cannot go faster than the slowest coupling rate. The matching condition is the result of maximizing these coupling rates and the single particle cooling rate

$$\Gamma_1 = \frac{2e^2}{m\epsilon_0 V} \frac{1}{(\omega_\lambda/Q)} \frac{1}{1 + (2\delta\omega_c/(\omega_\lambda/Q))^2} \quad (5.4)$$

at the same time. Here $\delta\omega_c \propto \Delta\omega_c$ is the particle's detuning from the cavity resonance (see below, particularly the discussion around Fig. 5.7). This expression is basically the Larmor cooling rate Γ_0 multiplied by the Purcell enhancement factor (Section 5.1), and is derived in Ref. [80].

It may be illustrative to derive the middle coupling term in the model just presented (the $\Delta\omega_c$ term will be discussed in the next section). Writing the center-of-mass displacement $r_{CM} = \epsilon \cdot r_L$, where r_L is the radius of the average cyclotron orbit,

$$\epsilon = \frac{1}{N} \left| \sum_{j=1}^N e^{i\varphi_j} \right| \approx \frac{1}{\sqrt{N}} \quad (5.5)$$

where φ_j is the cyclotron phase of the j^{th} electron relative to the collective phase $\langle \varphi \rangle = 0$. The approximate equality holds for a random flat distribution of φ , producing a random walk in the complex plane. The radiated power is proportional to the square of the total dipole moment: $P = (N\epsilon)^2 \cdot \Gamma_1 \cdot k_B T$. The energy U in the center-of-mass mode is $\frac{1}{2} m_{CM} (r_{CM} \omega_c)^2 = N\epsilon^2 \cdot k_B T$. Thus, for a plasma with N electrons the coupling (P/U) of the center-of-mass mode to the cavity mode is always $N\Gamma_1$, and it is only the fraction of energy in the collective mode, ϵ^2 , which changes.

This is at the root of the discrepancy between the results in Section 5.2 and the expected enhancement: the Purcell enhancement factor correctly describes energy loss from the collective mode, but one will only observe plasma cooling when the bulk electron energy is well coupled to this mode so that φ remains random and $\epsilon \sim 1/\sqrt{N}$ rather than falling to zero. The bulk-CM coupling will simply be called "mixing" in what follows. This term is used in a similar way in the description of stochastic cooling [90].

⁷O'Neil assigned only order of magnitude estimates to these variables. In Eq. 5.3 the resonant functions $y = \nu_p$ and $z = \nu_\lambda$ are approximated by constants over the range of integration and the variable $x = d\Omega \approx \Omega - \omega_\lambda \approx \Delta\omega_c$, the range of electron cyclotron frequencies due to electrons in the plasma seeing slightly different B fields.

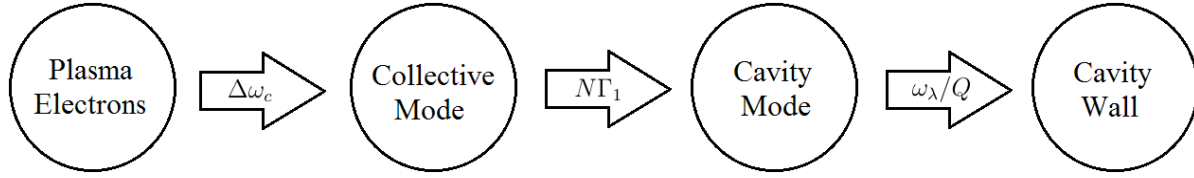


Figure 5.6: Graphical representation of the thermodynamic rate equations $dU/dt = -\kappa U$ where U is the energy of the source (bubbles) and κ is the coupling (arrows). This model is considered to be valid for weak coupling, i.e. when the dimensionless parameter $N\Gamma_1/(\omega/Q)$ is small. For clarity some additional details are not shown. Specifically (i) the arrows should point both ways, (ii) heat should be entering the plasma from expansion and electrode noise, (iii) the plasma (and in fact every bubble shown) may be weakly coupled to the egun, MCP, &c. via the free space radiation field.

Mixing

O’Neil’s answer to the problem that only the collective mode radiates is to steadily mix energy from the bulk back into the collective mode. There are several ways to do this. In the 1980 paper he assumed each electron had a slightly different ω_c because of a gradient in B . In this situation, the orbital angular coordinate of the j^{th} electron equals $\omega_{c,j}t + \varphi_j$. If the collective (in-phase) motion corresponds to an average phase $\langle\varphi\rangle = 0$ and an average frequency $\langle\omega_c\rangle$, then a random electron gyrating at $\langle\omega_c\rangle + \Delta\omega_c$ with phase φ_j will be back in phase with the collective mode in a time comparable to $\varphi_j/\Delta\omega_c$. Since for a typical electron $\varphi \sim 1$ radian, the collective mode should be repopulated⁸ at nearly $\Delta\omega_c$.

A second mechanism is thought to be responsible for most of the plasma cooling demonstrated in the last section. Electrons bounce back and forth in z , each with their own bounce frequency $\omega_z \sim 2\pi \cdot 10$ MHz. If the plasma length $L \sim \lambda$, the cavity mode wavelength, this bouncing takes electrons through alternating regions of strong and weak field. The field even changes sign if the plasma is centered at a wave node. To first order, an electron sees the microwave field modulated at ω_z . Electrons with different ω_z then see wave power at different $\omega_c \pm \omega_z$. This changes the observed T vs. B curve. In fact one will get a different T vs. B curve for every different initial temperature, because ω_z is a function of T (cf. Fig. 5.5). More importantly, the collective $\langle\varphi\rangle$ becomes a function of the electron positions,⁹ which vary in time as ω_z . The spread $\Delta\omega_z$ introduces a non-trivial time dependence to the collective phase $\langle\varphi\rangle$, possibly enabling a situation where $\varphi_j - \langle\varphi\rangle$ goes through zero at a rate comparable to $\Delta\omega_z$. This mixing mechanism should work best at the wave node where the depth of modulation approaches 100%. O’Neil assumed $L\omega_z \ll \lambda\Delta\omega_c$ so he did not model this effect.

⁸This does not mean that more than $\frac{1}{2}kT$ of energy accumulates in the collective mode, because the collective mode is itself dephasing— energy is going back into the plasma bulk— at about $\Delta\omega_c$. In other words $\Delta\omega_c^{-1}$ is the time it takes to randomize the cyclotron mode energy distribution after one of these modes (like the collective mode) is perturbed.

⁹The collective mode is no longer a true center of mass mode. Each electron’s contribution is weighted

In a way, the second mixing mechanism complements the first, for which $\Delta\omega_c$ is generated by a spatial gradient $\Delta B(z)$. The latter is suppressed by the electron bounce motion, which tends to average out $\Delta B(z)$ (see Intuitive Argument at the end of this section). As the plasma cools, the Debye length gets shorter, flattening the well and typically lowering ω_z . The gradient contribution improves while the bounce mixing, if there was any, disappears. These effects are evident in the data presented in the next section.

Collisions can also help to mix energy back into the collective mode. If an electron collides with an atom in the imperfect vacuum its cyclotron motion will be interrupted and φ will change. This mechanism directly mixes energy back into the collective mode. It may have contributed to the cooling behavior in 2015, but the vacuum in the 2017 trap (next section) is over an order of magnitude better. Even if the “good mixing” up to $N \sim 10^4$ obtained in the original trap was entirely due to this effect (rather than a $\Delta\omega_c$ arising from inhomogeneity in the solenoidal field), the effect remains irrelevant for $N > 10^3$ in the experimental conditions achieved in 2017.

Self collisions may significantly influence mixing in certain special cases. If, as O’Neil assumed, the collective mode is a true center of mass mode, then electron-electron collisions cannot directly contribute to mixing (Newton’s third law). However, if E_\perp varies across the plasma, the collective mode is not a center-of-mass mode, and collisions can contribute indirectly to the “second mixing mechanism” described above. Regardless of the nature of the collective mode, self collisions may contribute indirectly by reducing the effective bounce rate, which (as argued below) must reduce the effective spread in cyclotron frequencies. These effects should be most significant for the densest plasmas, and may explain why the mixing rate appears to be much higher for high- N in some of the data in Section 5.4.

Broadly speaking, three mixing mechanisms have been identified above, with rates proportional to $\{\Delta\omega_c, \Delta\omega_z, \nu\}$. A systematic attempt to independently control and study these three rates has not been attempted. There are several additional variables (N, L, T, r_p, ω_z) which also affect cooling and which would inevitably be varied at the same time. Instead, in Section 5.4, data is presented for a roughly corresponding set of variables: coil current ($\Delta\omega_c$), well shape and temperature ($\Delta\omega_z$), and number of electrons (ν). These variables are nearly independent and relatively easy to control, although their effects on the mixing rates are somewhat interdependent.

The reader may be wondering, why not just make $\Delta\omega_c$ as large as possible? Because in frequency space $\Delta\omega_c$ is a measure of how far the average electron is from resonance with the cavity (recall Eq. 5.4). The competing effects lead to an optimum near $\Delta\omega_c = \omega_\lambda/Q$. The cavity mode linewidth ω_λ/Q therefore sets an approximate upper bound on $\Delta\omega_c$ (see Fig. 5.7).

by the (signed) microwave electric field at its instantaneous location.

In connection with the possible bounce suppression mechanism discussed below, this raises another concern: for non-negligible ω_z , the effective $\Delta\omega_c$ for the purpose of mixing is less than the actual average detuning, which is what limits the single particle cooling rate in Eq. 5.4. In this case one must reduce ω_z or else fall unavoidably short of O’Neil’s maximum. Fortunately, a cold plasma naturally reduces ω_z . This produces a surprising trend in the cooling rate as a function of T (see Section 5.4).

Superradiance

The collective mode couples more strongly to the cavity when there are more particles participating in the collective motion. Ten electrons moving synchronously each radiate ten times faster than they would independently. In other words, the total power emitted by ten coherent electrons is one hundred times greater than that of a single electron. This remarkable effect, known as superradiance, was apparently a surprise to the atomic physics community in 1954,¹⁰ despite being an immediate consequence of Maxwell’s Equations. This is partly because it is so difficult to keep energy in the collective mode. The energy fraction ϵ^2 is usually quite small, only approaching $1/N$ when the mixing is very good.

Theorists have found two dimensionless parameters to describe the two critical arrows in Fig. 5.6. Goodness of mixing (first arrow) is parametrized by the combination $\Delta\omega_c/N\Gamma_1$. The strength of plasma-cavity coupling is parametrized by the combination $N\Gamma_1/(\omega_\lambda/Q)$. When the latter parameter is of order unity, the collective mode is strongly coupled to the cavity mode and the two modes are expected to hybridize (see Fig. 5.8). This behavior has not been investigated experimentally. A possible test is proposed at the end of the chapter (Section 5.5).

One may summarize the theory work in two roughly equivalent statements.

Hypothesis 1 (O’Neil): *The maximum amount of power is radiated when the plasma and cavity impedance are matched to the CM dephasing rate ($\nu_p \sim \omega_\lambda/Q \sim \Delta\omega_c$).*

¹⁰Dicke discovered it while writing down equations to describe emission from a quantum gas [25]. Laser amplification works the same way; there, the unusual situation where the collective mode (an excited state) has a significant amount of energy in it is called “population inversion” and is achieved via optical pumping of a metastable state.

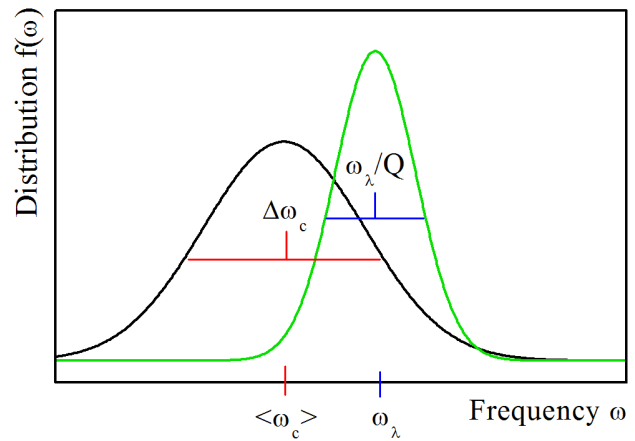


Figure 5.7: Plasma-cavity overlap in the frequency domain. Maximal power transfer is expected for maximum overlap ($\langle\omega_c\rangle = \omega_\lambda$, and similar linewidths). Here there are many electrons outside the resonance (ΔB too high) and the centers are offset as in a T vs. B scan.

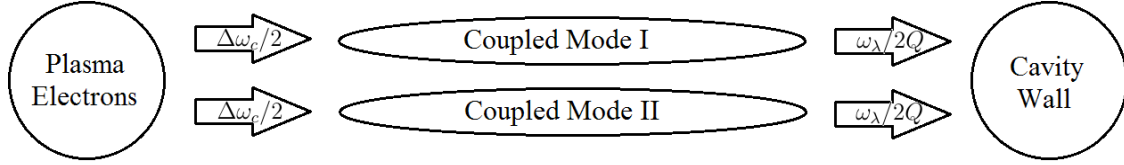


Figure 5.8: Mode splitting believed to occur when the superradiant power load exceeds the cavity dissipation or, in symbols, $N\Gamma_1 > \omega_\lambda/Q$.

This is O’Neil’s prediction. For a cavity mode with $Q = 10^3$ and $1/V = 10^6$, the maximum occurs at $N = 5 \cdot 10^6$ and $\Gamma = 36 \text{ s}^{-1}$ and requires a spread in cyclotron frequencies $\Delta\omega_c = 2\pi \cdot 25 \text{ MHz}$.

Hypothesis 2 (Robicheaux et al.): *Provided that the mixing is good ($\Delta\omega_c/N\Gamma_1 \sim 1$) the plasma will cool at the single particle rate Γ_1 for all N less than the overload value ($N\Gamma_1/(\omega_\lambda/Q) \sim 1$).*

This is the Berkeley-Purdue interpretation, to which is added the basic thermodynamic prediction that for $N\Gamma_1 > \omega_\lambda/Q$ the cooling rate Γ must fall as $1/N$ [76]. Notice that O’Neil’s $\nu_p = \beta^2 f(\Omega) \approx \pi e^2 N/4\epsilon_0 m V \Delta\omega_c = (8/\pi) \cdot N\Gamma_1$ when the matching condition is fulfilled, so the two Hypotheses are compatible. Both Hypotheses assume that the mixing is not suppressed by the bounce motion, an effect which is treated briefly in the following subsection.

Intuitive Argument for Suppression of the Mixing Due to Bounce Motion

O’Neil’s argument assumed electrons stationary in the axial magnetic field gradient. If the electrons can sample all values of the gradient, the cyclotron frequencies will tend to average to nearly the same value. A proper model of mixing in the presence of both axial bounce motion ω_z and a gradient $\Delta\omega_c$ ought to include a suppression factor proportional to the ratio $\Delta\omega_c/\omega_z$. Here a simplistic derivation is given to suggest how such a factor may come about.

For the j^{th} electron cyclotron phase $\varphi_j(t)$ and its difference with the center of mass phase $\langle\varphi\rangle$ it is evident that

$$\begin{aligned}
 \varphi_j(t) &= \int dt \omega_c + \varphi_{j,o} \\
 &= \langle\omega_c\rangle t + \int dt \delta\omega_{c,j}(z) + \varphi_{j,o} & \varphi_j(t) - \langle\varphi(t)\rangle &= \frac{e}{m} \frac{dB}{dz} \int dt \frac{L}{2} \cos(\omega_{z,j}t) + \varphi_{j,o} \\
 &= \langle\varphi(t)\rangle + \int dt \frac{e}{m} \frac{dB}{dz} z(t) + \varphi_{j,o} & &= \frac{\Delta\omega_c}{2\omega_{z,j}} \sin \omega_{z,j}t + \varphi_{j,o}
 \end{aligned}$$

The phase difference $\varphi_j(t) - \langle \varphi(t) \rangle$ must be small in order for an electron to contribute to the collective mode. If $\Delta\omega_c/2\omega_{z,j} < \pi$ radians, an electron pushed 180° out of phase ($\varphi_{j,o} = \pi$) with the collective mode will never¹¹ return ($\varphi_j(t) \neq 0$ for all t). This happens eventually to every electron because the decay of the center of mass mode tends to increase $\varphi_{j,o}$. After their initial contribution to the collective radiation, electrons with $\Delta\omega_c/2\omega_{z,j} \ll 1$ remain permanently out of phase in spite of the magnetic field gradient.

This demonstration is only intended as motivation for a proper theory. It is not known whether similar expressions can bridge the gap between the Berkeley-Purdue theory and some of the data presented in the next section.

5.4 Cooling in the Titanium Cavities

The first titanium cavity is geometrically the same as the original copper bulge, except cut into nine segments instead of three. This permits a z -position scan like that in Fig. 5.4 but with a shorter plasma and a longer range of axial positions in the cavity ($L = 7\text{--}20$ mm over ± 8 mm $\rightarrow L = 4\text{--}6$ mm over ± 30 mm). Figure 5.4 traces the full lineshape $\Gamma_i(B)$ for each axial position z_i . Figure 5.9 reports the maximum $\Gamma_{i,\max}$ for 22 values of z_i . For each position, $N = 2 \cdot 10^6$ electrons are allowed to cool for 0 and 1 s before their temperature is measured. The ratio $T_{0\text{ s}}/T_{1\text{ s}}$ is used to estimate the cooling rate via $\Gamma \approx \frac{1}{t} \ln[T_i/T_f]$. The scan is repeated with a significant applied gradient $\Delta\omega_c \approx 2\pi \cdot 20$ MHz. This single figure demonstrates several of the mixing effects described in the last section. With no magnetic field gradient, the cooling enhancement is completely blocked at the antinodes ($z = \pm 7.5$ mm) and is best at the node ($z = 0$ mm) where the gradient in microwave power is steepest. Applying a strong magnetic field gradient restores Purcell-like behavior: cooling is better where the field is strong. Curiously, the best cooling is obtained at neither node nor antinode: notice the horns at $z = \pm 12.5$ mm. One possibility is that the plasma is benefiting from at least two mixing mechanisms ($\Delta\omega_c$ and $\Delta\omega_z$). The combined effect appears to be slightly nonlinear, perhaps due to the approximation coming from two temperature points $T_{0\text{ s}}$ and $T_{1\text{ s}}$ (Fig. 5.15 shows how such an approximation could amplify a small increase in Γ).

For the analysis in the rest of this section it is important to be certain of the plasma temperature. Extra steps have been taken in what follows to implement some of the corrections prescribed in Chapter 3. Basically,¹² for each plasma

1. The plasma solver (see Appendix C) provides the 3D plasma profile in the cooling well, from which the initial plasma length L_i is extracted

¹¹In the real world, electron-electron collisions can reset the electron's *bounce* phase or even trap it at one value of the detuning $\delta\omega_c(z)$. In other words, anything that makes $z(t) \neq \frac{L}{2} \cos(\omega_z t)$ can circumvent the outcome in the right column above. These effects should be stronger at lower temperature, where the collision rate is higher. On the other hand, a spread $\Delta\omega_z$ for different electrons is probably not sufficient in the case that the collective mode is pure center of mass, for $\int dt \frac{L}{2} \cos \omega_z t$ will still average to zero over many bounce cycles, and the analysis given in the text should hold.

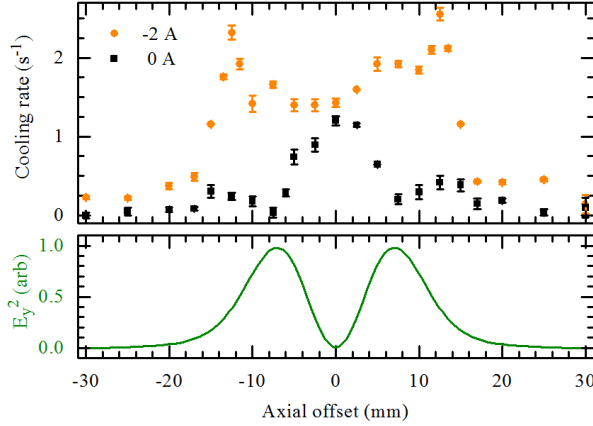


Figure 5.9: Cooling at TE_{122} ($B = 0.85$ T) as a function of position and gradient. The black dots come from measurements with no applied gradient, the orange with -2 A in the gradient coil. The bottom panel shows an HFSS simulation (done by Nathan Evetts at UBC) of the on-axis microwave power which can couple to the cyclotron motion.

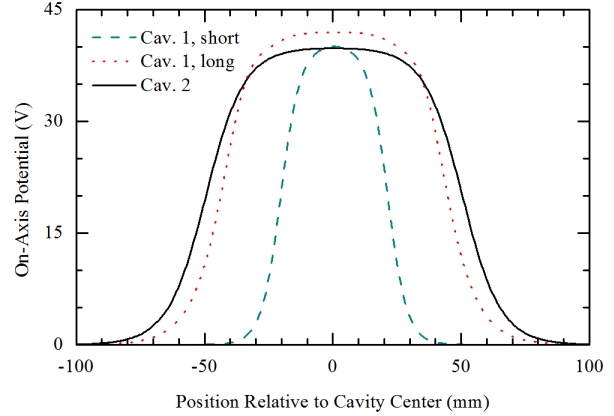


Figure 5.10: Three well shapes used in the majority of the experiments in this section. The well in Cavity 2 is actually formed with the biases $\{-90, -50, -90\}$ V on electrode lengths $\{3, 4, 3\} \cdot 2.54$ cm

2. The measured excitation voltages during the dump ramp $\{\phi_{exc}(t)\}$ are converted to on-axis well depth $\phi_w(t)$. The t -offset between SiPM trace and $\phi_w(t)$ is adjusted such that the disappearance of plasma current coincides with the time t_f where $\phi_w(t_f) = 0$
3. A modified form of the Tdiag software uses ϕ_w and records its value at $t = t_{esc}$, the time when the first e-folding of electrons escapes
4. The final length L_f is computed as the distance between turning points for particles at the top of the well when $t = t_{esc}$
5. The temperatures obtained in (3) are corrected by the factor $(L_f/L_i)^{2/3}$

Figure 5.10 displays the on-axis potential profile for the three wellshapes used in most of this section. These are the “cooling wells” mentioned in step (1) above.

The next set of graphs, Fig. 5.11, record the full temperature evolution at the TE_{111} in Cavity 1 ($B = 0.29$ T). Two well shapes are tested. One is short ($\omega_z \approx 2\pi \cdot 12$ MHz) and one is long ($\omega_z \approx 2\pi \cdot 2$ MHz). The dataset includes as variables the number of electrons $N = 3 \cdot \{10^4, 10^5, 10^6, 10^7\}$ and the current in the gradient coil $I = \{0.1, 0.28, 0.9, 1.87\}$ A, which corresponds to $(e/m) dB/dz = 2\pi \cdot \{1.5, 4, 14, 28\}$ MHz cm^{-1} at the center of Cavity

¹²Actually L_i and L_f are interpolated using look-up tables which are generated for the full range of $\{N, T\}$ for step (1) and t_{esc} for step (4). The excitation-well depth conversion also only needs to be done once.

1. The plasmas are initialized at a high temperature by applying a pulse of broadband noise with 10 – 100 mV amplitude (1 – 100 μ W power) for a fraction of a second¹³ prior to $t = 0$ in the figure.

Fitting each data set to the model function $T = (T_i - T_f)\exp[-\Gamma t] + T_f$, one obtains the cooling rate Γ in eight configurations for each N . For each configuration one can estimate the total spread in cyclotron frequencies $\Delta\omega_c \approx (e/m)dB/dz \cdot L$ where L is the plasma length. One then obtains eight points on the curve of Γ vs. $\Delta\omega_c$ for each N (Fig. 5.12).

The goal of this study was to compare the shape of the resulting Γ vs. $\Delta\omega_c$ curves with results from a scale-independent numerical simulation [80]. That is why such a broad swath was cut in parameter space. As it turns out, only for the highest N studied does one obtain what looks like a simple relationship. For $N = 30 \cdot 10^6$ the plasma is completely flattening both wells for all temperatures studied ($L > 100 \cdot \lambda_D$) and the plasma is highly collisional (Spitzer self-collision time $t_c \sim 1 \mu s$ [85]). These two factors may well eliminate the bounce suppression discussed at the end of the last section. The resulting simpler case (a spread of cyclotron frequencies with no bounce suppression) is what Robicieux et al. have simulated [80]. A direct comparison with theory is feasible for this case.

That comparison is plotted in Fig. 5.13. The data points from the bottom right panel of Fig. 5.12 are now given with the x axis replaced by the dimensionless parameter $\Delta\omega_c/N\Gamma_1$, mentioned in the last section. The theory curves represent the average rate of energy loss divided by total energy for a simulated ensemble of electrons. Each electron is locked to a particular z -position in the plasma. Each electron therefore sees a cavity field intensity $E_{\perp,j}$ and has a cyclotron frequency $\omega_{c,j}$ corresponding to its (static) axial position z_j .

The theory takes three adjustable parameters.

- i The fill factor $1/V_{eff} = 1.0 \cdot 10^5 \text{ m}^{-3}$, is a simulation result from Evetts using HFSS.¹⁴
- ii The cavity linewidth ω_λ/Q is obtained from Fig. 5.24: the logarithm $\ln(T_0/T)$ of the 12 MHz T vs. B set is fit very well by a Gaussian of width $2\sigma = 23$ MHz.
- iii The plasma length $L = \{36, 63\}$ mm. These are the average values for plasma in the short and long wells, respectively. The length determines the range of $E_{\perp,j}$ and $\Delta\omega_{c,j}$. The fill factor is modified for each electron by $(E_{\perp,j}/E_{\perp,max})^2$, where $E_{\perp,max}$ is the field at cavity center.

These parameters also determine Γ_1 for the x -axis scaling of the data points.

Considering that no attempt was made to tune any of these parameters to improve the fit, the agreement between experiment and theory is encouraging. Four data points per plasma length is not enough to determine whether the experimental points lie on a single curve or whether the 63 mm simulation has more in common with the long well points (open squares)

¹³10 – 1000 ms. The pulse is longer and of lower intensity for smaller N because these plasmas take longer to rethermalize after the excitation (see Chapter 7).

¹⁴The original, one-cavity simulation result $1/V_{eff} = 2.0 \cdot 10^5 \text{ m}^{-3}$ is here divided by 2 because this mode is now shared between Cavity 1 and Cavity 3

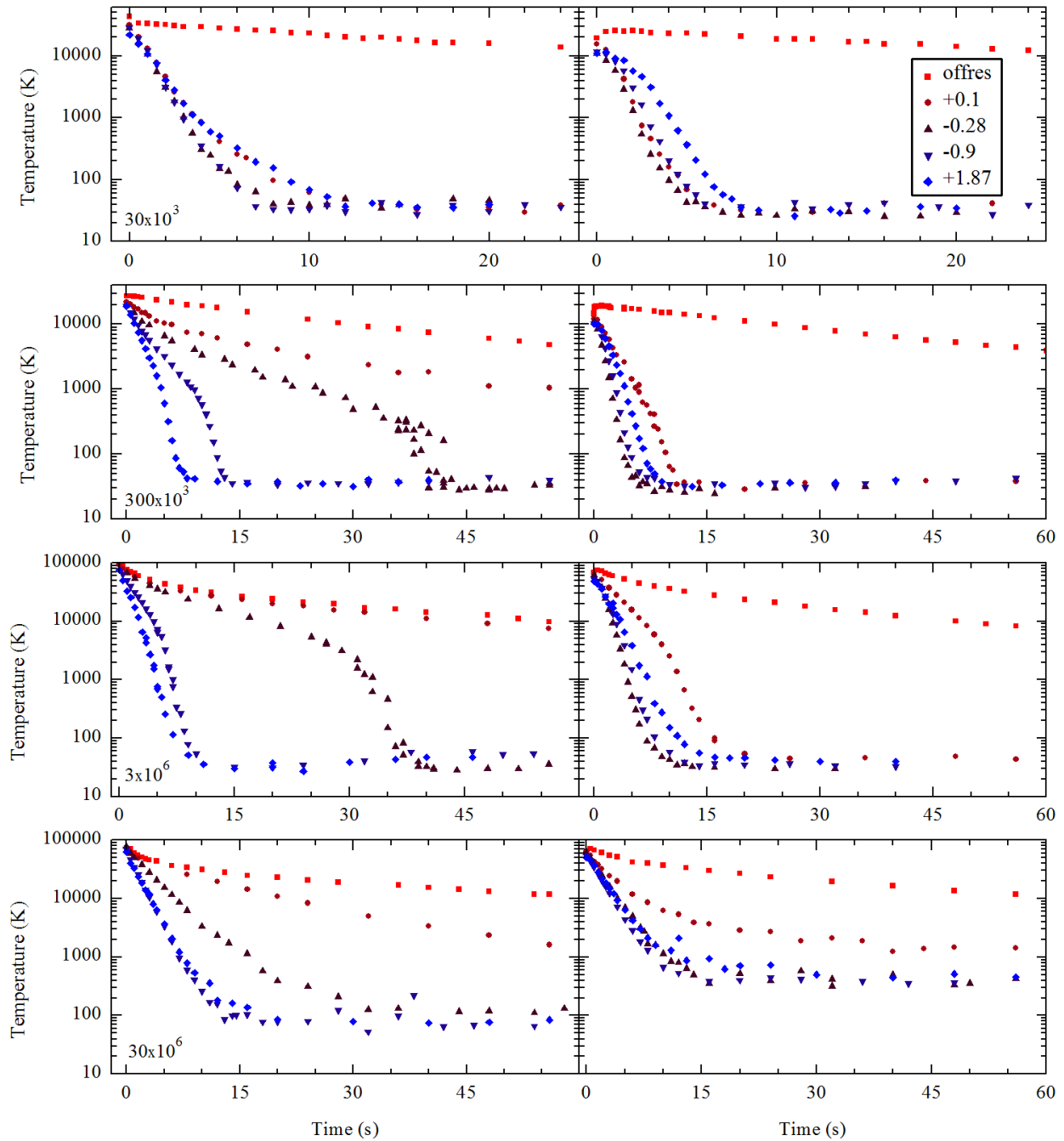


Figure 5.11: Temperature vs. time at TE_{111} as a function of number, well shape, and magnetic field gradient. Gradient coil current is given in the legend. N is indicated for each row in the bottom left of the first panel. Left column is a short well, right is a long well. Plasma center is the cavity center for both wells.

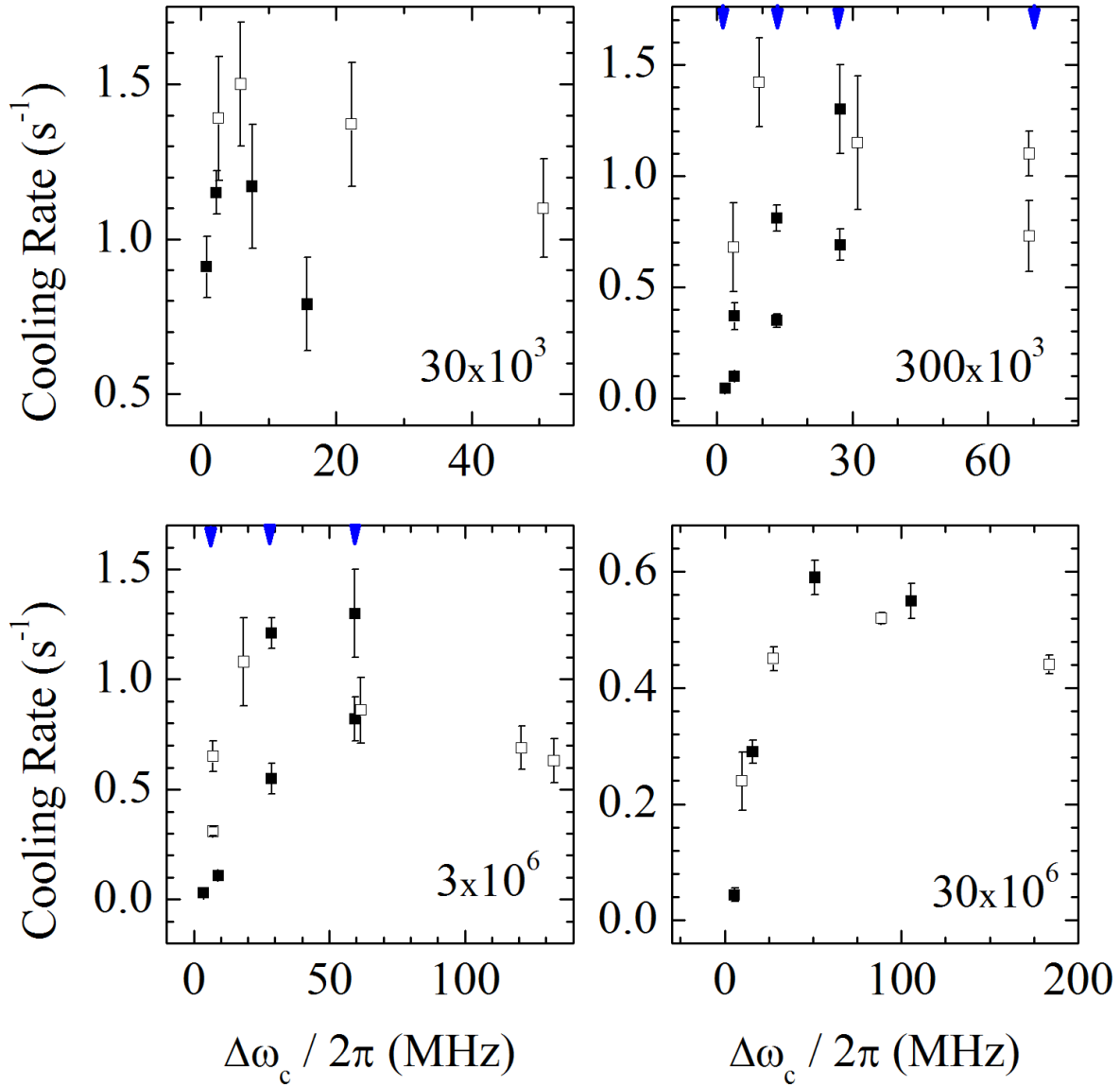


Figure 5.12: Cooling rate vs. spread in cyclotron frequencies for $N = 3 \cdot \{10^4, 10^5, 10^6, 10^7\}$ in a short well (dark squares) and a long well (open squares). Number of electrons is indicated in the top left of each panel. Double-valued $\Delta\omega_c$ locations (indicated with blue arrows from the top) correspond to plasmas with distinct hot and cold cooling rates, as discussed in the text.

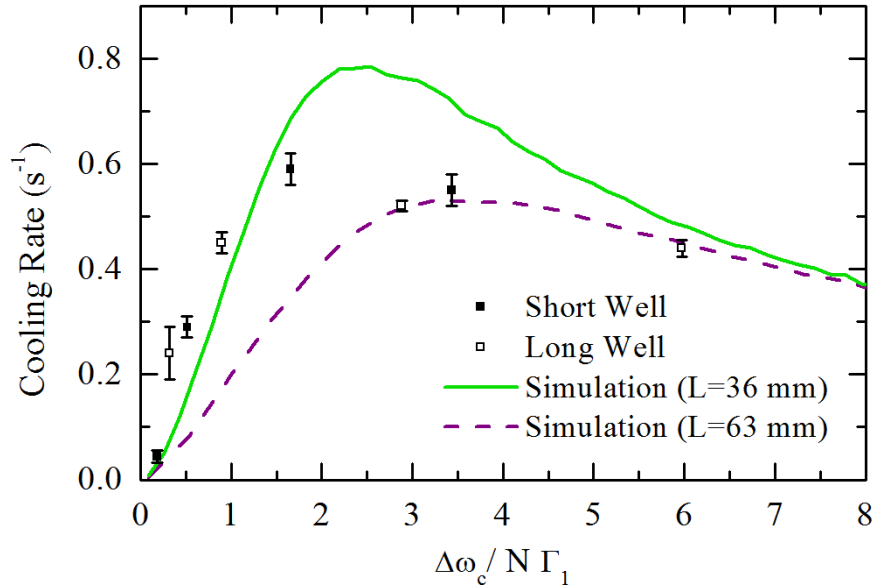


Figure 5.13: Cooling rates for $30 \cdot 10^6$ electrons compared to theory predictions. The theory curves were obtained via numerical simulation by Eugene Kur for a short and long plasma, as given in the legend. The predictions depend sensitively on the cavity linewidth and mode volume, which have been given exactly their nominal values. For no value of $\Delta\omega_c/N\Gamma_1$ should one expect to achieve the optimal cooling rate $\Gamma_1 \approx 4 \text{ s}^{-1}$ because to do so requires optimizing N as well; N is about a factor of 10 too high in this case.

than the short well points (filled squares). Nevertheless, the theory correctly predicts the peak cooling rate and optimal spread in cyclotron frequencies to within about 25%.

The fixed- z_j theory used above does not seem to accommodate the data sets with lower N ($N = 30 \cdot 10^3, 300 \cdot 10^3, 3 \cdot 10^6$ electrons). The calculated values of $\Delta\omega_c/N\Gamma_1$ come out unreasonably high. This suggests that mixing is being suppressed for these plasmas. Lower N implies lower plasma density, thus less Debye shielding of the trapping potential, thus a higher bounce frequency. Perhaps, then, the apparent reduction in the mixing rate for lower N is the factor of $\Delta\omega_c/\omega_z$ bounce suppression discussed earlier: the axial bounce motion reduces the effective spread in cyclotron frequencies because all electrons see roughly the same range of magnetic field within a decay time. Indeed, the $3 \cdot 10^6$ data set falls neatly onto a single curve if one rescales the horizontal axis by $\Delta\omega_c/\omega_z$. This operation is hard to justify, though, since the effective bounce rate ω'_z varies with T (see below).

The presence of many complicated factors in this situation makes it hard to evaluate or even to write down an accurate model. For example, it is reasonable to expect that collisions, which tend to lock electrons in place so that $\Delta\omega_c$ is not reduced by averaging, would mitigate the proposed bounce suppression. Whatever form of the collision rate is chosen, it will vary strongly with temperature, as may the well shape and effective bounce frequency. Another complication affecting this particular data set is that the TE_{111} is not an isolated peak, so

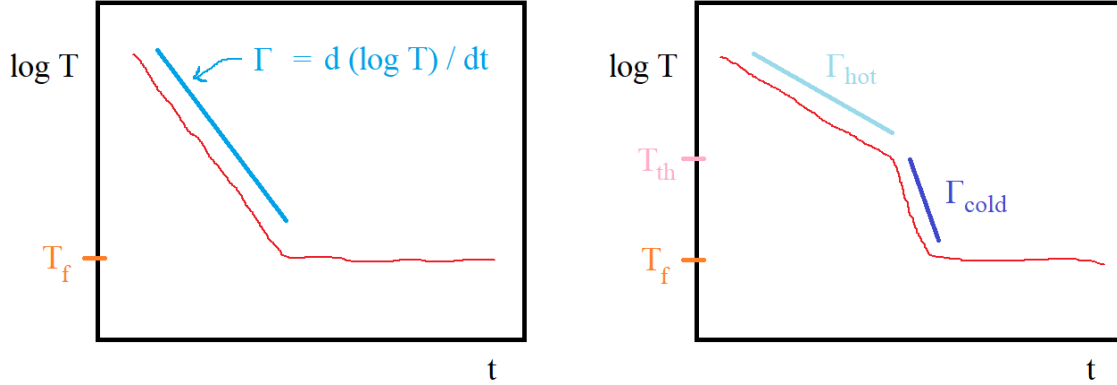


Figure 5.14: Illustration of the temperature threshold observed when cooling is apparently suppressed by bounce motion. The left panel is what one normally sees. The right panel represents a plasma which starts cooling much faster once it gets below some threshold $T = T_{th}$, as is the case for the plasmas in Fig. 5.15

large values of $\Delta\omega_c$ do not put electrons off resonance, but rather into a different resonance (see Fig. 5.24). Incidentally, this effect could explain why the point or two on the right of Fig. 5.13 are slightly higher than the single-resonance prediction.

A complete theoretical description should also explain the appearance of two time scales in some of the T vs. t curves. Normally the value of Γ is easy to determine: it's the slope of the linear range before T settles to T_f (see Fig. 5.14). However some of the plasmas studied are not so simple. The cooling seems to proceed at the rate Γ_{hot} until some threshold $T < T_{th}$, after which the rate is $\Gamma_{cold} \gg \Gamma_{hot}$. This is most apparent in the short-well plasmas of intermediate density. In a longer well or for a steeper ∇B there is just one slope $\Gamma \approx \Gamma_{cold}$. This observation alone is not sufficient to tell whether the suppression ($\Delta\omega_c/\omega_z$) is responsible for the smaller enhancement at higher T (and higher ω_z), or if it is merely a result of the smaller spread in frequencies ($(e/m)\nabla B \cdot L \approx \Delta\omega_c$) for smaller L .

To strengthen the connection with ω_z more T vs. t curves are accumulated for $N = 3 \cdot 10^5$, $I = -0.90$ A in five different wells (Fig. 5.15). The wells have a vacuum bounce frequency $\omega_z = 2\pi \cdot \{9.3, 11.8, 14.3, 16.8, 18.3\}$ MHz.

The dependence of T_{th} on ω_z is not very strong, and it requires very good cycle-to-cycle reproducibility to get matching T 's over the 30 s timescale. These factors make it hard to see the trend in T_{th} , but there is one ($2\pi dT_{th}/d\omega_z = -30 \pm 2$ K/MHz). The deeper wells (higher ω_z) require a lower T to get to Γ_{cold} , which is consistent with the near absence of this threshold phenomenon in the long well side of Fig. 5.11.

For these plasmas, $L \approx 6$ mm and $\lambda_D < 1$ mm, so the vacuum potential is partially shielded. Electrons are effectively bouncing at the lower rate $\omega'_z < \omega_z$ because the plasma is flattening the well. Numerical integration is used to calculate an average bounce time $2\pi/\omega'_z$ for a single electron of energy $E \approx \frac{1}{2}k_B T$ in each well.

At $T = T_{th}$, the plasma lengths (4–8 mm) and Debye lengths (0.3–0.6 mm) for the five

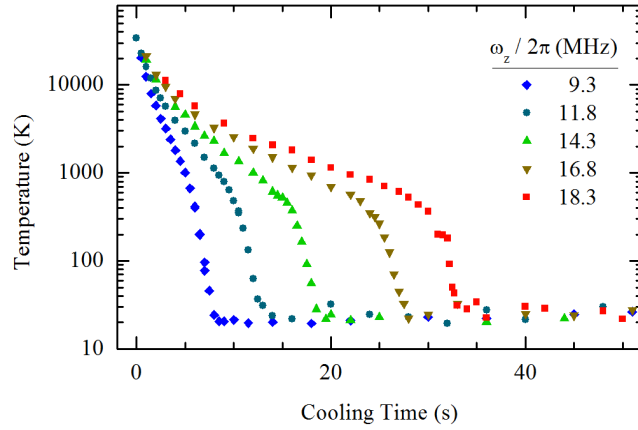


Figure 5.15: Motion of the knee in T vs. t for five different wellshapes. Plasma seems to cool at two distinct rates for reasons unknown.

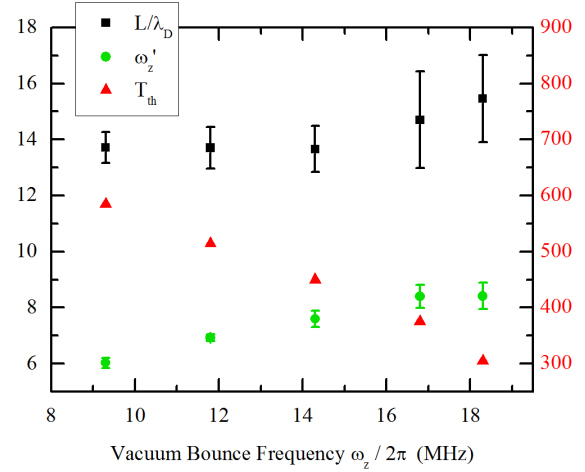


Figure 5.16: Plasma parameters L/λ_D and ω'_z (left axis) determined at $T = T_{th}$ (right axis) for five curves shown in Fig. 5.15. Error bars represent the range of simulated values for $T = T_{th} \pm 50$ K.

well shapes scale such that the ratio $L/\lambda_D \approx 14$ is nearly constant (see Fig. 5.16). While L is not changing much as the plasma cools (10–20%), $\lambda_D \propto \sqrt{T}$ shrinks by nearly two orders of magnitude, so the concordance of values L/λ_D within 10% at $T = T_{th}$ may be significant. On the other hand, at 1000 K and again at 20 K the values only differ by 25%.

At $T = T_{th}$ the effective bounce frequency $\omega'_z \approx 2\pi \cdot 7.5$ MHz varies by about 15%. Compared to the 100% variation at 1000 K ($2\pi \cdot 6.9$ – 12.9 MHz) and at 20 K ($2\pi \cdot 1.5$ – 2.6 MHz), this looks like a fairly fine-tuned parameter. Since the hypothetical bounce suppression goes as $\omega'_z/\Delta\omega_c$, and since $\Delta\omega_c \propto L$, a constant threshold ω'_z for different L values is not what one would naively expect.

These findings establish a strong correlation between flatter (not just longer) wells and higher cooling rate. That correlation alone is not sufficient to explain why there are two cooling rates rather than a smooth transition. The next step would be to take more data like in Fig. 5.15 for a few different values of N and $\Delta\omega_c$. That might help pinpoint which, if any, of the three mixing mechanisms described above ($\Delta\omega_c, \Delta\omega_z, \nu$) is most relevant to the transition from slow to fast cooling.

Since the system is better understood now than in 2015, it should be possible to improve the system's optimum. Previously, with no gradient, up to $\Gamma \approx 6$ s⁻¹ was reported for $2 \cdot 10^5$ electrons at 1.308 T. Now, using the gradient coil, the same cooling rate can be achieved for an order of magnitude more electrons at 0.775 T, where the free space cooling rate is nominally three times lower.

For this measurement B is first tuned to resonance, with ΔB as large as possible.¹⁵ Then

¹⁵The maximum ΔB is limited by the current $I \approx 2$ A through the gradient coil. More than this amount

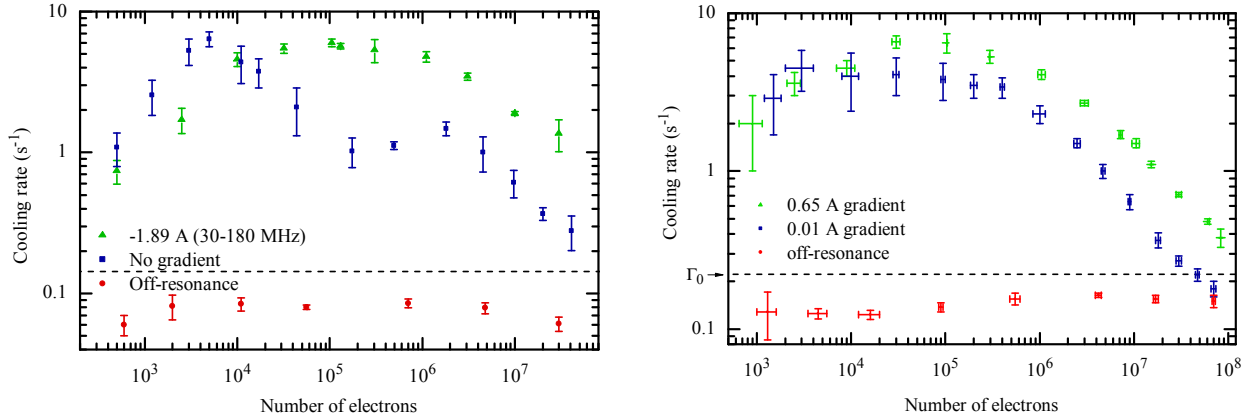


Figure 5.17: Left: Γ vs. N at TE_{121} in Cavity 1 ($B = 0.775$ T, $\Gamma_0 = 0.15$ s $^{-1}$). Right: Γ vs. N at TE_{141} in Cavity 2 ($B = 0.962$ T, $\Gamma_0 = 0.22$ s $^{-1}$). Free space cooling rate Γ_0 is indicated by a dashed line. The full cooling curve for the green point at $N = 83 \cdot 10^6$ in the right panel is reproduced in Fig. 7.2, Chapter 7.

the cooling time is varied to obtain T vs. t , from which Γ may be extracted. This is done for about 11 values of N spanning the range $10^2 < N < 10^8$. Then the entire process is repeated for two other settings: tuning to resonance with $\Delta B \approx 0$, and, for reference, completely detuning from resonance. The results are plotted on the left side of Fig. 5.17.

To maximize the contrast, for the off-resonant data set, B is tuned for the lowest cooling rate within a 1 mT range of the cavity resonance. This rate is apparently somewhat lower than the free space cooling rate Γ_0 , implying that the irises are still effective at reducing the coupling to free space even though they are less than one attenuation length long at this frequency ($\omega_c \approx 2\pi \cdot 20$ GHz). See Chapter 2.

The no-gradient curve has an unexpected dip around $N = 10^5$. This is about the range of N where the Γ_{hot} , Γ_{cold} problem arose in the TE_{111} data. In this data, however, there is no knee, only cooling at a lower rate.

In the hope of clarifying the T_{th} issue the strong-gradient scan was repeated using the short well. The knees came right back. Moreover, it is apparent in Fig. 5.18 that, when it can be determined, Γ_{cold} for the short well is close to the strong-gradient values in the long well. These observations can be summarized as follows. Cooling higher N requires a flat well and a field gradient. If the well is not flat, cooling is suppressed until the well is flattened: a knee in T vs. t appears. If the gradient is insufficient, the mixing is poor no matter how flat the well is, and there is no threshold behavior, just slow cooling.

The gradient coil was designed to terminate close to the center of Cavity 1 and produces the strongest gradient there (see Section 2.3). Cavity 2 is only $2 \cdot 2.54$ cm from the other end of the coil. The gradient there is a factor of 2.5 weaker but because of the length of the

may exceed the rating of some feedthru components. Extra care is necessary as a rating is not always given for low temperature operation.

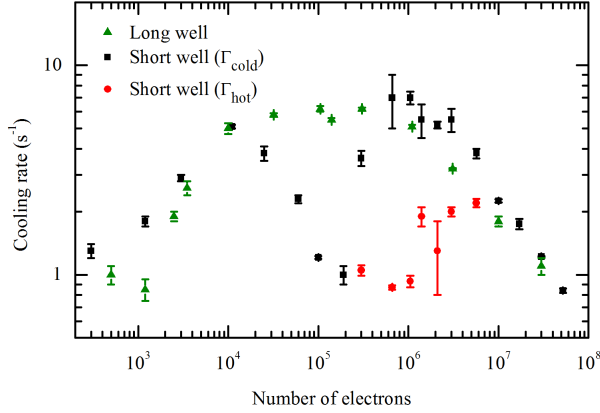


Figure 5.18: N dependence of the poorly understood cooling suppression. Similar to Fig. 5.17; “Long well” is the green data set there. Long and short wells are the same as elsewhere (Fig. 5.10). Γ_{cold} , Γ_{hot} are explained in Fig. 5.14

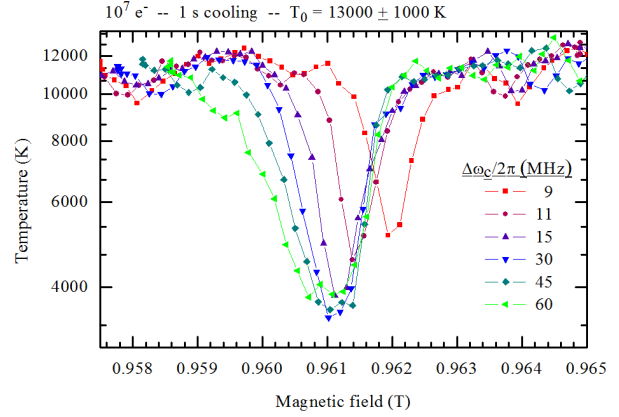


Figure 5.19: T vs. B at TE_{141} in Cavity 2, showing how settings were chosen for Γ vs. N : fix $N = 10^7$ electrons and scan T vs. B for varying ΔB . The 30 MHz curve is optimal.

Cavity	Mode	Field	Q	$1/V_{eff}$	Γ_1	N_{ovld}
1	TE_{121}	0.775 T	1600	$0.83 \cdot 10^6 \text{ m}^{-3}$	60 s^{-1}	$1.5 \cdot 10^6$
2	TE_{141}	0.965 T	2000	$0.29 \cdot 10^6 \text{ m}^{-3}$	25 s^{-1}	$3.5 \cdot 10^6$

Table 5.1: Comparing TE_{121} in Cavity 1 and TE_{141} in Cavity 2. Q and V_{eff} come from a simulations by Evetts in HFSS. The overload number N_{ovld} is defined by $N_{ovld}\Gamma_1 = \omega_\lambda/Q$.

electrode the plasma is typically four times longer, so one can access a similar range of $\Delta\omega_c$. The increased length implies a lower bounce frequency ($\omega_z \approx 2\pi \cdot 3 \text{ MHz}$), comparable to the long well in Cavity 1, so there should be no knees in the cooling curves in Cavity 2. Indeed, in Cavity 2 there has not been a single knee observed in T vs. t , nor even a dip in Γ vs. N . To study Γ as a function of N (right panel of Fig. 5.17) TE_{141} (0.962 T) was chosen because for $N = 1 \cdot 10^7$ the cooling seemed to be slightly better here than at any of the other modes with $B < 1 \text{ T}$. This is not surprising considering the discussion in Chapter 2: the TE_{141} is very well confined by the $(\Delta r/r) \approx 5 \%$ bulge, leading to a low mode volume and high Q , similar to the TE_{121} in Cavity 1 (see Table 5.1).

It is not necessary to run the gradient coil at maximum in Cavity 2, perhaps because of the apparent relative absence of bounce suppression. Instead ΔB is tuned empirically by fixing $N = 1 \cdot 10^7$ and measuring T vs. B for different values of the current I through the gradient coil. ΔB and B are fixed at the values that give the lowest T after 2 s of cooling.

A look at Fig. 5.17 and Table 5.1 reveals that the maximum cooling rate Γ_1 has not been reached for any number of electrons, in either cavity, with or without a strong gradient. One might expect $\Gamma_{max} \approx \frac{1}{2}\Gamma_1$ or so due to overlap effects (the electrons are not at the

maximum of the cavity field), but these should be small for low- N plasmas, which are relatively short. Another factor of 2 or so could well come from the bell-shaped nature of the cavity's frequency space representation (Fig. 5.7). Γ_1 is the cooling rate for a single electron sitting at the center of the bell curve. Cooling more electrons requires that the rest of them are at some detuning, somewhere below the peak in Fig. 5.7. Along these lines it is important to remember that the spread $\Delta\omega_c$ is not 100% efficient at mixing energy into the collective mode, but is 100% efficient at putting electrons off resonance. Finally there is a plasma effect worth considering, or rather the disappearance of a plasma effect: the curves turn over at low N . The cavity cools only T_\perp , whereas T_\parallel is what Tdiag reports (see Tdiag discussion in Chapter 3). The cooling rate for the parallel energy distribution cannot exceed $\nu_{\perp\parallel}$. No attempt is made to calculate the anisotropic relaxation rate for the wide range of parameters presented here. Note however that even for 10^6 electrons this rate should only be about 100 s^{-1} at $T_\perp = 10 \text{ K}$. Thus one could imagine that for 10^5 or fewer electrons it is impossible to cool T_\parallel faster than $\nu_{\perp\parallel} \sim 10 \text{ s}^{-1}$ or less, even though T_\perp goes to 10 K at a much faster rate. This effect would compete with the expected higher Γ at lower N , and may be responsible for the concave-down nature of the Γ vs. N curves.

So much for the theoretical optimum; the cooling is still tremendously improved relative to free space. With better cooling one can reach lower temperature, as shown in Fig. 5.20, again for both cavities. Keeping B and ΔB at the values optimized for $N = 10^7$, the “final” temperature T_f after 20 s of cooling is measured for the broadest possible range of N . In Cavity 2, in the range $1 \cdot 10^6 < N < 5 \cdot 10^6$, the final temperature is $12.2 \pm 0.5 \text{ K}$.

In addition to the 0.5 K statistical uncertainty, there are systematic uncertainties associated with the adiabatic calculation, as well as space charge (Section 3.3).

For the adiabatic correction, all plasmas were assumed to have $r_p = 1.0 \text{ mm}$. The measured values for $1 \cdot 10^6 < N < 5 \cdot 10^6$ were actually $r_p = 1.2 \pm 0.1 \text{ mm}$, averaging over both N and over the 20 s of cooling. To determine the effect on T_i , the solver was run for $N = 3.04 \pm 0.01 \cdot 10^6$ and $T = 0.001 \text{ eV}$. It was found that $L_i = \{4.08, 3.98\} \text{ cm}$ for $r_p = \{1.0, 1.2\} \text{ mm}$, respectively. The correction factor was therefore slightly smaller than it should have been in the range considered. $T_i = T_f(L_f/L_i)^{2/3}$ will have been perturbed downward by the erroneously longer L_i , causing the calculated temperature to be too low by a factor of $(2/3)\delta L_i/L_i \approx 2\%$. Thus the temperature in the trap T_i was about 2% higher than quoted due to this systematic.

The error due to space charge can be estimated using the data in Fig. 3.8 was taken for similar parameters and shows that in this regime T is read from the first $\mathcal{O}(N/10000)$ electrons. The space charge, there 0.6 V on axis, will change by at most 0.06 mV, equivalent to 0.6 K. Note that to first order a reduction of space charge will cause fewer particles to escape over time, so that the measured temperature will be higher than the actual temperature.

The systematic errors appear to be smaller than the statistical error. The potentially larger systematic error would lead to the true temperature being lower than measured. The plasmas therefore reached equilibrium at 12 K or less. This fulfills the original experimental goal: the targeted number of electrons ($N = 3 \cdot 10^6$) has been cooled nearly to the wall temperature $T_w = 9 \text{ K}$ in a stable state.

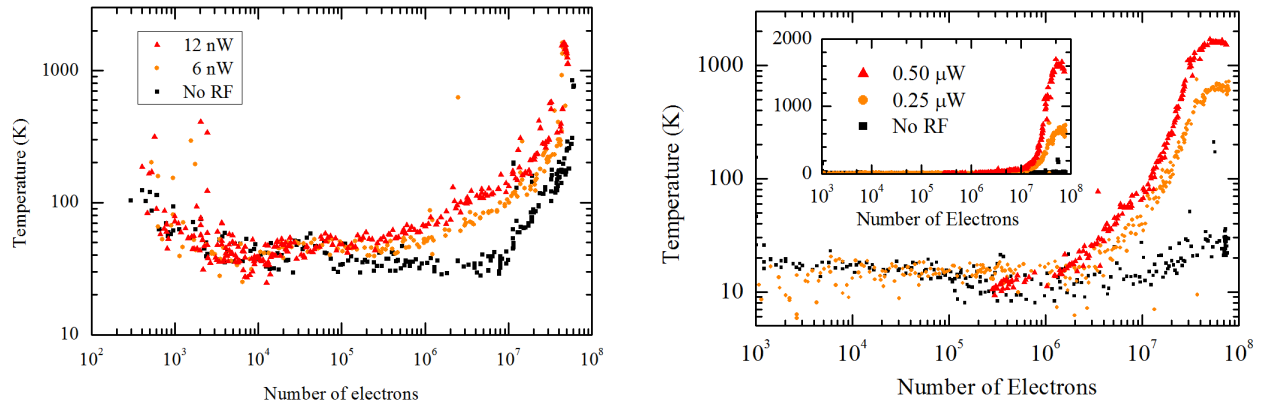


Figure 5.20: T_f vs. N in Cavity 1 and Cavity 2 for the optimal (green) parameters in Fig. 5.17. Cooling time is 8 s in Cavity 1 and 20 s in Cavity 2; this provides a minimum of 8 e-foldings in T for all points shown. Inset shows the data replotted with a linear vertical scale.

The excess of up to 3 degrees could be from heating due to expansion and electrode noise (recall Eq. 5.1). To characterize the latter effect, white noise is injected into the 1 MHz hi-pass filter going to the central cavity electrode (e3b or e8, respectively). The noise is gated on during the 8 or 20 s of plasma cooling.

The noise power given in the figures is V^2/R where V is the root-mean-square noise amplitude and $R = 50 \Omega$ is the input resistor to the hi-pass filter. The actual amount of power absorbed by the plasma is expected to be far less; the plasma should primarily absorb power in a few narrow bands at normal mode frequencies (see Section 7.1).

T_f is given in Fig. 5.20 for two power settings. The linear scale in the right panel inset shows that the temperature in Cavity 2 increases approximately linearly with noise power for a range of N . This trend is examined more closely in Fig. 5.21, where T_f is measured for a fixed number of electrons as the noise power is varied. There appears to be a good linear relationship between T and V^2/R in Cavity 2 and a somewhat nonlinear relationship in Cavity 1.

As exemplified in Figs. 5.20, plasmas tend to reach lower temperature in Cavity 2 than elsewhere in the trap, even off-resonance. The present T vs. H data indicates that noise power couples far less effectively to the plasma when it is confined there. This may be explained by electrode geometry. For both cavities, the plasmas in Fig. 5.21 had a length of about 4–5 cm. For a 5 cm long plasma, 1 V applied to the central electrode of Cavity 1 produces a voltage drop of about 0.400 V from $z = 0$ to $z = L/2$. In Cavity 2 that number is 0.035 V. Thus, one expects plasmas in Cavity 1 to be more sensitive to electrode noise in proportion to the power (V^2), or $(0.400/0.035)^2 \approx 100$ times more sensitive assuming the same noise on every electrode. The scaling in Fig. 5.21 agrees with this rough estimate: it takes 10 nW to reach 100 K in Cavity 1, but 1000 nW to reach 100 K in Cavity 2.

Finally, a broad and comprehensive view of the resonant cooling effect is presented for

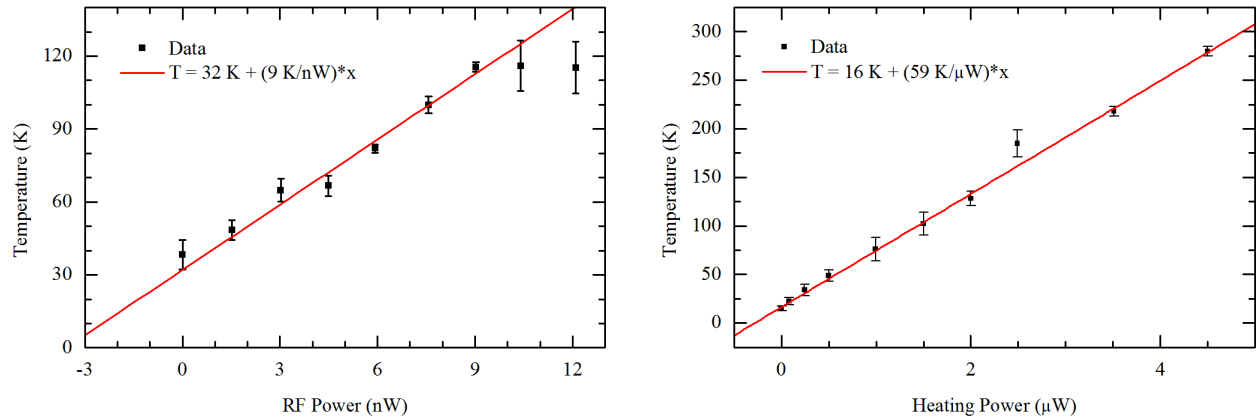


Figure 5.21: T_f vs. H for $7.5 \cdot 10^6$ electrons in Cavities 1 (left) and 2 (right). The fit curves intersect wall temperature (9 K) at -3 and -400 nW in the left and right graph, respectively. The smaller of the two numbers may be interpreted as an extra 0.5 mV of “environmental” noise on the electrode (see text for voltage-to-power conversion); this is of the same order as what is actually measured on a typical electrode line with no “added” noise. The larger number obtained in Cavity 2 is a measure of how irrelevant a few mV of electrode noise are in this cavity; the heating is coming from something else, like plasma expansion.

$N = 2 \cdot 10^6$ electrons. In Fig. 5.22, T is plotted against B for the entire accessible range of fields $0.1 < B < 1.5$ T and a variety of plasma conditions (see caption). In accord with the rest of these findings, modes without nodes at cavity center can be accessed by either applying a gradient (in Cavity 1) or moving the plasma to a node off-center (in Cavity 3). The mode structure in Cavity 2 is similar to what one would expect for a simple cylinder, as calculated for the original electrode stack in the thesis of Povilus [76].

The plasma reaches significantly lower temperature in Cavity 3 than in Cavity 1 in this data set. This may be interpreted as further evidence that a plasma covered by many short electrodes is heated relatively more by electrode noise. Cavity 1 has the same length as Cavity 3, but Cavity 1 has nine electrodes while Cavity 3 has three. Cavity 2, which is just one electrode, is the best of all. Data for Cavities 1 and 3 was taken after 16 s of cooling, corresponding to the red curve for the Cavity 2 data. Plasmas held for an equal amount of time in Cavity 2 seem to reach wall temperature at about half the field required in the other two cavities. The averaged curve for Cavity 2 is also consistently lower, reaching 500 K at about 0.5 T lower field than the top and bottom panel.

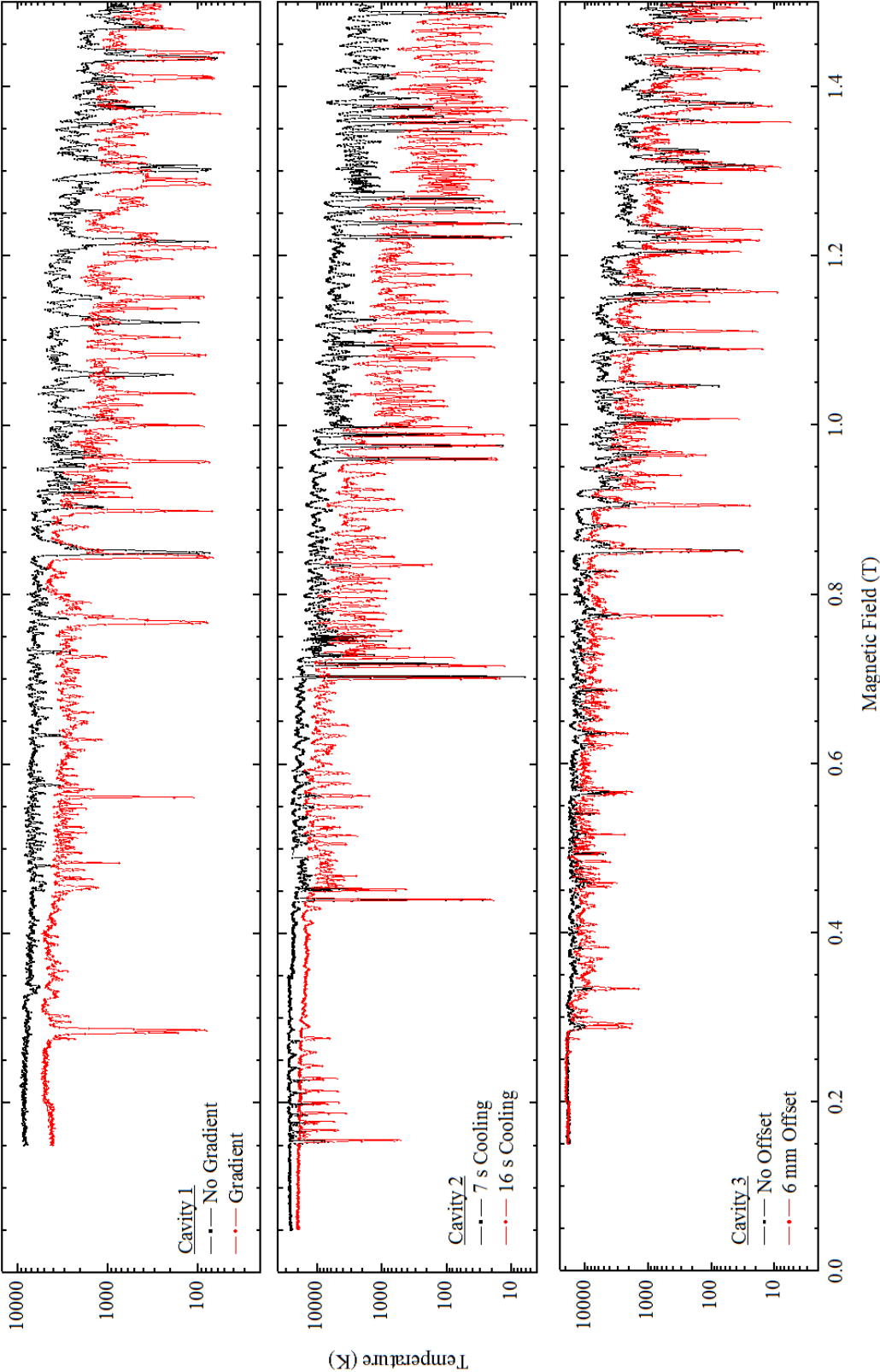


Figure 5.22: Complete magnetic field scan showing the mode structure of all three cavities. Raw temperatures are shown (no adiabatic or on-axis corrections). $N = 2 \cdot 10^6$ electrons for all three panels. The Cavity 2 data was taken using an extra-shallow well and a small applied field gradient to ensure that no modes were “suppressed” by smallness of $\Delta\omega_c/NT_1$. The majority of this data was taken by Ethan Ward in Summer 2018.

5.5 Applications

The previous sections have addressed some of the fundamentals of cavity enhanced plasma cooling. The knowledge gained was used to make plasmas colder, faster. This section explores some of the limits of the new technology and considers its application in future experiments.

Low Field

In Cavity 2, the TE_{111} comes into resonance with the cyclotron motion at 0.155 T. At this field setting the free-space cooling $\Gamma_0 \approx 0.006 \text{ s}^{-1}$ is barely measurable. Using cyclotron-cavity resonance cooling rates exceeding 1 s^{-1} have been obtained for $N = 10^6$ electrons (Fig. 5.23). The resulting steady-state temperatures are significantly lower than has ever been achieved elsewhere for electron or positron plasmas at such a low field.

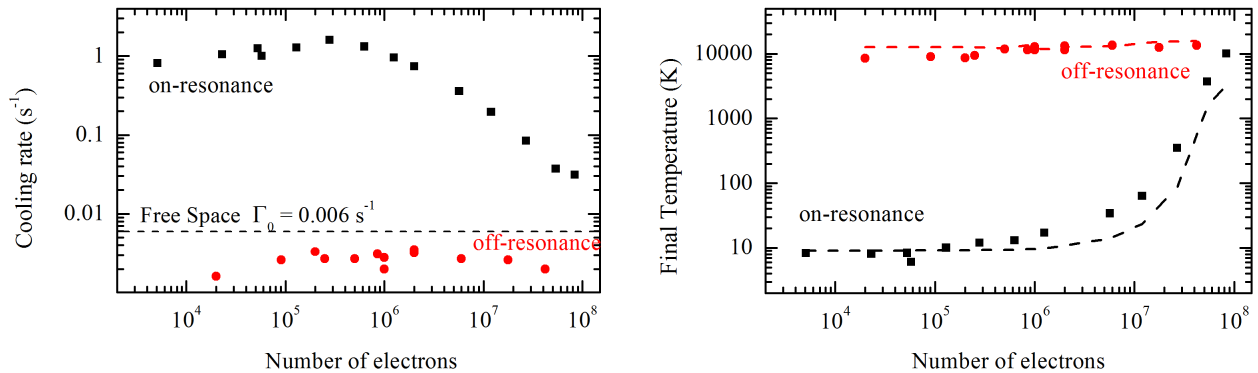


Figure 5.23: Cooling rate (left) and final temperatures reached (right) at 0.155 T in Cavity 2. No gradient was applied. Left: The cooling rate enhancement is greater than a factor of 100 relative to free space. The off-resonance measurements at 0.158 T set a very low bound on cooling from residual gas in the vacuum and even suggest that the irises (Section 2.1) are suppressing free-space radiation. Right: The dashed lines are estimates of the final temperature using Eq. 5.1. For Γ the measured cooling rate (Fig. 5.23) is used, and for H the heating is calculated from the measured expansion rate (not shown) using the expression given in Ref. [21]. Figures from [51].

The ALPHA plasma preparation could conceivably be modified to produce trappable antihydrogen in a cavity at low field. The measurements listed in Chapter 1, especially the hyperfine result, would be improved by operation at low magnetic field. A lower field reduces systematics and also allows a closer comparison to the highest precision measurements in hydrogen [71, 74], which are done at zero field.

Cavity-Cavity Coupling

If the microwave mode can absorb energy it can also give energy back (the interaction strength is the same after reversing the flow of time). This returning energy should be most significant when O’Neil’s matching condition is satisfied. The rate equations predict that a perfectly matched plasma ($\Delta\omega_c = N\Gamma_1 = \omega_\lambda/Q$), if steadily heated so as to maintain $T = 10,000$ K, would raise the temperature of the cavity mode to 3,000 K. If another, smaller plasma is also brought into resonance with this cavity mode, instead of resonantly cooling to 10 K this plasma should resonantly heat to 3,000 K.

In Chapter 2 it was shown that the TE_{111} is shared between Cavities 1 and 3 (this is the same mode used for the well shape studies in Fig. 5.11). The resonant structure as measured with a plasma (Fig. 5.24) indicates that cavity-cavity coupling persists in the completely assembled cryogenic trap, although the structure is somewhat different (cf. Fig. 2.4).

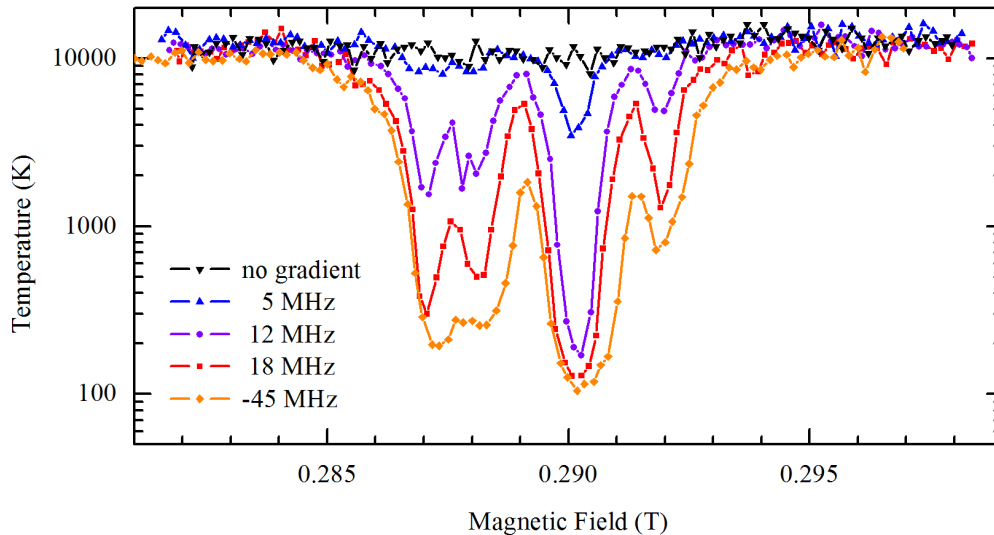


Figure 5.24: T vs. B at TE_{111} with variable gradient for plasma at cavity center. The cooling enhancement is completely suppressed with no applied gradient. Compare the two-or-three humped structure here to the bench measurement using a network analyzer in Fig. 2.4.

To demonstrate the postulated 3000 K sympathetic heating effect, one should

- i Prepare a “matched” plasma in Cavity 1
- ii Load another plasma simultaneously on-resonance in Cavity 3
- iii Heat the plasma in Cavity 1
- iv Observe whether the plasma in Cavity 3 heats up proportionally

Item (i) is the matching condition $\Delta\omega_c \sim N\Gamma_1 \sim \omega_\lambda/Q$. Section 5.4 partially characterizes the TE_{111} (Figs. 5.11, 5.12, and 5.13), but no parameters were found for which $\Gamma \rightarrow \Gamma_1 \approx 4 \text{ s}^{-1}$. Because the curve in Fig. 5.13 is not well fit for Γ_1 or ω_λ/Q different from their

nominal values by more than 20%, the most reasonable assumption is that these numbers are correct. Using these values, a matched plasma would have $N \approx 36 \cdot 10^6$, roughly the same N used to generate Fig. 5.13. The peak of that curve corresponds to 0.9 A in the gradient coil when the plasma is in a short well.

In order to satisfy both (i) and (ii), Cavities 1 and 3 must be tuned to $B = 0.2905$ T simultaneously while a gradient (0.9 A) is applied to Cavity 1. The gradient coil introduces an offset in B which makes it impossible, in the current setup, to match ω_c simultaneously in Cavity 1 and Cavity 3. Using the figures in Figs. 2.13 and 2.14, one can calculate that at 0.9 A, the offset produced by the gradient coil is about 2.3 mT in Cavity 1 and 0.1 in Cavity 3. Cavity 3 is $13 \cdot 2.54$ cm upstream. An opposing gradient of 0.7 G cm^{-1} is then required to bring Cavity 3 into resonance while the original gradient coil is running. Huws Landsberger has been charged with wrapping a copper magnet around the whole experiment to provide this field. Using two coils of opposite polarity, separated by $17 \cdot 2.54$ cm ($4 \cdot 2.54$ cm offset on each side), Huws has calculated that such a field could be produced with about 1000 amp-turns per coil. That number is a third what would be required if the electrode stack were co-axial with the case of the experiment, but it is not [83]. With four turns of 0000 wire this would require 200 A at 0.3 V or 60 W per coil. The field from these extra coils would cancel about 1/4 of the original gradient field, so these numbers would have to be perturbed upward self consistently.

Steps (iii) and (iv) can be performed repeatedly, during a T vs. B scan through the TE_{111} , for varying heating power, with and without plasma in Cavity 1, with and without plasma in Cavity 3, &c. If successful, this experiment would demonstrate the possibility of energy sharing between plasmas separated by more than a light-nanosecond. The underlying physics implies that sympathetic heating is linearly suppressed by the number of intermediaries (here three, hence $10000 \rightarrow 3000$ K), and this is worth demonstrating to clarify the limitations of sympathetic cooling.

Electrodes with Constant Radius

Figure 5.22 does not show all the modes accessible in the experiment. It only shows cooling at modes trapped in the three intentional cavities. It is possible to find resonant modes under simple cylindrical electrodes as well. If the electrodes are not bulged the modes may not be well confined (small $1/V$). Another characteristic of such modes is that they tend to be relatively sharp: $\omega_\lambda/Q \sim 2\pi \cdot 1\text{MHz}$. The modes treated up to now are an order of magnitude broader. The narrow linewidth modes are not good at dissipating energy rapidly because the normal electrode walls are not very resistive. This limits the number of electrons which can be effectively cooled by the mode.

Several such modes are known to exist in the current trap. The one with the lowest frequency is represented by a single antinode between the radial step at the end of Cavity 1 and the downstream iris. The frequency of this mode was found using COMSOL prior to being verified experimentally (Fig. 5.25). The cooling rate Γ is estimated using $T_{0\text{ s}}/T_{10\text{ s}}$ for plasmas pushed into the last electrode, cooled, then shuffled back into Cavity 1 prior

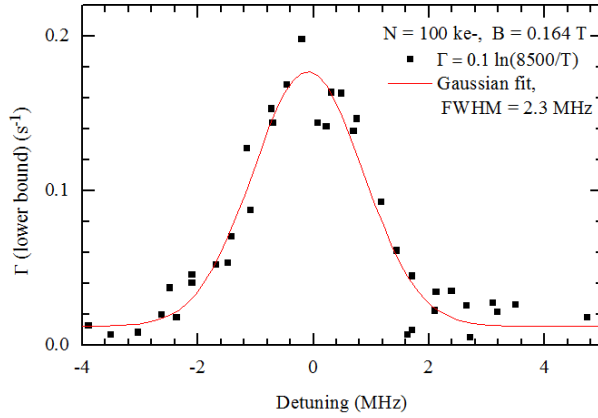


Figure 5.25: TE_{111} in the cylindrical section downstream of Cavity 1 in the current electrode stack. This mode has a narrow line ($\omega_\lambda/Q = 2\pi \cdot 2.3$ MHz or 0.07 mT) because it is concentrated in an area with gold-plated copper walls (low dissipation).

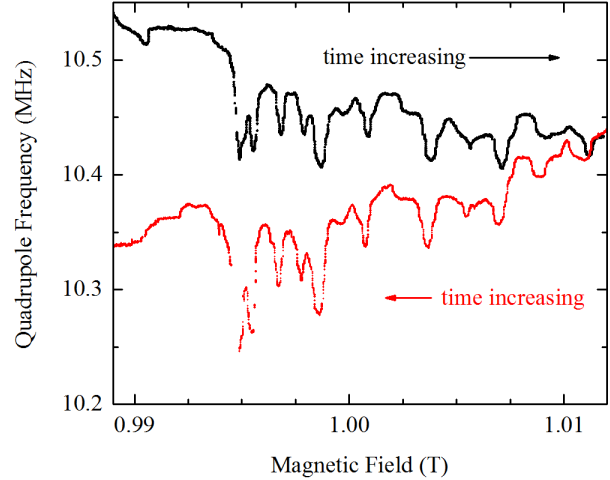


Figure 5.26: No-bulge resonances found near 1 T using the plasma modes diagnostic (see Chapter 7). Plasma expansion causes the quadrupole frequency to drift (decreasing in time), but the cooling peaks reproduce upon reversing the field ramp.

to measuring the temperature. As expected, this mode is much sharper than those in the intentional cavities. Γ was also hastily measured using T vs. t curves for $N = \{10^3, 10^4, 10^5\}$. Preliminary measurements indicate $\Gamma \approx 2$ s $^{-1}$ for $N \leq 10^4$ but $\Gamma \approx 0.5$ s $^{-1}$ for $N = 10^5$. This apparent turnoff with increasing N occurs an order of magnitude earlier than for the modes in the bulged cavities. This demonstration corroborates the foregoing explanation of the role of the cavity linewidth, but does not demonstrate that it is possible to obtain enhanced cooling in the more open geometry used by most experiments.

Back in 2015 all the electrodes upstream of the copper bulge cavity were standard constant-radius gold-plated copper. This 20 · 2.54 cm-long section was partially terminated at the upstream end by a flapper (which was probably never fully open or fully shut; see Section 2.1). At this time cooling data could be taken using a reservoir, which for this experiment was moved further upstream so that target plasmas could be loaded into the middle of the stack (so displace both plasmas in Fig. 5.2 upstream by about 4 · 2.54 cm). Resonant cooling (Fig. 5.26), though just detectable for $N \sim 10^6$, was significantly faster than free space cooling only for $N \sim 10^4$. It was not possible to determine whether the cooling would be better for $N < 10^4$ because at that time 10^4 electrons was close to the sensitivity limit of the temperature diagnostic. Consistent with the rest of the observations that year, the cooling was better when the target was on the edge (according to simulations of the mode structure) of the mode rather than at an antinode.

A more difficult measurement was then attempted: is the mode frequency or cooling rate changed by shutting the flappers? One would expect so, as this should presumably raise

the Q of the mode. This was the last day of the run. The flappers were not tested earlier for fear they should freeze shut or burnout, as had occurred in the previous run. B was tuned to resonance with the strongest peak. Persistence of the cyclotron-cavity resonance was tracked by observing the temperature of the target plasmas drawn from the reservoir: a low $T \sim 50$ K after 16 s of cooling indicated cavity resonance. Current was then sent to the flappers. The idea was to hold the upstream flapper closed once the reservoir was in, periodically opening and closing the downstream flapper each time a target plasma's temperature was to be taken.

The criterion for a “closed” flapper was that it would interrupt a beam of electrons from the egun. It was found that it took about 300 ms and at least 1 A of current to move the flappers sufficiently to block a beam of electrons from the egun (this was the criterion for a “closed” flapper). For one of the flappers the current had to be applied steadily to keep blocking beam.

These findings provide little confidence that the flappers were completely closed for a significant amount of the cooling time. The amount of current required was so high that it led to significant heating of the flapper, evidenced by offgassing (steady increase in pressure). Eventually the flapper appeared to seize in the open state, perhaps due to thermal expansion. After a small number (two or three reservoirs' worth) of attempts with no apparent change in target temperature, it was found that no reasonable amount of current could move the flapper so as to block beam anymore.

ALPHA

The present work shows that a small modification in electrode geometry and a different electrode material can be used to cool plasma 10 – 100 times faster and reach lower final temperature. For reference, after optimization ALPHA can often cool $3 \cdot 10^6$ positrons to 30–40 K at a rate $\Gamma \approx 0.24 \text{ s}^{-1}$. In Cavity 2 at Berkeley one can cool the same number of electrons to 12 ± 1 K at a rate $\Gamma \approx 3 \text{ s}^{-1}$. That's 16 times faster cooling to a temperature 10 times closer to wall temperature (30 with 5–6 K walls vs. 12 with 9 K walls). This method is really as promising for antimatter technology as was suspected at the start of the project.

The ALPHA collaboration has decided not to invest in a cavity. Due to other advances [15], the collaboration now routinely produces hundreds of antiatoms per hour (compared to a few per day in 2008). For many purposes this is good enough. Cavity cooling may well improve antihydrogen trapping if it were implemented, but to do so could jeopardize a physics program which is now flourishing. The collaboration is unwilling to incorporate a cavity because

- i It is not strictly necessary
- ii Nichrome, titanium, or stainless steel electrodes could perturb the magnetic field
- iii The strong magnetic field gradients used for trapping antihydrogen could make it difficult to tune to resonance or optimize $\Delta\omega_c$

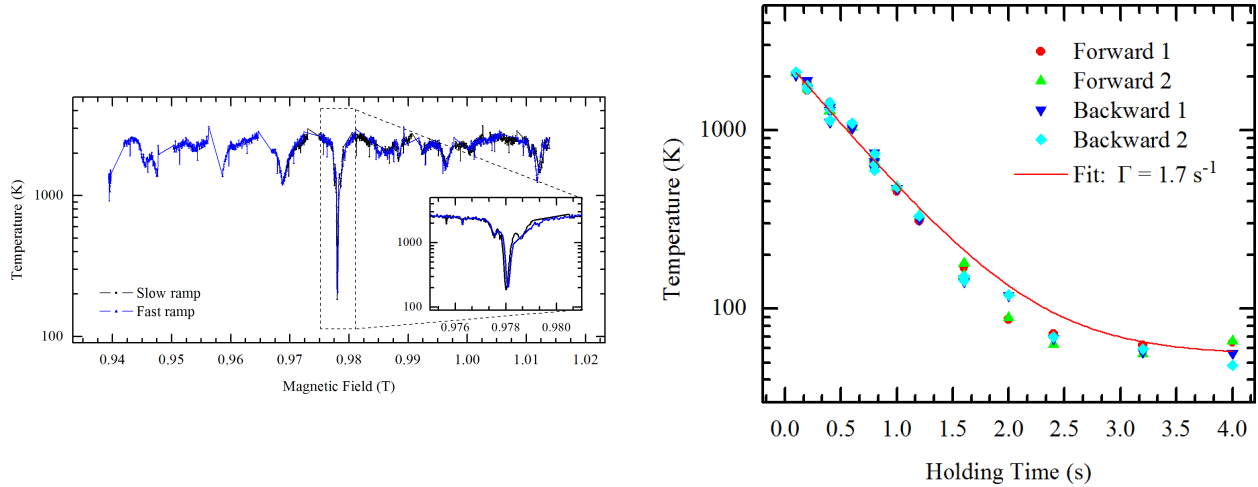


Figure 5.27: Cavity resonances found in ALPHA-2 using the reservoir technique. The measured $Q \approx 4000$ for the central peak in the left panel (possibly $\text{TE}_{1,4,19}$). Assuming the mode uniformly fills the entire atom trap, $\Gamma_1 = 0.38 \text{ s}^{-1}$. By fitting the data on the right to the equation $T = 60 \text{ K} + T_0 \exp(-\Gamma t)$ one obtains $\Gamma = 1.7 \text{ s}^{-1}$. This value suggests that the average E field in the total volume is 1/5 its value at the plasma center, which is quite reasonable (the equivalent factor for the TE_{121} in Cavity 1 at Berkeley is about 1/10).

- iv A bulge would reduce the usable trapping depth of the magnetic bottle
- v Colloidal graphite has not been tested in an antiproton trap

In 2017 some evidence was obtained suggesting that cavity cooling could work in ALPHA-2 even without a proper cavity. The electrodes in ALPHA-2 are not bulged but do contain two radial steps, and simulations suggest that many high- Q modes may be found in the central region of the atom trap. ALPHA uses aluminum alloy for its electrodes, which is not as “bad” as copper at low temperature but still a factor of 100 more conductive than the titanium. The experiment was limited by other factors. The main solenoid for ALPHA-2 has fewer turns than the one at Berkeley, requiring five times more current for the same B . The helium boiloff due to I^2R losses¹⁶ is enough to make the usual scans of T vs. solenoid B unfeasible. Instead, the 1 T mirror coils were used to change the field.¹⁷ The tests were therefore done in the strong gradient of a mirror coil because that is where positrons are normally placed when they are mixed with antiprotons. The uncertainty $\delta B \sim \nabla B \cdot \delta z$, where z is calculated with respect to the nominal center of the mirror coil, was large and not obviously reproducible due to superconducting hysteresis effects and time dependent disagreement between the requested mirror current and that measured by the DCCT’s.

¹⁶ R is not zero in the copper leads, which deliver the current to the superconductor when the field is ramped. These leads are in electrical and therefore thermal contact with the magnet.

¹⁷Thanks to Dan Maxwell for adding and testing this functionality. These are million dollar magnets.

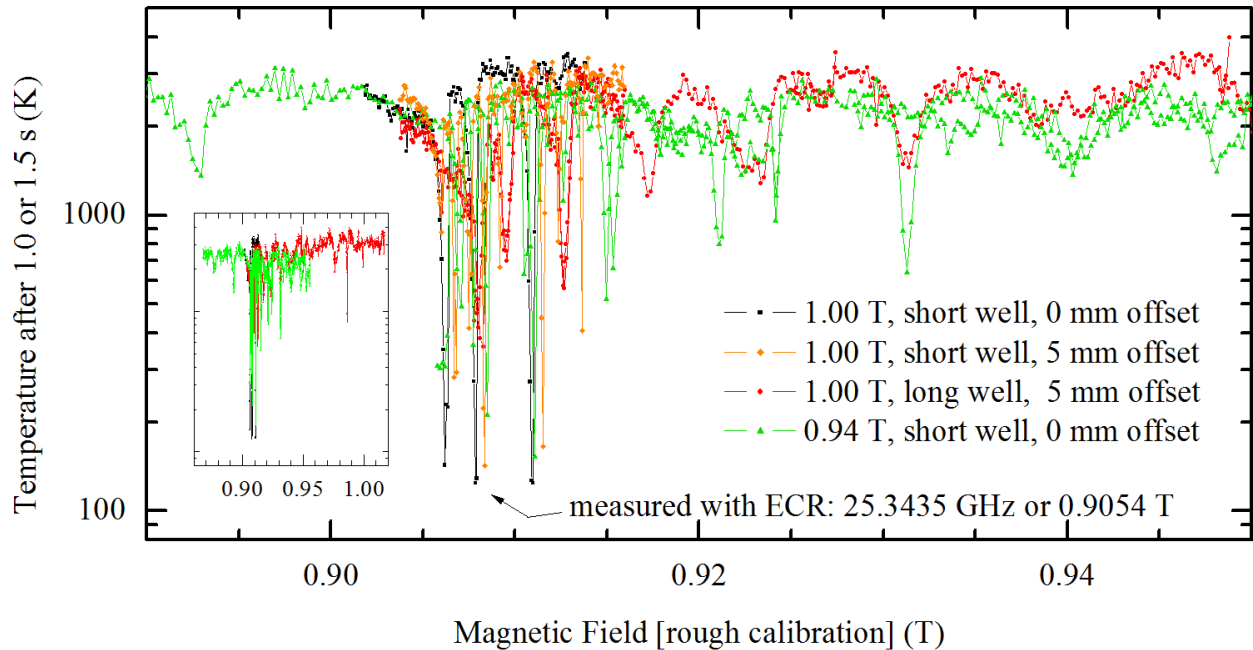


Figure 5.28: Scanning through the TE_{14x} with the reservoir in ALPHA-2. The magnetic field was measured using reservoir ECR for the putative TE_{142} . The legend gives the background (solenoidal) field, well description, and axial offset from trap center. Inset shows the full range of the scans. Estimated cooling rate $\Gamma \approx 2\text{--}3 \text{ s}^{-1}$ for the three strongest peaks (presumably TE_{141} , TE_{142} , and TE_{143}).

Despite all this, a strong but narrow cooling peak was found (Fig. 5.27) which appeared to work for at least $2 \cdot 10^5$ electrons. The peak was found in a range where there should be no low-order resonance, meaning the cooling was through some high-order mode. For example, the UBC collaborators simulated that the $TE_{1,4,19}$ should be close to $\omega_c = (e/m) \cdot 0.988 \text{ T}$. Following this preliminary result, it was possible to ramp the main field down enough to repeat the scan and, according to a hasty calculation, reach the TE_{141} (Fig. 5.28). The TE_{14x} peaks, if that’s what they were, were also quite sharp (about 0.3 mT in the black curves).

The next step taken was to run the standard positron preparation sequence ($N = 3 \cdot 10^6$) on resonance. No resonant cooling enhancement was observed. This was first interpreted according to the expectation that an aluminum cavity has low resistivity, giving a sharp line which can only cool low N . It was soon apparent that the length of the positron plasma in the standard sequences exceeded that of the small target plasmas. Given that the cooling was already limited by the excessive width $\Delta\omega_c$ of the target, it was not reasonable to expect a large enhancement with the much longer positron plasma. In other words the experiment was doomed to fail with such a long plasma in such a strong gradient. Because of beam-time limitations it was impossible to perform a more careful experiment.

It is not obvious from these experiments whether the “accidental cavity” could be used

to improve the antihydrogen trapping rate. It is possible that the factor of five cooling enhancement observed with smaller plasmas may extend to the $3 \cdot 10^6$ positron plasmas used for antihydrogen production, provided that the range of cyclotron frequencies $\Delta\omega_c$ is chosen properly. There is however a significant caveat, alluded to earlier: is the mode being damped by the walls, or by leakage? In the latter case, one should still measure resonant cooling, but only down to the temperature of whatever thermal bath receives the leaking mode power, according to the hypothesis given in connection with the Cavity-Cavity experiment. This may provide further motivation for that experiment.

Chapter 6

Precision ECR Magnetometry

The cyclotron frequency $\omega_c = qB/m = 2\pi \cdot 27.992490 \text{ GHz} \cdot B[\text{T}]$ is within the range of many microwave synthesizers. After connecting a synth to a microwave horn one can broadcast microwaves into the trap and look for the drive frequency which heats the electrons the most. In principle this frequency should be ω_c . The value of B , averaged over the plasma, is therefore determined provided one can identify the correct heating peak. This technique is called electron cyclotron resonance (ECR) magnetometry and was first implemented in a Penning-Malmberg trap by Friesen et al. using the ALPHA-1 machine at CERN [39] (Section 6.1).

In 2017, a $\times 5$ faster, $\times 100$ higher precision measurement was obtained by incorporating the plasma reservoir. The improved technique was used to map the on-axis magnetic field of ALPHA-2 (Section 6.2).

Further refinements in 2018 yielded yet another factor of 100 improvement in precision. This permitted a thorough study of systematic shifts and sideband structures (Section 6.3).

Although these developments were pursued as a “sideline” to the primary thesis topic, cavity cooling, the ECR work is of more immediate significance to ALPHA. Measurements of the gravitational mass of antihydrogen in ALPHA-g will require the most advanced ECR methods reported here (Section 6.4). Specifically, the precision of the antigravity measurement is expected to be limited by uncertainties in the measured magnetic field.

6.1 Initial Applications

Modes-based diagnostic at CERN

The frequencies of the normal modes of a plasma depend on the plasma shape and related properties such as temperature and number of electrons (for the latter, see Section 7.2). The temperature effect can be used to obtain an *in situ* measurement of the magnetic field. This “Plasma Modes Diagnostic” is performed by monitoring the frequency of the quadrupole mode (see Fig. 6.1) while firing a sequence of microwave pulses at the plasma. The mode

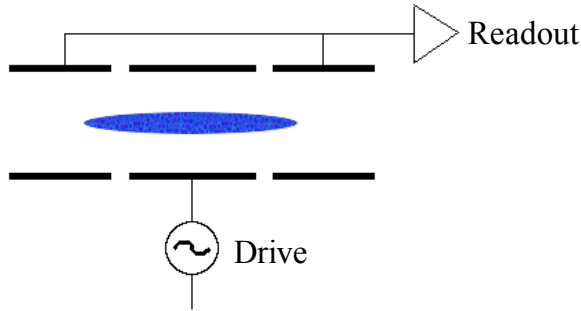


Figure 6.1: Cross-sectional schematic of the modes diagnostic showing plasma (blue), electrodes (black), and amplifiers. An alternating voltage on the middle electrode can stimulate the “breathing” mode [88]. The axially expanding/contracting plasma then pushes/pulls conduction electrons to/from neighboring electrodes. This tiny oscillating charge signal may be amplified and detected for plasmas with $N \sim 10^7$ or more.

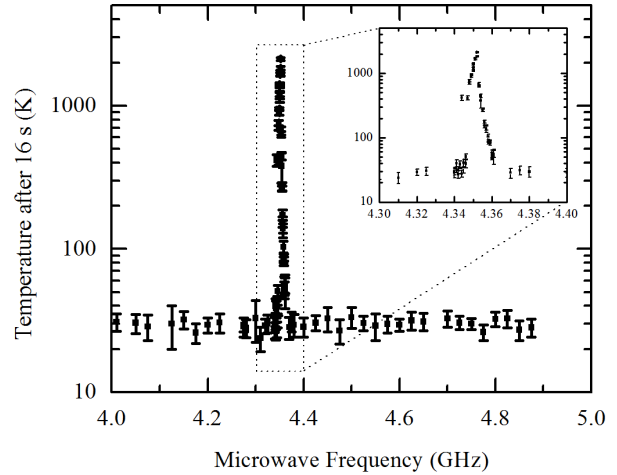


Figure 6.2: The first ECR heating peak measured in the experiment at Berkeley, using directly measured plasma temperatures. This peak occurs at a much lower frequency (and magnetic field) than has been accessed by the Modes Diagnostic.

frequency is found to increase sharply when the microwave frequency is within 5–10 MHz of the cyclotron resonance. By making a plot of plasma mode frequency vs. microwave frequency, one can estimate the cyclotron frequency of the plasma and thence the local magnetic field. For more details see Refs. [7, 39], and Friesen’s thesis [38].

The Modes Diagnostic has been used for years by ALPHA as a consistency check. In order to combine antihydrogen runs from different days, the superconducting solenoid is “reset” a few hours before each run by temporarily breaking the superconducting loop while flowing a reproducible current (186 A) through it. The field is then checked by running the modes diagnostic and confirming that the peak frequency, and therefore the axial magnetic field, is roughly (10^{-3}) the same day-to-day.

Long Slow Scans at Berkeley

At Berkeley it only¹ takes 25 s to load a new plasma, heat it with microwaves at some frequency f , and dump it to measure T . Thus, in an apparatus designed for rapid cycling, the modes diagnostic described above is not faster than simply looking for a heating peak in a scan of T vs. f , using the standard plasma temperature diagnostic (Tdiag) to measure T . Further, the modes diagnostic requires a large plasma in a maximally harmonic well. Doing the scans with Tdiag allows one to use any plasma, at any location, at any magnetic

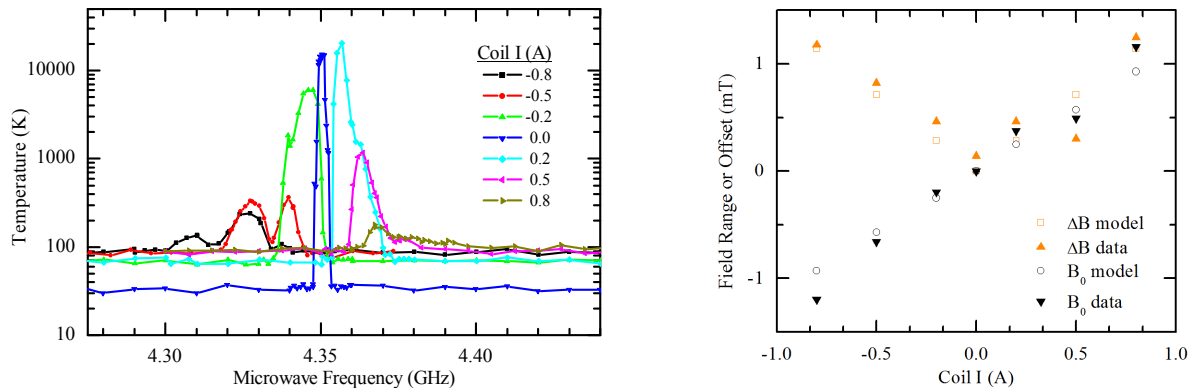


Figure 6.3: Temperature response of single plasmas to microwaves in Cavity 2, for various applied gradient fields, close to the TE_{111} resonance at 4.350 GHz. The right panel is populated using eyeball estimates of the length and center (in MHz) of the heatable region for each coil setting. The good agreement with the offset B_0 and range ΔB predicted using the coil model of Section 2.3 suggests that bounce suppression is not significant for a long plasma in Cavity 2, at least for the purpose of heating.

field—provided the microwave excitation can reach the plasma—as many times as desired. .

These were called Long Slow Scans (May 2017), because, with the benefit of egun feedback (see Chapter 2), the experiment could be automated and left riderless for hours while hundreds of points accumulated. For the first scans a 8 GHz Lab Brick was borrowed from the Siddiqi Lab. The microwave power entered through the hi-pass input of an unused electrode.² The heating curves were used to confirm the calibration of some cavity resonance frequencies and to estimate the gradient produced by the dipole coil. This was an opportunity to directly measure the range of cyclotron frequencies $\Delta\omega_c$ available to the electrons (see Section 5.3). Typical data is shown in Fig. 6.3. The result was difficult to interpret. Microwave power accumulated preferentially at cavity resonances. This distorts the line-shape, potentially even cutting off relevant parts of the distribution if it is not centered on the resonance. Another problem was the multiply-peaked structure, which is examined in detail in Section 6.3.

6.2 Mapping the ALPHA Trapping Fields with the Reservoir Technique

The author was informed upon arrival at CERN (September 2017) that his job was to set up a reservoir sequence (Chapter 4) for doing Tdiag-based ECR. Tim Friesen and others

¹The machine at CERN takes three or four times longer to complete these operations because the egun, MCP, and microwave horn must be moved into the beamline individually every time they are used.

²The electrode lines passed sufficient power to heat a large plasma for $\omega < 2\pi \cdot 10$ GHz, but the 12 GHz microwave horn was more effective at all microwave frequencies tested.

had recently done some single-plasma scans suggesting Tdiag produced a narrower line than Modes, but in ALPHA-2 these load-cool-heat-dump scans take too long to be practical.

Using the reservoir to rapidly produce a sequence of 100 small plasmas allows 100 T vs. f points to be acquired in little more than the time it takes to prepare 1 large plasma. Fig. 6.4 compares reservoir ECR to its predecessor. Because the target is naturally small ($N \sim 10^5$) the plasmas are short, so they sample a smaller range of $B(z)$ and produce a narrower line (here by a factor of at least 30, although even narrower lines are possible in deeper wells).

These measurements established Reservoir ECR as a fast method for making precise measurements of $B(z, t)$. The method was then used to characterize the spatial and time dependence of the fields used to study antihydrogen. Maps for two field configurations, obtained on September 22 and 23, are shown in Fig. 6.5. The field configuration used for laser spectroscopy (“neutral trap”) has its lowest minimum on the left side. That left-right asymmetry had long been suspected by more senior group members based on an observed asymmetry in reconstructed antihydrogen annihilation events during microwave kickout. The “microwave tweaked” field settings had been chosen so as to eliminate the observed annihilation asymmetry. ECR provided additional confirmation that the “tweak” put the minimum back in the center of ALPHA-2.

Later, Steve Jones and others (elog:21726) studied the time dependence of B after ramping the mirror coils and short solenoids, and Nathan Evetts (elog:21988) used a frequency doubler to do ECR directly under the +1 T mirror coils. In the latter case a set of peaks was found at regular intervals (about 50 MHz) instead of a single peak. Difficulty in identifying which peak corresponded to the true cyclotron resonance contributed to uncertainty in the measurement of B .

6.3 Higher Order Effects

The need to understand seemingly complex frequency response structures (encountered in the mirror maps mentioned above) was sufficient motivation to implement and refine the reservoir techniques at Berkeley in winter and spring of 2018. Because 20 GHz is the top of the range for most affordable synthesizers, this required modifying SDREVC to run at low

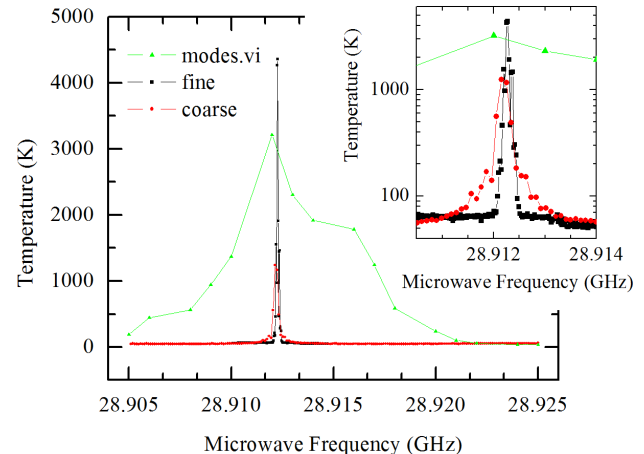


Figure 6.4: Reservoir ECR compared to Modes ECR. Green and red points were taken using 0.004 ms microwave pulses. Black points correspond to 1 ms pulses at $100\times$ less power. All three data sets were acquired within one two-hour window.

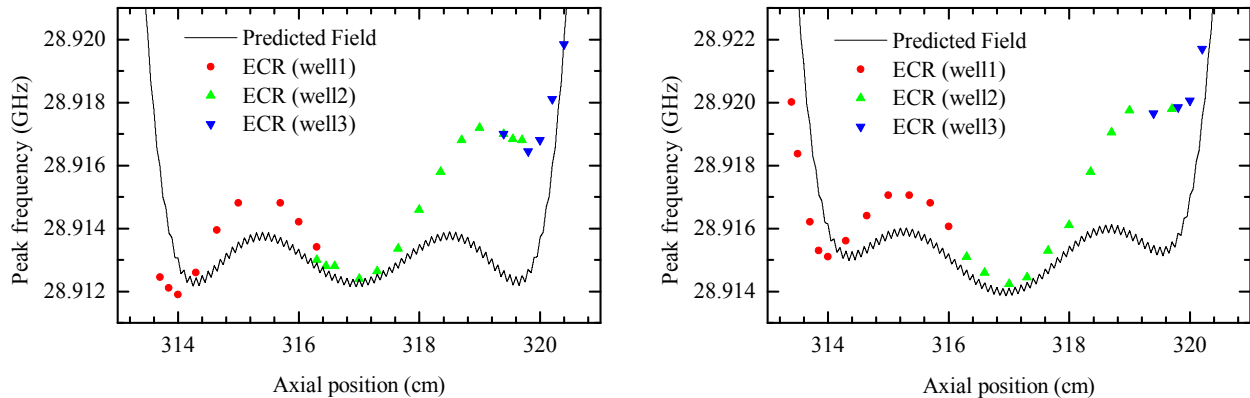


Figure 6.5: Maps of the trapping fields in ALPHA-2. Left panel is the “neutral trap” configuration used to trap antihydrogen atoms during laser spectroscopy, right is called “microwave tweaked” (see text). The black curve was generated by a code which uses the nominal geometry of the trapping magnets and the applied current.

field (see Chapter 4). The renewed interest in the plasma reservoir also led to important refinements to the target extraction protocol, in particular to colder target plasmas. These cold targets did not require EVC. The duration of the EVC procedure is longer than that of any other part of the sequence. By skipping the EVC step, the duration of the entire reservoir sequence was reduced to less than a minute. Speed may be an important factor for ECR in ALPHA-g. This is discussed further in Section 6.4.

Bounce frequency structures

Putting the plasma in a relatively shallow well ($\omega_z \leq 2\pi \cdot 10$ MHz) usually results in sidebands separated from the main peak by ω_z (Fig. 6.6). For deeper wells the sidebands are smaller and far enough from the main peak that they are often unmeasured (e.g. in Fig. 6.4). As discussed in Section 5.3, in the frame of an electron which bounces up and down along a plane wave (or cavity mode), the microwave field is modulated with period $2\pi/\omega_z$. With ECR heating one can resolve bounce sidebands much better than with cavity cooling because now a pure tone, rather than the $\mathcal{O}(30$ MHz) cavity linewidth, is convolved with the bounce frequency distribution. As mentioned earlier, this information could be used to test predictions from the previous chapter regarding mixing. For example, while in Fig. 6.3 the effective gradient is similar to the prediction, occasionally peaks-within-peaks are observed which are narrower than they should be if bounce suppression is not taken into account. Friesen et al. observed a similar effect with the Modes Diagnostic for sufficiently hot plasma [7]. Recall the hypothesis (Section 5.3) that colder plasma reduces the bounce suppression of the spread in cyclotron frequencies by flattening the well. A hot plasma in a deep well may improve the precision of Modes ECR by reducing sensitivity at frequencies that differ from the bounce-averaged cyclotron frequency.

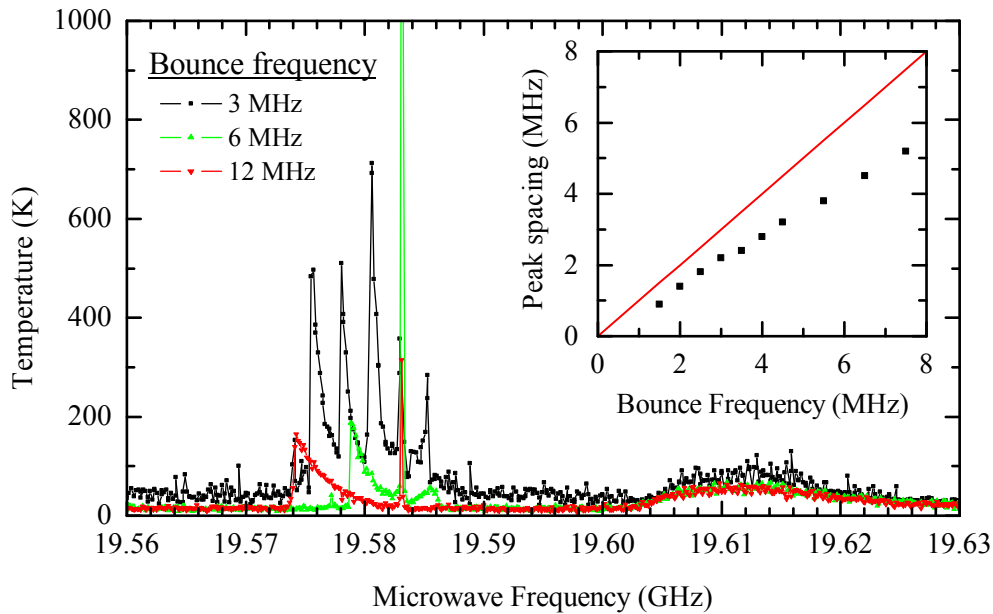


Figure 6.6: Broad microwave heating scan showing bounce sidebands and the response of the reservoir itself at higher field (see text). Sidebands are stronger on the left than on the right due, it seems, to an impedance mismatch which makes it difficult to heat at 19.59 GHz. Using the gradient coil to push the ECR peak to 19.59 GHz results in a barely detectable peak (not shown). The inset plots the spacing between successive sidebands as a function of calculated bounce frequency $\omega_z/2\pi$.

An inset displays show the dependence of peak spacing on calculated bounce frequency. The deviation at higher bounce frequency seems to be too large for a plasma effect (cf. Fig. 7.1, where a well with a similar degree of anharmonicity led to a significantly smaller downshift for more electrons). The ability to move the sidebands by changing the well depth makes identification of the central peak, which is at the cyclotron frequency and cannot change, relatively simple.

Another notable feature in Fig. 6.6 is the plateau around 19.61 GHz. This frequency corresponds to the magnetic field where the reservoir plasma is kept. Heating of the reservoir plasma contaminates the signal by making the target plasma start at higher temperature. This spurious signal can mimic or obscure the desired ECR heating peak if the magnetic field at the target is not kept well below the magnetic field at the reservoir plasma. Once again by varying the target well depth it is usually simple to determine whether the observed heating is due to microwaves absorbed at the target or at the reservoir.

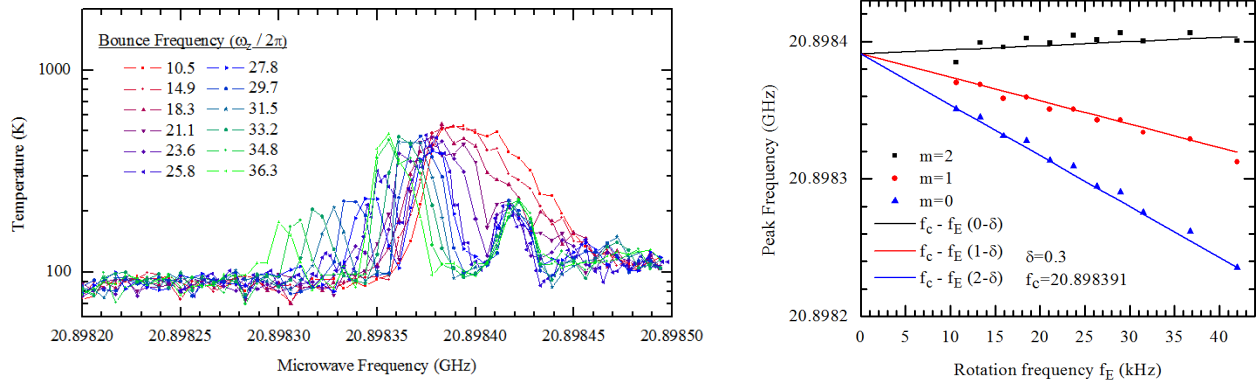


Figure 6.7: Rotation frequency scan for a needle-shaped plasma. Rotation frequency is increased by increasing ω_z . Positions of the three observed peaks in the left panel are plotted on the right with the same conventions as used by Affolter [1]. Independent linear fits to the three peak positions agree on the y -intercept ω_c to within 2 kHz or 0.1 ppm.

Rotation frequency structures

The strong electric field in a very deep well ($\omega_z \geq 2\pi \cdot 30$ MHz) produces a “magnetron” rotation of the target plasma. If the microwave electric field varies in the azimuthal direction, the field seen by a revolving electron will be modulated at the plasma rotation frequency ω_r . As before, this leads to sidebands in the microwave heating spectrum, now separated by ω_r . As long as the density³ of the target $n \leq 10^7$ cm⁻³, the rotation rate $\omega_r \approx \omega_z^2 / 2\omega_c$ will be primarily set by the trapping field. Just like in the bounce splitting case, one may obtain a set of spectra by varying ω_r via its dependence on ω_z (Fig. 6.7). Since the peak separation is only a function of the independent variable and the unknown ω_c , the latter may be constrained \sqrt{M} times better with a set of spectra containing M total heating peaks. This is the source of a factor of 7–8 improvement in precision. The rest of the claimed $\times 100$ improvement is a result of pushing the target into an unusual regime, described in the next section, which allows it to be shortened by an additional factor of ten or more.

Pancake plasmas

A typical plasma in a Penning-Malmberg trap is needle shaped with aspect ratio $L/r_p \geq 10$. Pancake shaped electron plasmas ($L/r_p \leq 1$) are not often discussed, but the shape is commonly encountered in laser-cooled ion plasmas. The pancake shape is advantageous for ECR because it samples a very small range of $|\mathbf{B}(r, z)|$, which varies primarily in the z

³This is the condition $\omega_p < 2\pi \cdot 30$ MHz, which is the bounce frequency ω_z corresponding to a typical ECR well. In what follows, the condition $\omega_p < \omega_z$ is fulfilled for the $N = 10^3$ set and violated for the $N = 10^5$ set.

N	T (eV)	ϕ_0 (V)	r_p (mm)	L (mm)	λ_D (mm)
$1 \cdot 10^3$	0.001	0.002	1.0	0.24	0.18
$1 \cdot 10^5$	0.010	0.236	0.7	2.00	0.12

Table 6.1: Numerical results for representative target plasmas from Fig. 6.8. L , ϕ_0 and λ_D are calculated using the Poisson solver (see Appendix C) for a 30 MHz well. Other parameters in the table are measured experimentally. The first row corresponds to a plasma preparation using more EVC (top of Fig. 6.8), second row less (bottom). In this case more EVC does not reduce λ_D , perhaps because the temperature was already low.

direction⁴.

One can minimize the length of the target by evaporatively cooling to the minimum possible temperature and confining it in a deep well (see Fig. 4.7 in Chapter 4). The resulting L may be less than 0.1 mm. N and T are both very low as well, but the ratio is such that the target is still somewhat in the plasma regime. Typical linewidths thus obtained are around 8 kHz in the pure solenoidal field at Berkeley. With such a narrow line, a sub-ppm measurement could in principle be done with only a handful of target plasmas. One could repeat that measurement 20 times from a single reservoir to obtain $B(t)$ with a temporal resolution $\mathcal{O}(1 \text{ s})$. This could be a way to map the rampdown in ALPHA-g (next section).

Figures 6.8 and 6.9 compare the spectra obtained with needle and pancake shaped targets. Plasma preparation is similar to that used in Fig. 4.6, but with more EVC; see Table 6.1. These two sets of spectra were taken back-to-back and somewhat interleaved to be sure the field hadn't drifted significantly between scans. The comparison highlights the importance of understanding the peak structure in order to correctly identify the true ECR frequency. In the pancake regime one obtains a simple nearly symmetric sideband structure on either side of the resonance at ω_c . In contrast to this nearly single-particle result, a needle-like plasma with higher N produces asymmetric spectra. The latter spectra look more like those obtained by Gould [43], Sarid [81], and Affolter [1]. This might be because those authors used quasi-electrostatic perturbations introduced on electrodes, whereas the present experiment is done with (electromagnetic) microwaves. The former have no $m < 0$ modes which can couple to cyclotron motion of an electron, whereas the latter do—only for finite r [60]. The $N = 10^3$ target plasmas are evaporatively cooled much more, so those have a larger radius.

For the $N = 10^5$ case it is tempting to interpret the extrapolated peak separation at $\omega_z^2/2\omega_c = 0$ to be the rotation rate $\omega_p^2/2\omega_c$ due to the plasma self field. Under this assumption one can calculate $n = 1.5 \pm 0.3 \cdot 10^7 \text{ cm}^{-3}$, which compares fairly with the value $n = 3.7 \cdot 10^7 \text{ cm}^{-3}$ obtained with the Poisson solver.

⁴ B_r and $\partial_r B_z \rightarrow 0$ on the axis of symmetry. Why? $B_r = 0$ there because any other choice would break cylindrical symmetry. Meanwhile $\partial_r B_z = 0$ because $\nabla \times \mathbf{B} = 0$ or $\partial_r B_z = \partial_z B_r$. The derivative on the right is zero because, as was just stated, $B_r = 0$ on axis for all z . One can also see, by considering axial field lines which diverge from a pillbox of radius and height $dr = dz$, that $\Delta B_r \approx (-1/2) \Delta B_z$.

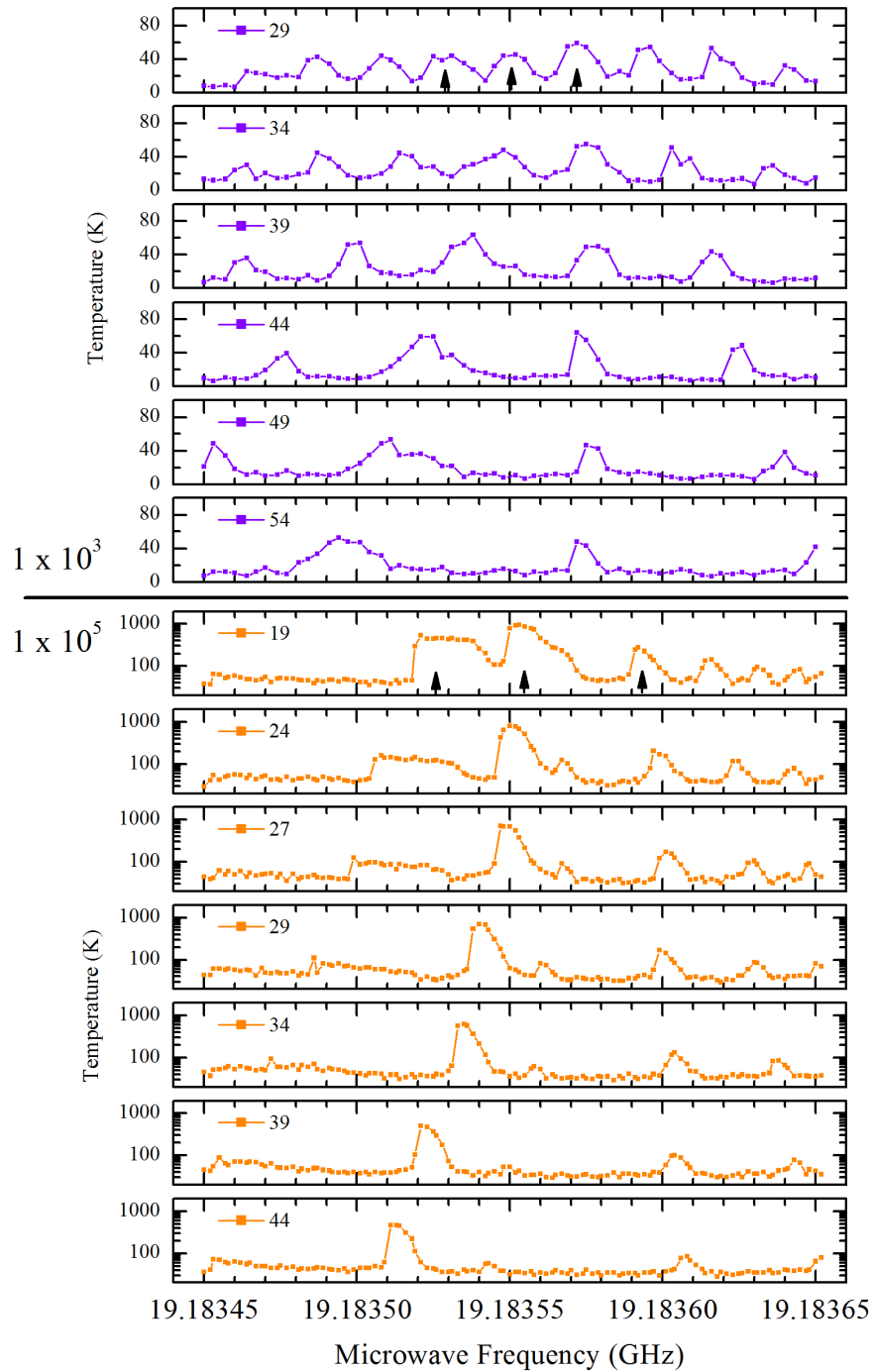


Figure 6.8: Simultaneous ECR spectra for needle and pancake plasmas. The unmoving purple peak at $2\pi \cdot 19.183575$ GHz is the cyclotron frequency $\omega_c = qB/m$, which determines the magnetic field at the center of the plasma to better than 0.1 ppm. As the bounce frequency is changed (legend), the observed peak structure seems to behave like the $m = \{0, 1, 2\}$ observed by Affolter [1] (these peaks are indicated by three arrows in the first trace of each series).

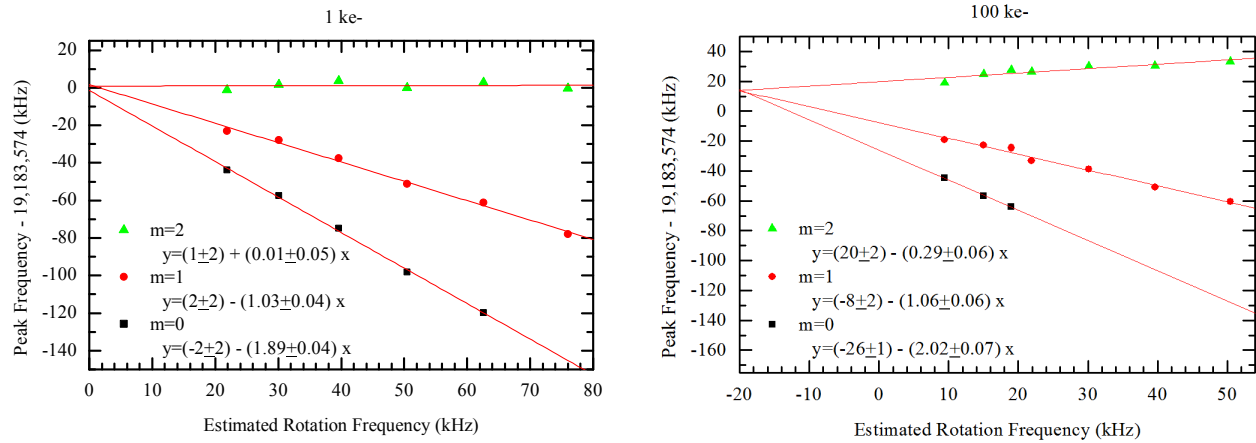


Figure 6.9: Linear fits to the $m = 0, 1, 2$ peak locations in the previous figure. $\delta \approx \text{slope}_{m=2}/\text{slope}_{m=1}$ is consistent with zero for $N = 10^3$ and about 0.3 for $N = 10^5$. The horizontal axis is the trapping field contribution to the rotation frequency $\omega_r \approx \omega_z^2/2\omega_c$. In the right panel, the $m = 0$ is approximated by the center of the flat region indicated in Fig. 6.8. Even this crude approximation is only possible for the first three traces.

6.4 ECR in ALPHA-g

The scheme for weighing antihydrogen in ALPHA-g is to slowly release it from a 1 T mirror + octupole (or “Ioffe Pritchard”) magnetic minimum trap and see whether more comes out the top or the bottom (see Fig. 6.10). Unlike ALPHA-1 and ALPHA-2, this trap will be vertical so that the mirrors can be tuned to cancel the gravitational potential of hydrogen as they are ramped down to 0 T. Thus if the ramp is perfect, antihydrogen atoms which gravitate the same way as hydrogen will escape the opening trap with equal probability up and down. Anomalous gravity would be detected as a deviation from 50% up, 50% down.

The greatest source of uncertainty in this measurement will be the magnetic field ramp. If $\mathbf{B}(r, z, t)$ were completely determined there would be no systematic error at the targeted $\delta m/m \approx 1\%$.

Using Hall probes, Nathan and others have begun to obtain field maps of the ALPHA-g solenoid. Nathan has also developed cryogenic NMR probes, made out of aluminum microparticles suspended in paraffin, which can monitor changes to the field at 10 Hz, which is probably better than what can be achieved using Reservoir ECR. This work is really

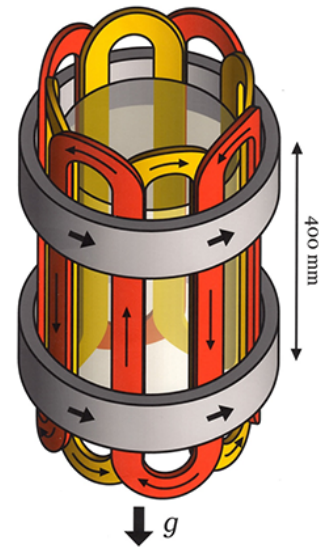


Figure 6.10: Chukman’s cartoon of the magnetic bottle in ALPHA-g. Will more antihydrogen come out the top than the bottom?

important for developing the detailed understanding of the solenoid which will be necessary to control it and effectively integrate the other magnets. There remain, however, some considerable technical challenges associated with the probes. For example, it is not obviously possible to accurately locate a 4 mm^3 NMR probe dangling from a 2000 mm rod into a cryogenic trap with energized magnets. ECR is currently considered to be the only option for a precision measurement. There are two reasons.

1. ECR could potentially be reporting the magnetic field while the antihydrogen is being released. A calibration with an NMR probe must be done at another time. It can be used to estimate what the field ought to be, assuming nothing has changed since the calibration. But even if the trapping structure were not altered significantly between calibrations, yet the field will be different every time a magnet is ramped because of superconducting hysteresis and activities in the zone.
2. 4 mm^3 is probably not small enough. Recall that the trap depth for a 1 T mirror is about 0.5 K, using $k_B T$ to represent energy. In contrast the change in potential energy mgh for antihydrogen in a $h = 1 \text{ m}$ trap is about 1.2 mK. An error of $1.2/500 \cdot 1\%$ or $2 \cdot 10^{-5} \text{ T}$ would spoil an attempted $\delta m/m \approx 1\%$ measurement. $2 \cdot 10^{-5} \text{ T}$ is ΔB for a z -range of only 0.3 mm at the center of a 1 T mirror coil with a 3 cm radius.

Granting that Reservoir ECR appears to be superior in some important aspects, it remains to be seen whether it is truly sufficient for the precision gravity measurement. The challenges are:

1. Time. The technique is currently able to produce one of the traces in Fig. 6.8 in about a minute. The total rampdown time in ALPHA-g will probably not be more than a few minutes and could be much less. One could measure ω_c 10 more times per minute by targeting a single peak and repetitively acquiring, say, 10 points in the vicinity of the peak. This requires a model of ω_c vs. time; these measurements would only allow for few-ppm corrections to a pre-calibrated ramp. It also requires that the microwave exposure to be short enough that the field doesn't change significantly during the exposure. If a Fourier-limited linewidth of 10 kHz is acceptable, one can use a $100 \mu\text{s}$ pulse, which covers only $10^{-4} \cdot 1 \text{ T}/60 = 2 \cdot 10^{-6} \text{ T}$, so this is no problem for a 1% measurement. Finally, recall that EVC is the time-limiting step in the reservoir sequence. There is potential for preparing pancake plasmas much faster using gradient-assisted EVC, discussed at the end of Chapter 7. This could allow for up to 100 B -field measurements during the rampdown.
2. Space. The minimum magnetic field will not be directly under an electrode, so it will be hard to make a deep well there. Because of the octupole, the minimum will be a few mm off-axis. Target plasmas might be moved off-axis by inducing a diocotron, perhaps using the patch potential method of Christensen [17]. The position of the minimum will have some time dependence, too. It seems that all these problems in

space can be studied offline. If $B(\mathbf{r}, t)$ were calibrated at the minimum and at some more convenient Point A, it would probably be sufficient to just measure $B(t)$ at Point A when the antihydrogen is escaping, provided Point A is reasonably close to the minimum.

Chapter 7

Distractions

Cavity cooling and magnetometry are the main results of this thesis. They were not the result of months or years of focused effort, but were more like old friends, occasionally left behind during rambles elsewhere. When a dead end occurred in the cavity cooling work, work could be done on microwave heating, or else on one of the projects described in this chapter.

Some of the topics introduced here warrant further development. The sections are organized in order of increasing usefulness: part of the first section (Ψ 's) really was a distraction, while the topic of the last section (Mirror-EVC) has an imminent application (improving reservoir ECR).

7.1 Stimulating Longitudinal Waves

It was important in Chapter 5 that the center of mass cyclotron mode normally couples much more strongly to the electromagnetic field than the $N - 1$ other modes. It is generally the dipole which rings the loudest. This is certainly true for the z -bounce motion, which, by coupling the plasma to electrode voltage noise, contributes to plasma heating. For the single particle heating rate Cluggish et al. derived the expression [18]

$$\frac{1}{T} \frac{dT}{dt} = \frac{\sqrt{2\pi}}{3} \omega \left(\frac{\delta L}{L} \right)^2 \sum_{l=1}^{\infty} \left(\frac{\omega}{l\omega_z} \right)^5 \exp \left[-\frac{\omega^2}{2(l\omega_z)^2} \right] \quad (7.1)$$

where ω is the drive frequency and δL is the amount the plasma is shortened by the applied perturbation. The response function should be roughly Gaussian with a Q of order unity.

While such single particle effects may well be happening at a lower level, the effect is negligible in comparison with heating due to collective axial modes, which are far narrower. In Fig. 7.1, $\Delta\omega \approx 2\pi \cdot 100$ kHz or $\omega/\Delta\omega \approx 300$. A value $Q > 100$ is also consistent with the number of post-excitation oscillations of the axial dipole mode when its frequency is measured with the plasma modes diagnostic (Section 7.2). This discrepancy is likely

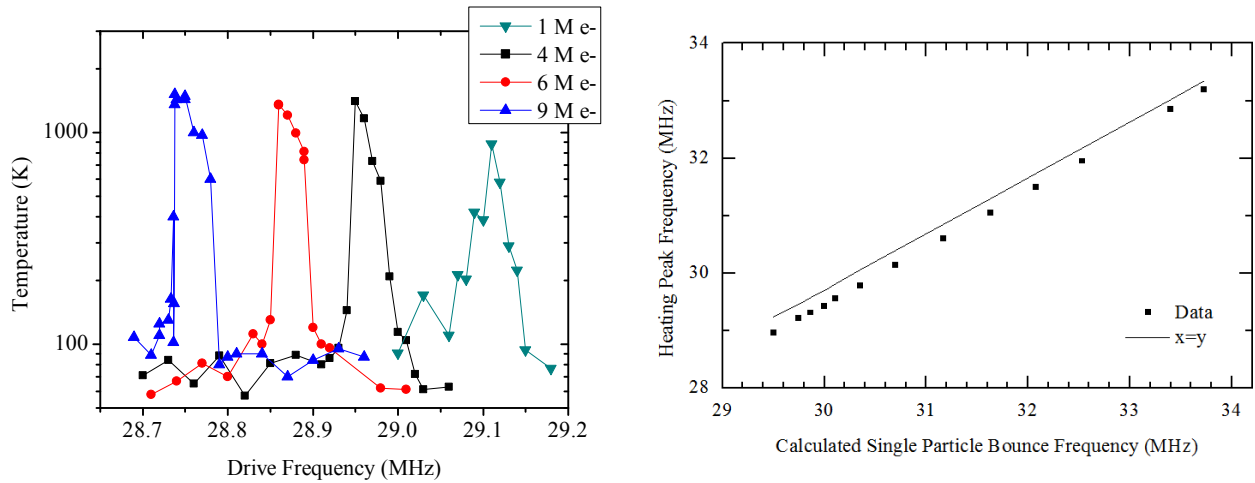


Figure 7.1: Bounce resonant heating of a few million electrons. Heating peak frequency is consistently downshifted relative to the bounce frequency calculated from the vacuum potential. The width of the $N = 1 \cdot 10^6$ line is probably limited by cycle-to-cycle reproducibility. Right panel uses $N = 3 \cdot 10^6$ and was obtained by undergraduates in 2014. While a small error in electrode amplifier calibration could also cause the observed downshift relative to the solid line, in magnitude it does appear consistent with the 200 kHz shift obtained by extrapolating from $3 \cdot 10^6$ to 0 electrons on the left panel.

due to the disappearance of Landau damping for the colder plasmas typical of the present experiment, compared to the $\mathcal{O}(1 \text{ eV})$ plasmas used to validate Eq. 7.1.

The data in Fig. 7.1 leads to the expectation that power in the electrode voltage FFT due to noise can add to expansion heating in limiting the minimum temperature $T_{min} = H/\Gamma$ for any noise peak near ω_z . This was mentioned in Chapter 2, where some of the dominant noise components in the FFT appeared (Fig. 2.7).

One can test the above hypothesis by looking at the minimum plasma temperature in a sequence of wells having ω_z near the CERNOX peak at $2\pi \cdot 30.5 \text{ MHz}$. The results are shown in Fig. 7.2. A more recent data set is shown on the right. This is one of the cavity-resonant cooling curves corresponding to the $83 \cdot 10^6$ electron point in Fig. 5.17 in Chapter 5. An interesting feature of this data is that the plasma seems relatively unaffected by the noise until it has cooled to 100 K. This suggests that a cold plasma mode is being driven to high amplitude before being converted to thermal energy.

The true source of the width in Fig. 7.1, if it is not collisions, is likely the anharmonicity in the on-axis potential. This would make the bounce frequency a function of amplitude. Under such conditions the oscillating plasma may phase-lock to the drive [34]. The oscillation amplitude self-corrects to keep ω_z close to the drive frequency. This could manifest itself in two ways in the experiment, which are discussed in the next two subsections.

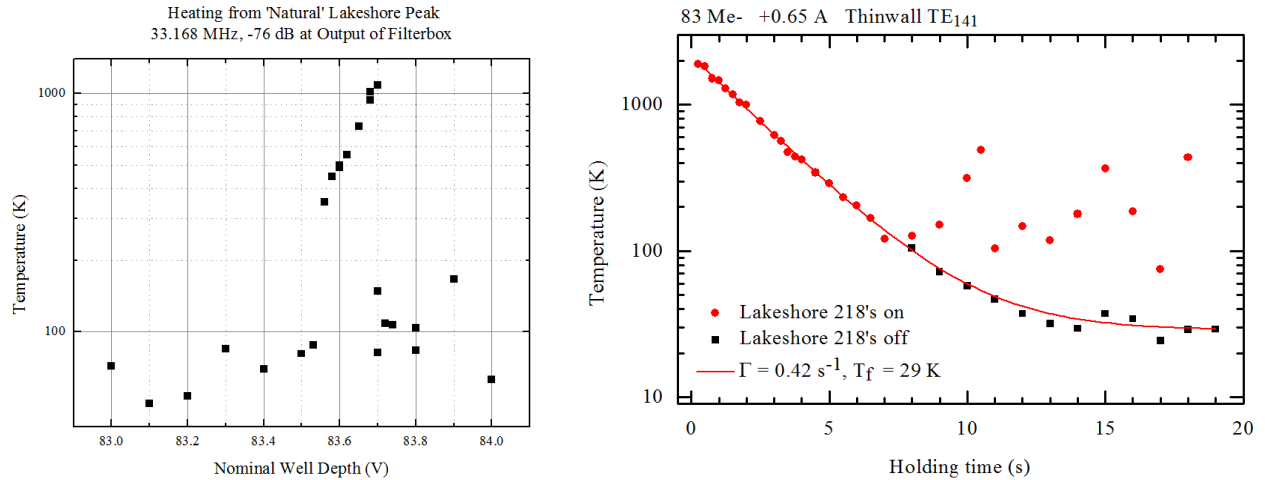


Figure 7.2: Plasma heating attributed electrode voltage noise. Lakeshore’s CERNOX controllers couple noise into the experiment which heats the plasma. The noise is much worse when the controller is on (cf. Fig. 2.7). For a few million electrons or less, heating is not severe unless the well depth is tuned to resonance with a noise peak (left). For achieving the lowest temperatures with $N > 10^7$ these controllers must be turned off (right).

Ψ 's

If the well is made gradually shallower, ω_z will slowly decrease and may come into resonance with a noise peak at ω . There is no doubt that the plasma is heated when $\omega_z \approx \omega$. What might happen in addition, as the well is made shallower, is that the amplitude of the dipole mode grows so as to maintain $\omega_z = \omega$ in the changing well. Possibly only a fraction of plasma particles in a narrow energy range are so trapped, forming a “phase space island” (Ψ).¹ Well shallowing is a natural part of every dump operation. If the plasma were to go through a resonance during Tdiag, a lump of charge would appear to arrive “early.” Such lumps are often observed when doing Tdiag in noisier parts of the trap. They may be produced intentionally using a fixed frequency drive during the dump. Small perturbations of the drive frequency upward result in earlier emission. The lumps or “ Ψ 's” can be made in both electron and positive ion plasmas. .

Chukman So’s Vlasov simulations suggest that the lumps are excited at the time of emission, thus they are not coherent long-lived objects after all. This interpretation agrees with the observation (Fig. 7.3) that an $8 \mu\text{s}$ pulse is sufficient to excite a Ψ . It still seems strange that one can drive at any frequency $\omega > \omega_z$, as long as it’s not too high, and induce emission—in Fig. 7.3 the drive frequency is the same for all pulses. But Chukman’s simulations also manifested this feature.

A similar phenomenon can occur well after the hottest particles from the Maxwellian

¹That would be a hot plasma phenomenon, whereas a coherent CM oscillation requires a cold plasma. The CM is not the only mode which can exhibit autoresonance; cf. [37]

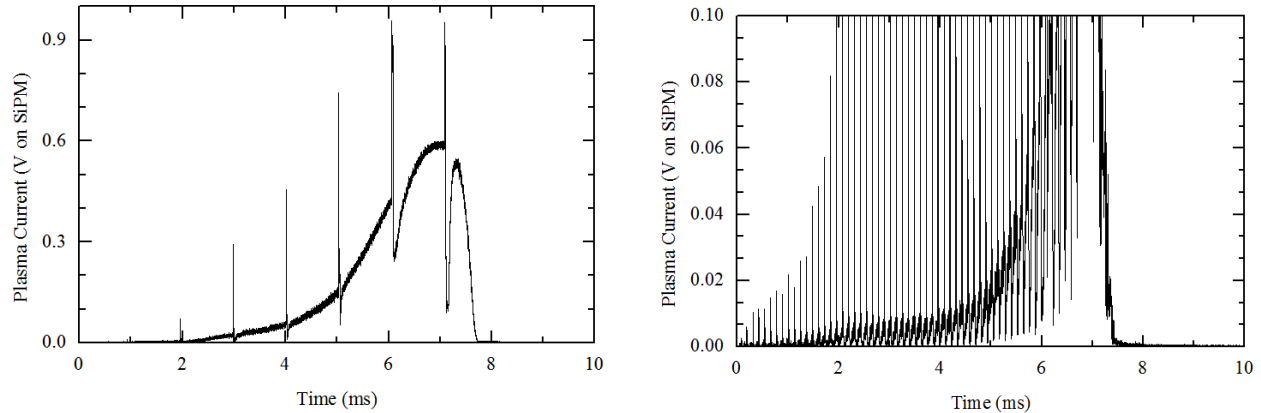


Figure 7.3: Induced noisy emission during temperature dump. Ψ 's are excited using a series of 10 MHz, 8 μ s pulses with low (left) and high (right) repetition rate. Plasma parameters are $N \approx 4 \cdot 10^6$, $T \sim 10,000$ K, $L \approx 3$ cm, $\lambda_D \approx 0.1$ cm. This means $v_z/2L \approx 7$ MHz, while for this well $\omega_z = 2\pi \cdot 7.5$ MHz.

have escaped². When the plasma is dense and cold ($N/T > 10^4$ e⁻ K⁻¹) the extraction trace often develops spikes just after rolling over into constant-current mode (see Fig. 7.4). This observations, along with the experiments done on positron plasma at UC Riverside [16], suggests that the mechanism described above must be part of the explanation. The diocotron and $\mathbf{E} \times \mathbf{B}$ contributions in Fig. 7.4 are distinct, having a different frequency domain signature than the spikes.

Nonmaxwellianizing the Distribution and Watching it Remaxwellianize

The alternative to fixing ω and sweeping ω_z is to leave the well shape constant and sweep ω upward. Single particles can be resonantly excited at $v_z/2L$, which is energy dependent. Thus by starting the drive at say $\omega = v_t/2L$ and sweeping the frequency up it is possible to selectively excite a subgroup of electrons to higher v_z , that is, higher energy. One can measure the perturbed distribution function with Tdiag, provided the plasma density is low and the temperature is high. This ensures that the dump (10 ms duration) is faster than the collision rate $\nu \approx 1000$ s⁻¹ (for $n = 10^8$ cm⁻³, $T = 1$ eV).

The manipulation of a selected portion of the distribution function of a hot plasma distinguishes this experiment from the autoresonant technique formerly used in the ALPHA-2 experiment to coherently excite the entire cold positron plasma during mixing. The present experiment has more in common with Will Bertsche's thesis work [13]. The two main differences are, first, in Bertsche's experiment the coherent object was a phase space *void*

²The orthodox view is that the latter 95% of the extraction is garbage. It is important to understand what one can about the plasma since so much is usually unmeasured and unknown.

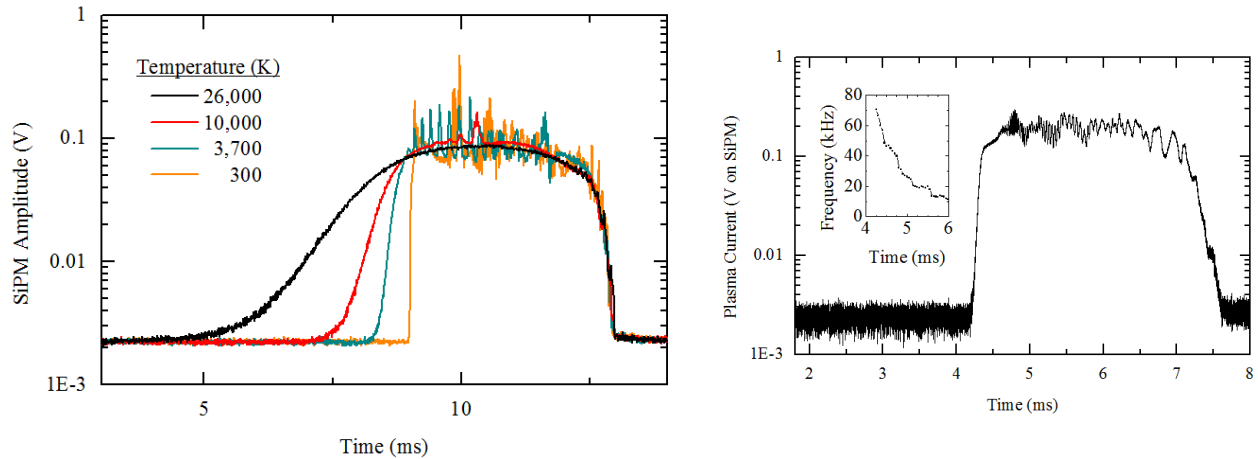


Figure 7.4: Full unsaturated extraction traces showing effects of electrode noise (left), plasma rotation and diocotron instability (right). Left side exhibits “noisy emission,” similar to that reported in Ref. [16], getting worse at lower T ($N = 43 \cdot 10^6$). Right side shows a clearly distinct effect: the frequencies of the perturbations start at reasonable values for the diocotron and $\mathbf{E} \times \mathbf{B}$ rotation, then gradually fall as the plasma becomes less dense. Inset plots peak of FFT using a rolling ROI of width ~ 0.1 ms (this is why it bottoms out around 10 kHz). It is hard to imagine what else this could be, if it is not the $\mathbf{E} \times \mathbf{B}$ rotation.

inserted into the bulk by sweeping the drive frequency *down*. Second, the parallel energy distribution is here directly characterized with Tdiag.

While non-Maxwellian distributions have been produced this way, in the interest of time a hybrid case of greater general interest is presented below. A slow dump is initiated on a cold plasma. While the well is getting shallower but before any plasma can escape,³ a chirped pulse (3 V, 1–11 MHz in 25 ms) is applied to the central electrode. This produces a beam of electrons at a relatively high energy (4 eV above the thermal distribution), but still confined by the well. The dump is paused for a variable hold time (0.03–1.50 s), and then completed to obtain the axial energy distribution. Fig. 7.5 includes some examples, along with a summary plot. The summary plot reports a manual estimate of how long it took, for each N , for the distance between the centers⁴ of the excited and bulk distributions to decrease by a factor of two.

The NRL Plasma Formulary [48] gives the relaxation rate for an energetic beam in a cold plasma as

³This is what makes it a hybrid case. Doing it this way produced a bigger, tighter beam than sweeping only one of ω or ω_z and holding the other fixed.

⁴The centers were found by first binning the data (number of samples above threshold divided by number of sample per bin) to produce plots like the left of Fig. 7.5, then fitting two Gaussians plus an offset with LabVIEW’s LevMar routine. The distance between the centers, plotted against log-time, formed an s-shaped curve. The middle of the s-curve is a manual estimate for the relaxation time.

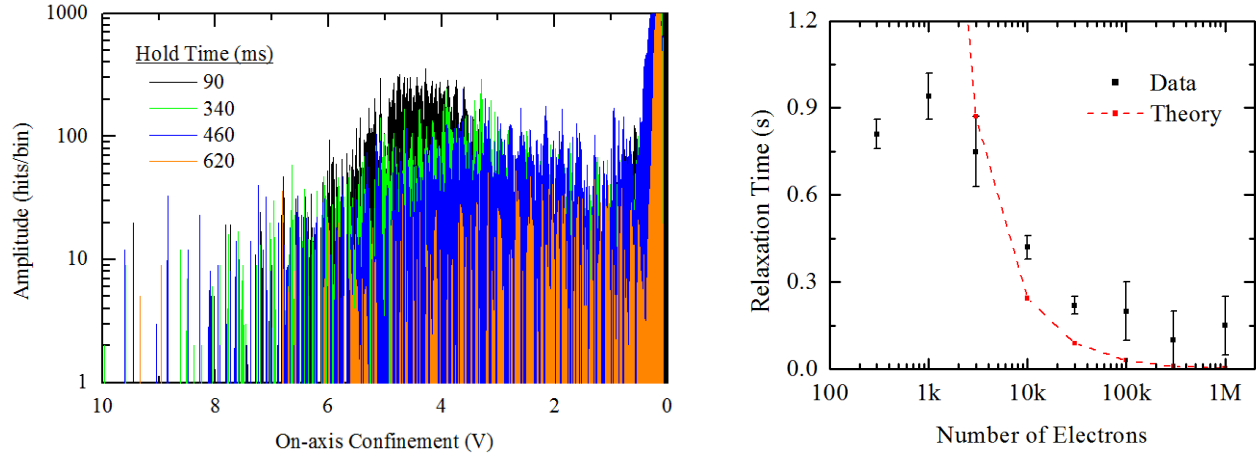


Figure 7.5: Relaxation of non-thermal electrons after being chirped to high energy. Sample traces (binned) are shown on the left for $N = 10^4$ electrons. Right panel plots approximate time for the center of the non-thermal fraction to move “halfway back to the right” (see text), as a function of total charge in the plasma. Dashed line is Eq. 7.2, using Peinetti’s solver (see Appendix C) for the plasma density, assuming $r_p = 1$ mm, $E_{beam} = 4$ eV, and $T = 1$ eV. The plasma length $L \approx 7$ cm is greater than λ_D for $N > 3 \cdot 10^3$ electrons.

$$\nu_\epsilon = 2 [\psi(E_{beam}/kT) - \psi'(E_{beam}/kT)] \left(\frac{e^2}{4\pi\epsilon_0} \right)^2 \frac{n \ln(\lambda_D/b)}{m^2 v_{beam}^3} \quad (7.2)$$

where $\psi(x) = (2/\sqrt{\pi}) \int_0^x dt t^{1/2} \exp(-t)$ and λ_D/b is the ratio of the Debye length to the distance of closest approach. This expression can be traced back to Chandrasekhar, who cautioned against using it for $E_{beam} > kT$. Using it for $E_{beam} > kT$, one obtains the prediction plotted as a dashed line on Fig. 7.5. This calculation uses a fixed beam energy $E_{beam} = 4$ eV. A more detailed calculation using a time dependent distribution for E_{beam} would reduce the theory estimates by up to a factor of two, due to faster thermalization for lower beam energy, and increase them by an unknown amount due to particles at higher energy which take even longer to thermalize.

Now that a preliminary data set has been analyzed, it is clear how to improve this experiment: more points between 10^3 and 10^5 electrons, more points for low holding time ($t < 1$ s, constant bulk temperature, dense targets from a reservoir, and image analysis to be sure that the radius is not varying in an unexpected way with the number of electrons. The two-Gaussian analysis can also be improved as the beam is not very Gaussian after the first e-folding.

Another interesting experiment along these lines would be to quickly evaporate the highest energy electrons of a hot plasma then restore the confinement and characterize the population of the tail. The non-magnetized theory for this already exists [61], but there may not be a clean experimental demonstration of those predictions.

7.2 Monitoring the Slosh and Breathing Modes

The plasma modes diagnostic was introduced by the Surko group [88] as a tool for continuously monitoring small changes in plasma aspect ratio and temperature. The implementation at Berkeley is nearly identical to the one described in Tim’s thesis [38], with a few improvements:

1. Amplifier noise. Here a homemade 100 MHz x10 preamp is followed by two x5 channels of the sr445a for a total gain of 250. The preamp is simply an el2125 op amp mounted in a non-inverting, $50\ \Omega$ impedance configuration on a PCB⁵. The el2125 amplifies with about half the noise of the SRS.
2. Blanking. The electrode high-pass lines are in principal independent, but with them all in the same filter box, there can be a lot of cross talk. Unless this is removed, the gain must be reduced to prevent overloading the sr445a. The pickup electrode signal passes through a zfswa-2-46 switch, gated off (60 dB isolation) during the drive pulse.
3. DAQ speed. The inherited version of the LabVIEW code had a buggy, deep hierarchy, some of which was intended to increase potential functionality. Code was gutted, kluged, and bypassed until the acquisition time went from something like 800 ms down to about 30 ms. This allows one to obtain the same information with a weaker drive at a higher repetition rate, or, if one is greedy, much more information and a more perturbed plasma.

These improvements were hoped to increase the sensitivity enough to track the quadrupole mode of significantly smaller plasmas. For reference, it is hard to get a signal at CERN with $N < 10^7$ electrons. It was occasionally possible to obtain a second-order peak at Berkeley for $N \sim 10^6$, but it was at the limit of sensitivity, and tended to drift to a lower frequency where it would soon disappear altogether. Although at least one successful scan was completed in an attempt to characterize the “accidental” cavity modes (see Fig. 5.26), the improvements described above were largely insufficient. It is possible that (a) a factor of 2 increased sensitivity is not good enough, (b) blanking is nice for the electronics but operation at high gain without blanking is probably possible, (c) the more rapid acquisition scheme is not really an improvement for stimulating and detecting the quadrupole mode (d) the quadrupole mode is not well defined for $N < 10^6$.

It is easier to stimulate and track the dipole mode (see Fig. 7.6). In the present setup it is not difficult to detect 10^6 electrons with the slosh drive. The resonant frequency of a plasma in a given well depends on the number of electrons. The trend in Fig. 7.7 is consistent with the trend in the heating peak vs. N experiment shown previously (Fig. 7.1). The slosh frequency goes down as N is increased: -40 or -75 kHz per 10^6 electrons for Figs. 7.1 and 7.7, respectively.

⁵The original SiPM board, with the SiPM bypassed and removed

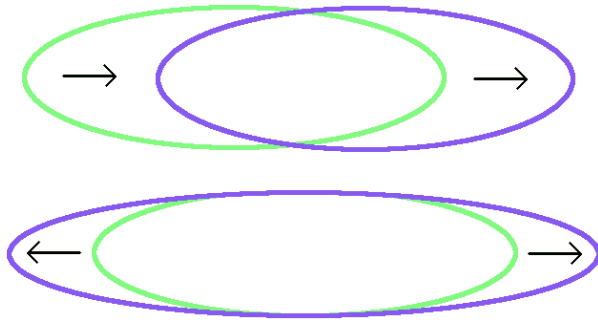


Figure 7.6: Cartoon comparing the dipole (slosh) and quadrupole (breathing) modes. The dipole (top) corresponds to a bulk displacement of the plasma center of mass, here depicted oscillating to the right. The quadrupole (bottom) is a compressional mode, here depicted during the expansion part of the cycle.

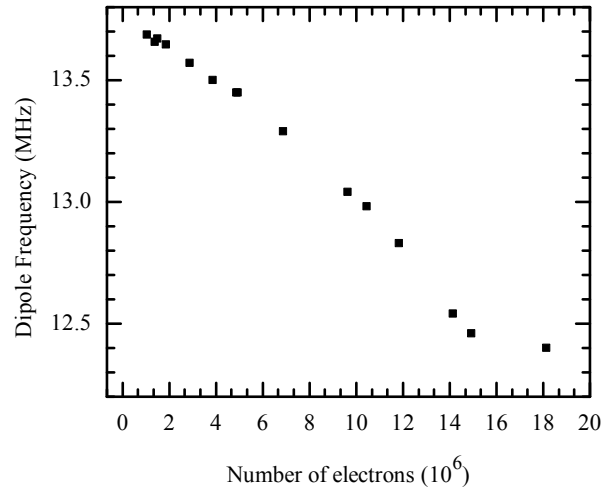


Figure 7.7: Observed correlation between dipole frequency and number of plasma electrons. After the frequency was determined using Modes.vi, the plasma was dumped to the MCP, which was simply used as a Faraday Cup (no HV bias).

Curiously, in 2010 Tim did a similar experiment and observed a trend in the other direction (elog:ALPHA/12098). These observations may be consistent with the accepted wisdom, that bounce frequency goes up as electrons gain energy [96], although this statement is normally intended to apply in the single particle regime. Tim’s data seems to match the simulated bounce frequencies for particles in an empty well but with kinetic energy equal to the space charge corresponding to each N .

This bounce-resonance data has not been modeled. The reader is reminded that to first order, all of the TG modes of a *cylindrical* plasma have the same dependence on aspect ratio and temperature, not just the quadrupole [78]. This fact may appear to contradict Dubin’s predictions for a spheroidal plasma (see Fig. 3 in [88]). These issues have been addressed in a followup paper from the Surko group [87]. Apparently the behavior observed depends on (A) whether the plasma is cold and dense enough that $\lambda_D \ll \lambda$, the wavelength of the plasma mode, and (B) the anharmonicity of the well. The electrostatic well used at CERN was “roughly harmonic” [38], presumably optimized to remove anharmonicity and make a clearer comparison with theory. The well shape was not carefully tuned in the various studies at Berkeley. Typical fourth order coefficients for these wells are around 10% of properly normalized second-order coefficients. Thus the data presented here likely represents the anharmonic regime, where plasma size and shape dependence would be expected for the slosh mode.

Before moving on to the next section, which happens to include another application of the modes diagnostic, the author pauses to honor the most important application of all:

fun.⁶ Collective modes are a big part of what makes plasmas more interesting than isolated particles, and it is fun to play with them. The plasma is like a living thing—one that has had enough of being born, held a little while in the dark to cool, then dumped. The operator can control the drive frequency with up and down arrow keys, or switch to drive amplitude, pulse length, &c. and the plasma will write its answer in the frequency domain. There’s also a neat swept harmonic structure which appears when the egun is on.

7.3 Resistive Cooling

The seminal work using a tank circuit to cool an electron cloud was done by Wineland and Dehmelt [96]. The cavity cooling experiments are basically an extension of this work to microwave frequency and the plasma regime. The latter introduces non-trivial complications which tend to be glossed over [92] or ignored [24, 47] by groups wishing to directly apply Wineland and Dehmelt’s methods to the cooling of a plasma.

The resonant circuit used for cooling axial motion must peak close to $\omega_z/2\pi \sim 50$ (1) MHz for electrons (ions). As described in Chapter 5 this sets an absolute thermodynamic limit on the cooling rate $\Gamma_z < \omega_z/NQ$. Because this is an axial cooling rate, the rate for cooling all three degrees of freedom is lower: $\Gamma \leq (1/3)\Gamma_z$. Thus, even for Q as low as 100, no more than $N \approx 10^6$ (10^5) electrons (ions) can be cooled at a total rate $\Gamma \approx 1 \text{ s}^{-1}$.

An attempt was made to demonstrate the dependence of Γ on N by incorporating an appropriate cryogenic tank circuit into the trap. The attempt ended in failure due to a neglected component (which does not always appear in the literature). This section reviews the calculations and observations made while optimizing and characterizing the LRC system.

An electron oscillating axially in the gap between two electrodes produces an “image charge current” between them. Shockley [82] used Green’s Reciprocity Theorem to show that the current is

$$I = q \frac{\mathbf{v} \cdot \mathbf{E}}{\phi} \quad (7.3)$$

where \mathbf{v} is the electron’s velocity, q is its charge, and \mathbf{E} is the field at the electron which would be produced by a potential difference ϕ applied across the electrodes. Since $|\mathbf{E}|/\phi = 1/2z_0$ if the electrodes are simply parallel capacitor plates separated by $2z_0$ it is standard to write this $I = qv_z\alpha/2z_0$. The correction factor α can be calculated by the electrostatic solver normally used to calculate trapping potentials.

If the electrodes are then connected with a resistor R , one might expect that the electron will lose energy at a rate $P = I^2R$, cooling as

$$\Gamma_z = \frac{P}{\frac{1}{2}mv_z^2} = \frac{q^2\alpha^2R}{2mz_0^2}. \quad (7.4)$$

⁶<https://drive.google.com/file/d/0B-QIxm3kY7CJbnFTRHNySUE5MFU/view?usp=sharing>

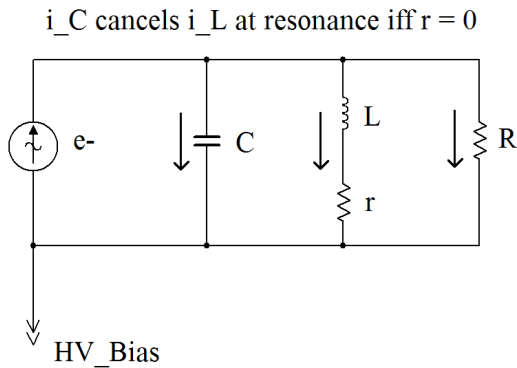


Figure 7.8: Schematic of the LRC circuit. The electron is represented as an ideal source of (image charge) current. As Shockley put it, “the net current is found by adding the currents induced by the moving charge...and the currents due to the changing voltages [on the conductors].”

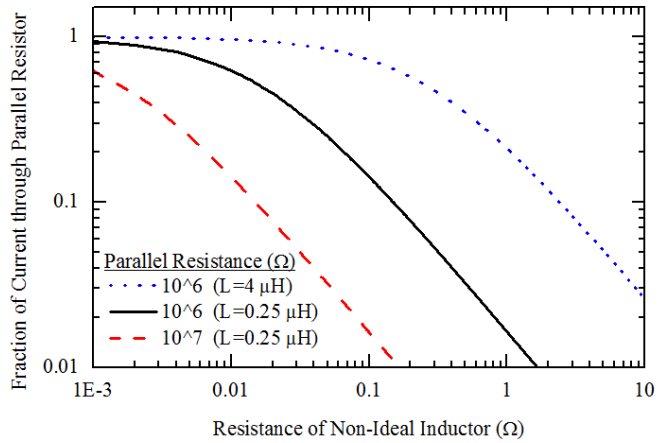


Figure 7.9: Calculated fraction of current which flows through the parallel resistor, for typical values of R and L . To about 1%, the curves shown are independent of $\pm 50\%$ variation in C and ω_z for $r < 1 \Omega$. The plotted function should enter Eq. 7.4 as a correction factor. This is not mentioned in any of the reviews, tutorials, or articles cited here, but Ulmer alludes to it in [89].

This is the usual result given, and it is quite wrong unless one has jumped through a number of additional hoops, some of which are not mentioned in the standard references [14, 35, 47, 55, 56, 92, 96]

To begin with, Shockley’s image charge result assumes a low impedance current path between the electrodes. No matter how small the induced image charge q' “ought” to be, $I = \omega_z q' \rightarrow \infty$ as $\omega_z \rightarrow \infty$ so a high frequency image charge oscillation requires a high voltage source ($V = IR$). The electron is not a high voltage source. Approximating the maximum output voltage by the electron’s kinetic energy, one obtains a practical limit of $R \sim 10^8 \Omega$ for cooling a single electron to 10 K.

Another problem is that at 50 MHz the capacitance of the electrode is going to short out V ($|X_C| \sim 100 \Omega$ for $C \sim 10$ pF). The solution to this problem is to add an inductor. Fig. 7.8 shows a schematic of the usual tank circuit employed, having a resonant frequency $1/\sqrt{LC} \approx \omega_z$.

At resonance, all the image charge current flows through R , and one obtains Eq. 7.4—only if L and C are perfect. If $r \neq 0$ one can show using Kirchoff’s Laws that the fraction of current from the electron which actually goes through R is

$$\left| \frac{I_R}{I} \right| = \left| 1 + \frac{j\omega r C}{j\omega \frac{L}{R} + \frac{r}{R}} \right|^{-1} \tag{7.5}$$

This equation is plotted in Fig. 7.9. There is a premium on producing an inductor with

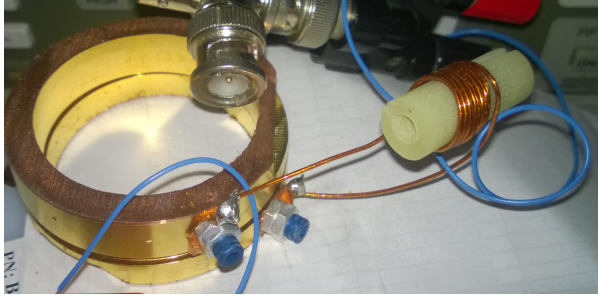


Figure 7.10: Test rig used to produce Fig. 7.11, shown with the actual inductor and dummy half-inch electrodes. The G-10 form was removed prior to attachment to the electrode stack (see Fig. 2.1).

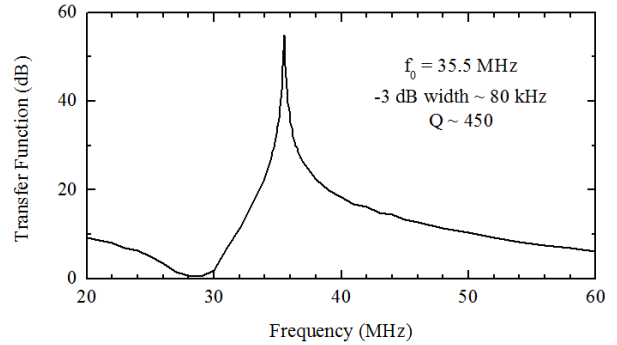


Figure 7.11: Transfer function of the mock-up tank circuit, measured using the modes PXI crate. Drive and pickup “coils” are the blue wires coupling to the Accuglass-wire inductor in Fig. 7.10.

L (μH)	r at 30 MHz and 10 K (Ω)	C (pF)	Q	z_0 (cm)	α	$\Gamma_z^{(\text{uncorrected})}$ (s^{-1})
0.25	0.3	120	150	1.25	0.028	0.5

Table 7.1: Estimated LRC circuit parameters for resistive cooling. L , r , and Q are calculated from wire and inductor dimensions (22 awg), then C is derived from the *in situ* resonant frequency measured with Modes.vi. Calculated Q agrees with the Modes.vi result (Fig. 7.12). Γ_z is given prior to the correction factor, Eq. 7.5.

very low series resistance r . That resistance is much larger at high frequency than at DC because of the skin effect. The residual resistivity and magnetoresistance (Section 2.3) must also be considered in this connection: the copper is sitting at 10 K in a 1 T background field. Thicker wire with higher RRR is still better, despite the reduced skin depth. Another consideration is the parasitic capacitance between turns. This is thought to be marginal provided the turn spacing is at least twice the radius of the conducting part of the wire [93]. These considerations⁷ led to the design of the inductor shown in Fig. 7.10. Fig. 7.11 shows the results of the bench test.

Figure 7.9 explains what actually limits R in most cases. Choosing R too high leads to less current through the parallel resistor and can reduce the cooling rate. In the present case the cooling rate was drastically reduced because it was naïvely assumed, looking at Eq. 7.4, that arbitrarily high R was optimal, and the resistor was simply omitted.

⁷In fact, the current-fraction problem described above was not realized until much later (see below). The series resistance r was still minimized, but for a different reason. According to Ref. [24], one can simply multiply Eq. 7.4 by the ratio of quality factors $Q_{ser}/Q_{par} = (L/r)/RC$ in the case $Q_{ser} < Q_{par}$ because r behaves as if it were a parallel resistance $R_{par} = rQ^2$. This gives a cooling rate proportional to $1/r$.

Using the values given in Table 7.1, combined with the current fraction from Fig. 7.9, one can estimate $\Gamma_z < 0.01 \text{ s}^{-1}$. Such a low cooling rate is well below the detection threshold. It was not possible to detect the LRC circuit by measuring the temperature of plasmas brought into resonance with it. At that time the thorough analysis and literature search presented here was not complete, so the lack of resonant cooling was a surprise. In order to better understand the problem, a different measurement was proposed. Using the plasma modes diagnostic, the amplitude and frequency of the plasma’s dipole mode was monitored while the well depth was gradually decreased such that the dipole frequency would scan through the LRC resonant frequency. Figure 7.12 displays the result for two different plasmas. This seems to confirm the presence of a resonator of about the right Q value, able to absorb energy at about the right frequency.

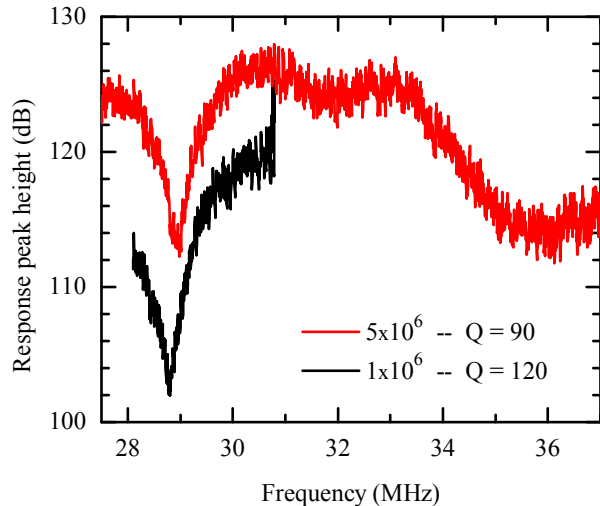


Figure 7.12: Finding the LRC resonance with Modes.vi: bounce frequency of the well is swept while tracking the dipole mode of a 5 or $1 \cdot 10^6 \text{ e}^-$ plasma.

7.4 Mirror EVC

The goal of the experiment built at Berkeley, forming the thesis work of at least two graduate students and one masters student, was to use cavity cooling to produce cryogenic electron plasmas. The original expectation was that once cavity cooling had been demonstrated and understood for electrons, a cavity would be made to go into ALPHA-2 to cool positrons and increase the antihydrogen trapping rate. Simultaneous with this research, SDREVC was developed at CERN, enabling a finely tuned antiproton-positron mixing step with active antiproton cooling provided by positron EVC. This is a very effective mixing scheme and it makes cavity cooling obsolete. It is natural now to ask whether anything in this thesis will ultimately contribute to the original goal.

In 2017 an amusing and previously unknown effect was observed. In the original reservoir sequences at CERN, target plasmas were evaporatively cooled in the strong gradient of a mirror coil in the neutral trap. It was found that the EVC duration could be reduced to 10 ms with no adverse effect—but only with the trapping magnets on. Without the strong gradient the minimum usable time was 100 if not 200 ms. It appeared that electrons could be evaporatively cooled over an order of magnitude faster with the mirror field on (“NT”) vs. off (“no NT”). See Table 7.2.

Due to other priorities, there was not an opportunity to properly study the apparent effect. ALPHA is a big collaboration which is known for refusing to waste machine time on

		N (10^3)	r_p (mm)	T (K)
No EVC	NT	92 ± 4	2.10 ± 0.05	
	no NT	93 ± 5	1.90 ± 0.04	
10 ms EVC	NT	12.8 ± 0.6	3.50 ± 0.07	150 ± 50
	no NT	4.5 ± 0.6	4 ± 1	600 ± 50
100 ms EVC	no NT			100 ± 10

Table 7.2: Measured target plasma parameters suggesting a Mirror-EVC effect. “NT” refers to the mirror and octupole magnets used in the “neutral trap,” which could be ramped up after the reservoir plasma was prepared in the purely solenoidal field. Target plasma length is about 1 cm at the end of the EVC step. The gradient under the mirror coil is 0.16 T cm^{-1} in that location with the neutral trap on and less than 0.0001 T cm^{-1} otherwise.

plasma physics discoveries that don’t substantially affect the antihydrogen program. Further study of the phenomenon has been postponed indefinitely. This is a little unfortunate because the positron-EVC during mixing with antiprotons appears to be executed in the “wrong” direction: up a steep gradient rather than down (cf. Fig. 7.13). The present observations suggest that evaporating the other way could affect the number of trappable antiatoms produced.

A related experiment was later performed at Berkeley using the copper gradient coil. The theoretical work of Fajans [33] seemed to suggest that the mirror ratio needs to approach unity in order to see a significant effect.⁸ The gradient coil is nominally limited to a field of about 10 mT. Plasmas at fields as low as 30 mT could be trapped and apparently diagnosed with Tdiag, although significant aperturing observed with the camera below 60 mT may compromise the result. The plasma was made as long as possible, so that while being evaporatively cooled it should cover over 50% of the change in field associated with the gradient. EVC was optimized at 0.03 T with no current in the gradient coil, and then the resulting temperature for different current values was measured, in both polarities. The result, shown in Fig. 7.14, provides further support for the hypothesis that evaporative cooling down a gradient is more effective than the alternatives.

A single-particle model will be sketched here to potentially explain the observations at CERN and at Berkeley. Denote the side of the plasma where the potential is highest Side A, and the side from which particles escape Side B (see Fig. 7.13).

Normally during EVC, particles with the most axial energy escape, and the rest of the distribution rethermalizes with a lower-average-energy via collisions. For simplicity, consider this a two-step process. First the axial population relaxes, then the transverse population

⁸Fajans’ work guided the early approach to the problem, but a single-particle explanation will be presented in what follows. Fajans’ work is a warning against ignoring plasma effects, which might have been less important for the small target plasmas and very long low-field plasma reported here. The requirement that the mirror ratio be large is valid in any case.

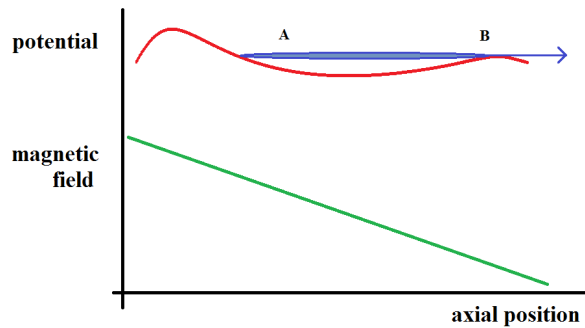


Figure 7.13: Cartoon of a positron plasma being evaporatively cooled under a magnetic field gradient. Particles escape on the low-confinement side, labeled B, where the magnetic field is also lower than at A. In traveling from high (A) to low (B) field, cyclotron energy is transferred to parallel energy, which helps “hot-transverse” particles to escape.

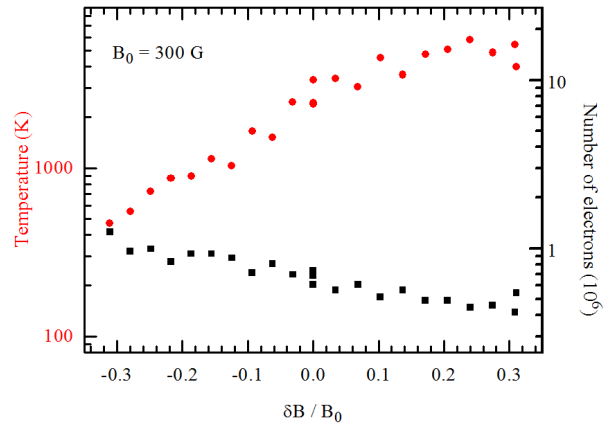


Figure 7.14: Low field demonstration that EVC works better using a gradient. The horizontal axis gives the difference in field at the escape point “B” relative to “A,” normalized to the background field B_0 . $\delta B/B_0 < 0$ corresponds to the “downhill” configuration portrayed in Fig. 7.13.

thermalizes with the lower axial temperature at the rate $\nu_{\perp\parallel}$ [53]. The distribution must be clipped and rethermalized many times for the EVC to be efficient. Supposing it takes $\mathcal{O}(10)$ times, $\nu_{\perp\parallel}$ could limit the maximum ramp-rate to $\mathcal{O}(\nu_{\perp\parallel}/10)$.⁹

With a gradient, it might not be necessary to wait for collisional equilibration of the perpendicular and parallel energy distributions to obtain good cooling. Suppose that the magnetic field is stronger at point A than at point B. By the conservation of magnetic moment $\Phi_m = (\frac{1}{2}mv_{\perp}^2)/B$, particles going from A to B will lose transverse energy, transferring it into axial kinetic energy.¹⁰ Thus, the hottest part of the transverse energy distribution at A will be preferentially evaporated at B.

If instead the field is stronger at B than at A, transverse energy will not be efficiently removed. In fact one should expect the opposite: particles will lose axial energy while approaching the escape point and arrive with insufficient energy to escape. Particles with low transverse energy will be preferentially evaporated (that’s bad), because the axial energy loss in the mirror field is proportional to Φ_m .

In both cases the steep gradient is mixing perpendicular and parallel energy, perhaps irreversibly once collisions are properly accounted for. Nevertheless, the arguments given above suggest that, compared to no gradient and uphill gradient, EVC in a downhill gradient

⁹An alternative explanation could be that this is the time required for the plasma core to be repopulated by collisions or, if enough of the core is removed, by the diocotron instability.

¹⁰Fajans’ theory suggests that this would not happen in the interior of the plasma, where the total potential should be constant if the plasma is in thermal equilibrium.

should still be the fastest option, because it directly cools two degrees of freedom rather than one, and because it doesn't produce the hurtful bias described in the previous paragraph.

It is not obvious from the preceding discussion that a downhill gradient should improve the antihydrogen production rate during positron-antiproton mixing. It may even be better the way it is (stronger field at the antiprotons) because positrons with higher transverse energy are prevented from reaching the antiprotons.

Reservoir ECR could benefit from faster EVC. High precision in an axially varying magnetic field requires the shortest, therefore coldest, possible target plasmas. It is therefore necessary to EVC the target plasmas. EVC is therefore the time-limiting step in high precision Reservoir ECR. With the 500 ms EVC step currently employed to achieve minimum temperature, ECR is barely viable as a diagnostic during the $\mathcal{O}(10^2)$ s mirror rampdown foreseen for ALPHA-g. A 10 ms EVC step under the gradient, prior to moving the target to the short well, might enable one to take T vs. f data at a rate exceeding 1000 points per minute. That's enough for 100 peak detections during a one-minute rampdown, provided one can estimate the peak locations to within about $1/Q$ in advance—either feeding back on the previous peak locations, or using a table acquired prior to running the experiment with antihydrogen.

Another possible application, suggested by the Chair, is SDREVC for antiprotons. With the coming ELENA upgrade [65] it may be possible to obtain cold antiproton plasmas with over ten million particles. For these to be compressed by the rotating wall in the strong drive regime [15, 20] will require good cooling, possibly better than can be achieved with EVC in the absence of a strong gradient. It should be noted, in this connection, that plasmas produced using SDREVC by Carruth et al. [4] did not appear to be affected by the presence of a modest gradient field ($\delta B/B_0 < 1/10$).

Appendix A

LabVIEW VI's

It would be hard to run the experiment without these VI's. Many were thrown together in a few hours when the need arose and have evolved continuously for years. Here is a link to a Google Drive folder with many of these VI's in it (not necessarily the most recent versions):

<https://drive.google.com/drive/folders/0B-QIxm3kY7CJfI9IZ0JINnZTUVVqWFNNM1NIZlJsNHZPV3Y5aGRJb1BGUmozamZHMEdzOG8?usp=sharing>

Name	PC	LV Version	Purpose
Sequencer 3.0.1	envmon	13	electrode voltages and triggers
Egun Control	envmon	11	Marcelo's egun control box
Lakeshore Reader	envmon	13	CERNOX temperature logger
Lakeshore 625	envmon	11	solenoid power
Kepeco Flapper Control	pbar	14	MCP and coil
RW Project	pbar	14	rotating wall
Potential Analysis	pbar	14	analyze on-axis potential profiles
CeRes Faraday Cup	pxi2	13	DAQ, control and log parameters (synth freq., coil current, etc.)
Netty Anne	pxi2	12	test electrode connections
Modes	pxi2	12	plasma modes diagnostic
Camera Control Main	vulcan	13	camera DAQ
Bakery 2014	vulcan	13	bakeout
Analysis Queue Control	gluino	14	image analysis
TemperatureFit Final 2016	gluino	14	Tdiag
TNBthzoff Analysis	gluino	14	collate and filter data, plot in 3D
Poisson	broken	14	Fede's plasma solver

Appendix B

Historical Penning-Malmberg Trap Experiments

Close to equilibrium, a typical plasma in a Penning Malmberg trap is rotating in three different ways (Table B.1). Each class of collective motion corresponds, at low density and high temperature, to a single particle motion of similar frequency. If one adds to these modes the collisional timescale ν^{-1} a fairly complete list of the kind of perturbations which can couple strongly to the plasma is obtained. Each kind has proven fruitful, either for applications or basic plasma research, resulting in experiments which could not have been done in any other machine.

The Diocotron Mode

This is the macroscopic, low frequency orbital motion of the plasma column about the trap center. Despite being a negative energy mode, it is often stable enough to be treated as an adiabatic invariant, permitting a well-controlled demonstration of adiabatic invariant breaking [68]. Multiple charge columns may coexist stably, pulling each other the same as a 2-D array of point vortices, via the one-to-one analogy electron density \rightarrow vorticity, space charge \rightarrow stream function. This idea along with a photocathode plasma source permitted

Plasma Mode	Single Particle Motion	Typical Value
Diocotron	Diocotron	1 kHz
Bulk Rotation	Magnetron	100 kHz
Trivelpiece Gould	Axial Dipole	10 MHz
Cyclotron	Modified Cyclotron	10 GHz

Table B.1: Normal modes of a pure electron plasma

stability studies of arbitrary 2-D vortex patterns [28]. In 2018 the adiabatic invariant was resurrected in aid of a patch potential study [17], and there is talk of exciting a small diocotron for extending the ECR measurement to $r > 1$ mm.

Rotating Wall

Infinite lifetime was achieved shortly before the millenium [8] by this technique, which immerses the plasma in a swiftly spinning electric dipole field. Weak fields couple via a surface plasma wave, pinning the plasma density to resonance with the applied rotation frequency ω_{RW} (the Trivelpiece-Gould wave frequency $\omega_{TG} \propto n$. If n decreases, $\omega_{RW} > \omega_{TG}$ and the field produces a positive torque, restoring higher n). It was later found that the same feedback mechanism works at *any* frequency if the field is strong enough [20]. Thus, n may be chosen by fixing $\omega_{RW} = \omega_r \approx ne/2\epsilon_0 B$ (here the drive couples to the bulk rotation ω_r , apparently a single particle effect). In 2017 this technique was combined with the evaporative cooling process to simultaneously fix n and ϕ_0 , which at $T = 0$ defines a single plasma equilibrium, as described in Chapter 4 and in Celeste's thesis [15].

Collisions and Shielding

Collisions are of course what makes the rotating wall necessary. A pure electron plasma may be cooled, without risk of recombination, down to the strongly magnetized regime where the cyclotron radius $r_c \lesssim b = e/k_B T$. Here the collisional equipartition rate $\nu_{\perp\parallel}$ drops exponentially as the cyclotron motion, which carries the energy in T_{\perp} , becomes an adiabatic invariant during electron-electron collisions [12]. In fact the Penning-Malmberg trap boasts the first measurement of $\nu_{\perp\parallel}$ in any regime [53], and since the advent of laser-cooled Mg^+ plasmas and spin tagging, increasingly sophisticated transport studies have been carried out to reveal thermal, particle, and viscous diffusion much higher than predicted by classical collision theory [9, 46, 58].

Careful study in a Penning Malmberg trap has also shown that plasma shielding is rather more interesting than the equilibrium Debye model normally taught in plasma theory courses. Plasmas may shield without collisions via dynamically trapped particles and even antishield, depending on how the perturbation is created [44].

Appendix C

Electrode Potential Solver

A MATLAB based Poisson-Boltzmann solver, written by Federico Peinetti [73], is used in this thesis to calculate the plasma length, density, and space charge. The solver takes the measured plasma radius and temperature as inputs.

Federico's solver has proven extremely valuable for this thesis work. It does have some limitations though. For example, one cannot specify the number of electrons N at the input. Instead one must guess the density n , and try again if the wrong N comes out. The guess-and-check routine has been automated in LabVIEW.

A more severe limitation is that the solver assumes five cylindrical electrodes with one constant radius. This is not a good model for the trap. This section describes a method for approximating the COMSOL profiles using five electrodes of the same radius. It begins by reviewing an analytical model for the five-electrode case. This model is implemented in LabVIEW. Another LabVIEW code then uses the Lev-Mar routine to control the five-electrode lengths and potentials, minimizing the distance between the resulting on-axis potential profile and the one calculated in COMSOL for the actual trap.

The first task is to calculate the potential. Begin with Laplace's equation.

$$[\partial_r^2 + \frac{1}{r}\partial_r + \partial_z^2] \phi = 0 \quad (\text{C.1})$$

Assume ϕ is separable i.e. $\phi(r, z) = f(r)g(z)$. If such a solution is found it must be correct, as Laplace's equation has only one solution for a given geometry (boundary conditions). Separability implies

$$[\partial_r^2 + \frac{1}{r}\partial_r + \kappa^2] f(r) = 0 \implies f(r) = J_0(\kappa r) \quad (\text{C.2})$$

$$[\partial_z^2 - \kappa^2] g(z) = 0 \implies g(z) = e^{\pm\kappa z} \quad (\text{C.3})$$

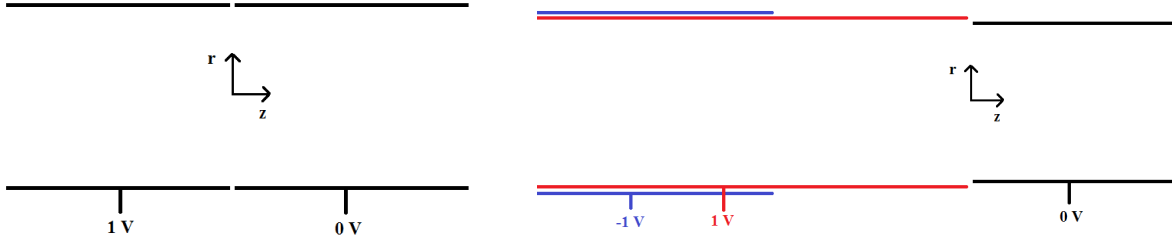


Figure C.1: Illustration of the procedure for calculating potentials due to finite length electrodes. Left: Two electrodes assumed to extend to infinity to left and right. Origin of r and z is shown. Right: If the 1 V electrode was actually finite, it can be represented as a superposition of two infinitely long electrodes at 1 V and -1 V, the latter having a z offset equal to the finite electrode length.

$\phi_\kappa(r, z) = J_0(\kappa r)e^{\pm\kappa z}$ solves Eq. C.1¹ for any constant κ , so one can combine solutions as $\phi = \sum c_\kappa \phi_\kappa$ to satisfy the boundary conditions imposed by the metal electrodes (see Fig. C.1). The conditions are

- i For $r = R$, the trap radius, $\phi = 1$ V if $z < 0$ and 0 V if $z > 0$.
- ii For $r < R$, $\phi = 1$ V for $z \rightarrow -\infty$ and 0 V for $z \rightarrow \infty$.
- iii For $r < R$ and $z = 0$, $\phi = 0.5$ V.

A piecewise solution can satisfy these conditions. For $z < 0$, $\phi = 1$ V plus positive exponential terms, while for $z > 0$, ϕ contains only negative exponential terms. κ is determined by (i): $J_0(\kappa R) = 0 \implies \kappa = \alpha_k/R$ where α_k is the k^{th} root of J_0 . The coefficients c_k are determined by (iii):

$$\begin{aligned} \sum_{k=1}^{\infty} c_k J_0(\alpha_k \frac{r}{R}) &= 0.5 \text{ V} \\ \int dr r J_0(\alpha_m \frac{r}{R}) \sum_{k=1}^{\infty} c_k J_0(\alpha_k \frac{r}{R}) &= \int dr r J_0(\alpha_m \frac{r}{R}) \cdot 0.5 \text{ V} \\ c_m \frac{R^2}{2} J_1^2(\alpha_m) &= \frac{R^2}{\alpha_m} J_1(j_0 m) \cdot 0.5 \text{ V} \\ c_m &= \frac{1 \text{ V}}{\alpha_m J_1(\alpha_m)} \end{aligned}$$

where a couple J_0 identities (orthogonality ID, derivative ID) are used to go from line two

¹ $Y_0(\kappa r)$ also solves the radial equation, but it diverges logarithmically as $r \rightarrow 0$, so this term does not contribute to a solution with $r = 0$ in its domain.

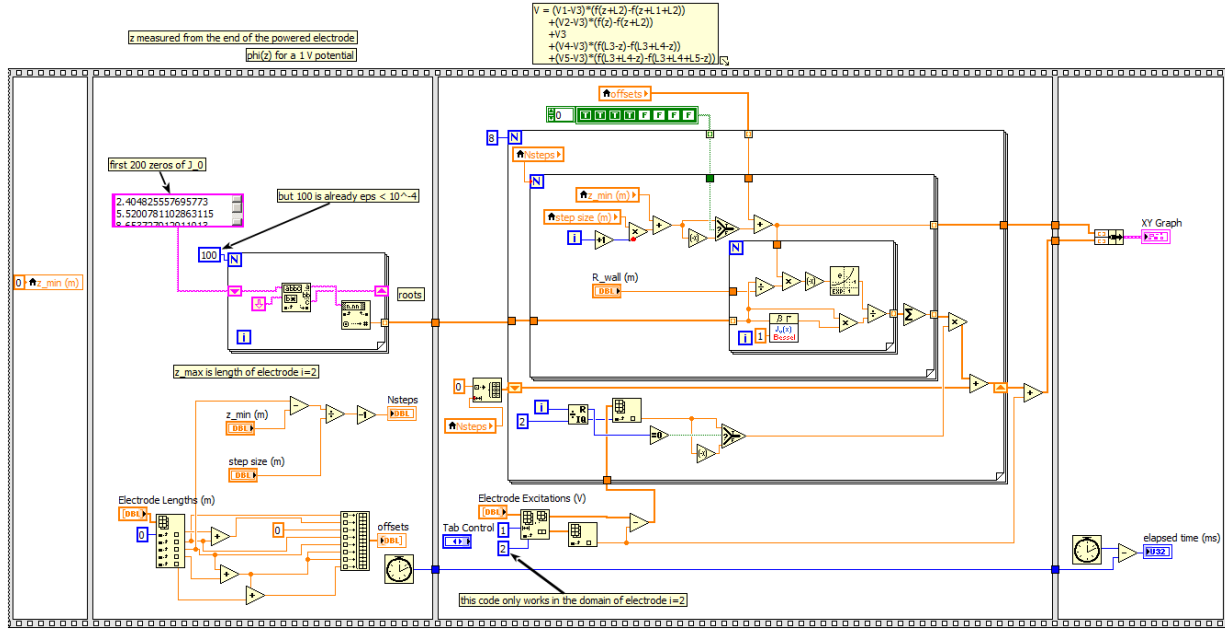


Figure C.2: The block diagram of the VI which generates the on-axis potential, $V(z)$, at 300 points per second with better than 10^{-4} precision.

to line three. Thus,

$$\phi(r, z) = 1 \text{ V} \cdot \sum_{k=1}^{\infty} \frac{J_0(\alpha_k \frac{r}{R})}{\alpha_k J_1(\alpha_k)} \begin{cases} -e^{\alpha_k \frac{z}{R}} & z < 0 \\ e^{-\alpha_k \frac{z}{R}} & z > 0 \end{cases} \quad (\text{C.4})$$

plus a constant 1 V for $z < 0$. This solution can be extended to the case of arbitrarily many electrodes via scaling and superposition: within the domain of a powered electrode, one must add the scaled constant. Outside an electrode's domain one can treat it as infinite in the other direction. The basic idea is illustrated in the right side of Fig. C.1. The exact algorithm is

$$V(z) = (V_1 - V_3) * (f(z + L_2) - f(z + L_1 + L_2)) \quad (\text{C.5})$$

$$+ (V_2 - V_3) * (f(z) - f(z + L_2)) \quad (\text{C.6})$$

$$+ V_3 \quad (\text{C.7})$$

$$+ (V_4 - V_3) * (f(L_3 - z) - f(L_3 + L_4 - z)) \quad (\text{C.8})$$

$$+ (V_5 - V_3) * (f(L_3 + L_4 - z) - f(L_3 + L_4 + L_5 - z)) \quad (\text{C.9})$$

where L_i and V_i are the applied voltage and length for the i^{th} electrode and $f(z) = \phi(r=0, z>0)$ from Eq. C.4. This algorithm is only valid in the domain of electrode 3, that is for $0 < z < L_3$. The LabVIEW code is displayed in Fig. C.2.

This code was streamlined in order to be used efficiently by LabVIEW's LevMar routine. For a given electrode configuration, LevMar is asked to match the 5-electrode potential to

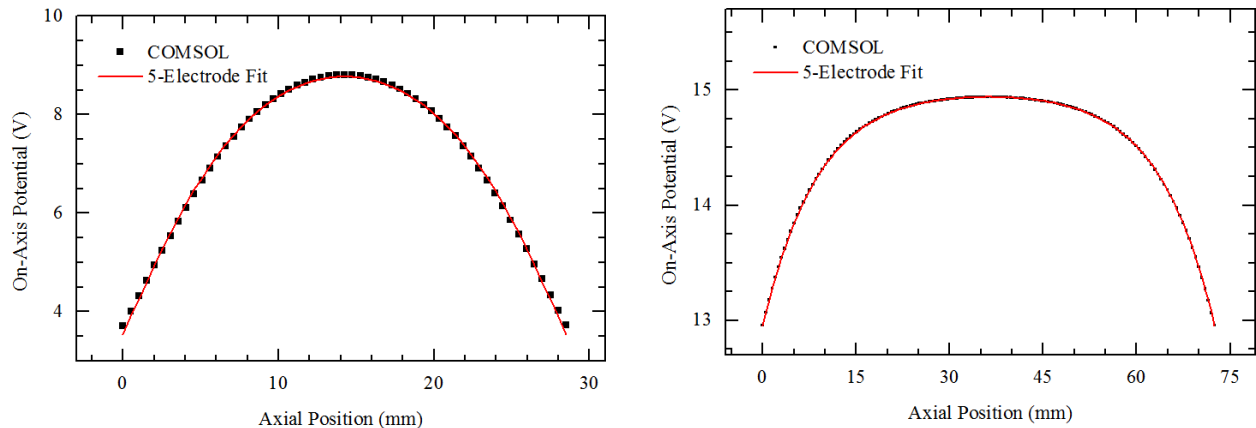


Figure C.3: LevMar fits using 5 flat electrodes to model Cavities 1 (left) and 2 (right). Parameters for the fit on the left are $r_w = 12$ mm, $L_i = \{50, 50, 28.5, 50, 50\}$ mm, $V_i = \{-50.95, -3.11, 9.89, -3.11, -50.95\}$ V. Parameters for the fit on the right are $r_w = 20$ mm, $L_i = \{100, 31.3, 72.5, 31.3, 100\}$ mm, $V_i = \{-80.93, 14.44, 15.00, 14.44, -80.93\}$ V.

the part of the COMSOL-predicted on-axis potential seen by the plasma. LevMar is allowed to tune at most five variables: $L_1 = L_5$, $L_2 = L_4$, $V_1 = V_5$, $V_2 = V_4$, and V_3 . As expected with a nonlinear fitter, the more constraints, the faster the fit and the more reasonable the resulting lengths and voltages. Sometimes a good fit can be obtained in seconds using only three electrodes of 1" length. For more anharmonic wells, more flexibility is required, and the fit can take up to a minute to converge, if it converges at all for the initial guess and parameter bounds chosen. For some asymmetric wells it was also necessary to allow $V_2 \neq V_4$. Typical results are shown in Fig. C.3.

Bibliography

- [1] M. Affolter et al. “Cyclotron mode frequency shifts in multi-species ion plasmas”. In: *Phys. Lett. A* 378 (2014), p. 2406.
- [2] Michael Ahmadi et al. “An improved limit on the charge of antihydrogen from stochastic acceleration”. In: *Nature* 529.7586 (2016), p. 373.
- [3] Michael Ahmadi et al. “Observation of the 1S–2S transition in trapped antihydrogen”. In: *Nature* 541.7638 (2017), p. 506.
- [4] M Ahmadi et al. “Enhanced control and reproducibility of non-neutral plasmas”. In: *Physical review letters* 120.2 (2018), p. 025001.
- [5] M Ahmadi et al. “Observation of the 1S–2P Lyman- α transition in antihydrogen”. In: *Nature* 561.7722 (2018), p. 211.
- [6] M Ahmadi et al. “Observation of the hyperfine spectrum of antihydrogen”. In: *Nature* 548.7665 (2017), p. 66.
- [7] C Amole et al. “In situ electromagnetic field diagnostics with an electron plasma in a Penning–Malmberg trap”. In: *New Journal of Physics* 16.1 (2014), p. 013037.
- [8] F. Anderegg, E. M. Hollman, and C. F. Driscoll. “Rotating Field Confinement of Pure Electron Plasmas Using Trivelpiece-Gould Modes”. In: *Physical review letters* 81 (1998), p. 4875.
- [9] F Anderegg et al. “Test particle transport due to long range interactions”. In: *Physical review letters* 78.11 (1997), p. 2128.
- [10] David Robert Bates, AE Kingston, and RW Pt McWhirter. “Recombination between electrons and atomic ions, I. Optically thin plasmas”. In: *Proceedings of the Royal Society of London. Series A. Mathematical and Physical Sciences* 267.1330 (1962), pp. 297–312.
- [11] B. R. Beck. “Measurement of the Magnetic and Temperature Dependence of the Electron-Electron Anisotropic Temperature Relaxation Rate”. PhD thesis. University of California, San Diego, 1990.
- [12] B. R. Beck, J. Fajans, and J. H. Malmberg. “Measurement of Collisional Anisotropic Temperature Relaxation in a Strongly Magnetized Pure Electron Plasma”. In: *Physical review letters* 68 (1992), p. 317.

- [13] William Alan Bertsche. “Direct excitation of kinetic, nonlinear electron-hole BGK waves in a non-neutral electron plasma”. PhD thesis. University of California, Berkeley, 2007.
- [14] Lowell S Brown and Gerald Gabrielse. “Geonium theory: Physics of a single electron or ion in a Penning trap”. In: *Reviews of Modern Physics* 58.1 (1986), p. 233.
- [15] Celeste Carruth. “Methods for Plasma Stabilization and Control to Improve Antihydrogen Production”. PhD thesis. 2018.
- [16] DB Cassidy, SHM Deng, and AP Mills Jr. “Noisy emission of a slowly released single component plasma”. In: *Nuclear Instruments and Methods in Physics Research Section B: Beam Interactions with Materials and Atoms* 248.1 (2006), pp. 121–126.
- [17] A. Christensen and The ALPHA Collaboration. “Patch Potential Induced Particle Loss in a Penning-Malmber Trap”. 2019.
- [18] B.P. Cluggish, J.R. Danielson, and C.F. Driscoll. “Resonant Particle Heating of an Electron Plasma by Oscillating Sheaths”. In: *Physical review letters* 81 (1998), p. 353.
- [19] D. L. Eggleston and T. M. O’Neil. “Theory of Asymmetry-Induced Transport in a Non-neutral Plasma”. In: *The Physics of Plasmas* 6 (1999), p. 2699.
- [20] J. R. Danielson and C. M. Surko. “Torque-balanced high-density steady states of single-component plasmas”. In: *Physical review letters* 94 (2005), p. 0305001.
- [21] JR Danielson et al. “Plasma and trap-based techniques for science with positrons”. In: *Reviews of Modern Physics* 87.1 (2015), p. 247.
- [22] Ronald C Davidson. *Physics of nonneutral plasmas*. Imperial College Press London, 2001. ISBN: 978-1860943034.
- [23] Steven Derenzo et al. *Scintillation Properties*. <http://scintillator.lbl.gov/>. 2019.
- [24] S Di Domizio et al. “Toward sub-Kelvin resistive cooling and non destructive detection of trapped non-neutral electron plasma”. In: *Journal of Instrumentation* 10.01 (2015), P01009.
- [25] Robert H Dicke. “Coherence in spontaneous radiation processes”. In: *Physical review* 93.1 (1954), p. 99.
- [26] DHE Dubin and TM O’Neil. “Cross-magnetic-field heat conduction in non-neutral plasmas”. In: *Physical review letters* 78.20 (1997), p. 3868.
- [27] DuPont. *Kapton, Summary of Properties*. <https://www.dupont.com/content/dam/dupont/products-and-services/membranes-and-films/polyimide-films/documents/DEC-Kapton-summary-of-properties.pdf>. Accessed: 2019-07-27. 2017.
- [28] D. Durkin and J. Fajans. “Experiments on two-dimensional vortex patterns”. In: *Physics of Fluids* 12 (2000), p. 289.
- [29] D. L. Eggleston et al. “Parallel Energy Analyzer for Pure Electron Plasma Devices”. In: *Physics of Fluids B* 4 (1992), p. 3432.

- [30] L. T. Evans. “Phenomenology of creation of antihydrogen and measurement of anti-hydrogen properties”. PhD thesis. University of California, Berkeley, 2016.
- [31] Nathan Evetts. “Cavity cooling of leptons for increased antihydrogen production at ALPHA”. MA thesis. University of British Columbia, 2015.
- [32] N. Evetts et al. “Open Microwave Cavity for use in a Purcell Enhancement Cooling Scheme”. In: *Rev. Sci. Instrum.* 87 (2016), p. 104702.
- [33] J Fajans. “Non-neutral plasma equilibria, trapping, separatrices, and separatrix crossing in magnetic mirrors”. In: *Physics of Plasmas* 10.5 (2003), pp. 1209–1214.
- [34] J. Fajans and L. Friedland. “Autoresonant (nonstationary) excitation of a pendulum, Plutinos, plasmas and other nonlinear oscillators”. In: *Am. J. Phys.* 69 (2001), pp. 1096–1102.
- [35] X Feng et al. “Tank circuit model applied to particles in a Penning trap”. In: *Journal of applied physics* 79.1 (1996), pp. 8–13.
- [36] Richard Feynman. *Feynman lectures on gravitation*. CRC Press, 2003.
- [37] L. Friedland and Shagalov. “Autoresonant Phase-Space Holes in Plasmas”. In: *Physical review letters* 96 (2006), 225001–1:4.
- [38] T. P. Friesen. “Probing Trapped Antihydrogen: In Situ Diagnostics and Observations of Quantum Transitions”. PhD thesis. University of Calgary, 2014.
- [39] T. Friesen et al. “Microwave-plasma interactions studied via mode diagnostics in ALPHA”. In: *Hyperfine Int.* 212 (2012).
- [40] Gerald Gabrielse and Hans Dehmelt. “Observation of inhibited spontaneous emission”. In: *Phys. Rev. Lett.* (1985).
- [41] Gerald Gabrielse and Hans Dehmelt. “Observation of inhibited spontaneous emission”. In: *Physical review letters* 55.1 (1985), p. 67.
- [42] V. Gorgadze. “Non-neutral Plasmas: Injection, Instabilities and Control”. PhD thesis. U. C. Berkeley, 2005.
- [43] Roy W Gould and Michael A LaPointe. “Cyclotron resonance in a pure electron plasma column”. In: *Physical review letters* 67.26 (1991), p. 3685.
- [44] C. Hansen and J. Fajans. “Dynamic and Debye Shielding and Antishielding in Magnetized, Collisionless Plasmas”. In: *Physical review letters* 74 (1995), p. 4209.
- [45] David N Hill, Steven Fornaca, and Michael G Wickham. “Single frequency scanning laser as a plasma diagnostic”. In: *Review of Scientific Instruments* 54.3 (1983), pp. 309–314.
- [46] EM Hollmann, F Anderegg, and CF Driscoll. “Measurement of Cross-Magnetic-Field Heat Transport in a Pure Ion Plasma”. In: *Physical review letters* 82.24 (1999), p. 4839.
- [47] MH Holzscheiter. “Cooling of particles stored in electromagnetic traps”. In: *Physica Scripta* 1988.T22 (1988), p. 73.

- [48] Joseph D Huba. *NRL plasma formulary*. Tech. rep. Naval Research Lab, Washington D.C., 2006, pp. 32–35.
- [49] J. E. Huffman, M. L. Snodgrass, and F. J. Blatt. “Magnetoresistance of copper, gold, and indium”. In: *Phys. Rev. B* 23 (2 Jan. 1981), pp. 483–488.
- [50] E. D. Hunter et al. “Electron Cyclotron Resonance (ECR) Magnetometry with a Plasma Reservoir”. arXiv:1912.04358. 2019.
- [51] E. D. Hunter et al. “Low magnetic field cooling of lepton plasmas via cyclotron-cavity resonance”. In: *Physics of Plasmas* 25.1 (2018), p. 011602.
- [52] E. D. Hunter et al. “Plasma Temperature Measurement with a Silicon Photomultiplier”. arXiv:1912.? (not yet published). 2020.
- [53] A. W. Hyatt, C. F. Driscoll, and J. H. Malmberg. “Measurements of the Anisotropic Temperature Relaxation Rate in a Pure Electron Plasma”. In: *Physical review letters* 59 (1987), p. 2975.
- [54] J.D. Jackson. *Classical Electrodynamics*. 3rd. John Wiley & Sons, Inc, 1999.
- [55] Martina Knoop, Niels Madsen, and Richard C Thompson, eds. *Physics with Trapped Charged Particles: Lectures from the Les Houches Winter School*. Imperial College Press, 2014.
- [56] Martina Knoop, Niels Madsen, and Richard C Thompson, eds. *Trapped Charged Particles - A Graduate Textbook with Problems and Solutions*. World Scientific, 2016.
- [57] Jacob W. Kooi. *Cryogenic Properties of Various Useful Materials*. <http://www.submm.caltech.edu/cso/receivers/thermal/properties.html>. Accessed: 2019-07-27. 2001.
- [58] J.M. Kriesel and C.F. Driscoll. “Two Regimes of Asymmetry-Induced Transport in Non-neutral Plasmas”. In: *Physical review letters* 85 (2000), p. 2510.
- [59] W B Kunkel. “Hall effect in a plasma”. In: *American Journal of Physics* 49.8 (1981), pp. 733–738.
- [60] Eugene Kur. Personal Communication. 2019.
- [61] William M MacDonald, Marshall N Rosenbluth, and Wong Chuck. “Relaxation of a system of particles with Coulomb interactions”. In: *Physical Review* 107.2 (1957), p. 350.
- [62] J. H. Malmberg and J. S. deGrassie. “Properties of a Nonneutral Plasma”. In: *Physical review letters* 35 (1975), p. 577.
- [63] J. H. Malmberg and T. M. O’Neil. “The Pure Electron Plasma, Liquid, and Crystal”. In: *Physical review letters* 39 (1977), p. 1333.
- [64] JH Malmberg et al. “Experiments with pure electron plasmas”. In: *AIP Conference Proceedings*. Vol. 175. 1. AIP. 1988, pp. 28–74.

- [65] Stephan Maury et al. “ELENA: the extra low energy antiproton facility at CERN”. In: *Hyperfine Interactions* 229.1-3 (2014), pp. 105–115.
- [66] T. B. Mitchell et al. “Mode and transport studies of laser-cooled ion plasmas in a Penning trap”. In: *AIP Conference Proceedings* 457.1 (1999), pp. 309–318.
- [67] JD Moody and JH Malmberg. “Free expansion of a pure electron plasma column”. In: *Physical review letters* 69.25 (1992), p. 3639.
- [68] J. Notte et al. “Experimental Breaking of an Adiabatic Invariant”. In: *Physical review letters* 70 (1993), p. 3900.
- [69] T. M. O’Neil. “Cooling of a Pure Electron Plasma by Cyclotron Radiation”. In: *Physics of Fluids* 23 (1980), p. 725.
- [70] T. M. O’Neil and P. G. Hjorth. “Collisional Dynamics of a Strongly Magnetized Pure Electron Plasma”. In: *Physics of Fluids* 28 (1985), p. 3241.
- [71] Christian G Parthey et al. “Improved measurement of the hydrogen 1 s–2 s transition frequency”. In: *Physical review letters* 107.20 (2011), p. 203001.
- [72] S Peil and G Gabrielse. “Observing the quantum limit of an electron cyclotron: QND measurements of quantum jumps between Fock states”. In: *Physical Review Letters* 83.7 (1999), p. 1287.
- [73] Federico Peinetti. “Large-Amplitude BGK Modes in Pure Electron Plasmas”. PhD thesis. Politecnico di Torino, 2005.
- [74] P Petit, M Desaintfuscien, and C Audoin. “Temperature dependence of the hydrogen maser wall shift in the temperature range 295-395 K”. In: *Metrologia* 16.1 (1980), p. 7.
- [75] A. P. Povilus. Personal Communication. 2014.
- [76] A. P. Povilus. “Cyclotron-cavity mode resonant cooling in single component electron plasmas”. PhD thesis. University of California, Berkeley, 2015.
- [77] A. P. Povilus et al. “Electron Plasmas Cooled by Cyclotron-Cavity Resonance”. In: *Phys. Rev. Lett.* 117 (2016), p. 175001.
- [78] SA Prasad and TM O’Neil. “Waves in a cold pure electron plasma of finite length”. In: *The Physics of Fluids* 26.3 (1983), pp. 665–672.
- [79] E. M. Purcell. “Spontaneous Emission Probabilities at Radio Frequencies”. In: *Proceedings of the American Physical Society*. Vol. 69. American Physical Society. 1946, p. 681.
- [80] Francis J. Robicheaux et al. “Theory and simulation of magnetized plasmas cooled by resonant interaction with a microwave cavity”. 2019.
- [81] E. Sarid, F. Anderegg, and C. F. Driscoll. “Cyclotron resonance phenomena in a non-neutral multispecies ion plasma”. In: *Physics of Plasmas* 2.8 (1995), pp. 2895–2907.
- [82] William Shockley. “Currents to conductors induced by a moving point charge”. In: *Journal of applied physics* 9.10 (1938), pp. 635–636.

- [83] James C Simpson et al. “Simple analytic expressions for the magnetic field of a circular current loop”. In: (2001).
- [84] C. Smorra et al. “A reservoir trap for antiprotons”. In: *International Journal of Mass Spectrometry* 389 (2015), pp. 10–13. ISSN: 1387-3806.
- [85] Lyman Spitzer. *Physics of fully ionized gases*. 1962.
- [86] J Tan and G Gabrielse. “Synchronization of parametrically pumped electron oscillators with phase bistability”. In: *Physical review letters* 67.22 (1991), p. 3090.
- [87] M. D. Tinkle, R. G. Greaves, and C. M. Surko. “Low-order longitudinal modes of single-component plasmas”. In: *Physics of Plasmas* 2.8 (1995), pp. 2880–2894.
- [88] M. D. Tinkle et al. “Low-order modes as diagnostics of spheroidal non-neutral plasmas”. In: *Phys. Rev. Lett.* 72 (1994), p. 352.
- [89] Stefan Ulmer et al. “The quality factor of a superconducting rf resonator in a magnetic field”. In: *Review of Scientific Instruments* 80.12 (2009), p. 123302.
- [90] Simon Van Der Meer. “Stochastic cooling and the accumulation of antiprotons”. In: *Reviews of Modern Physics* 57.3 (1985), p. 689.
- [91] G. Vandoni. *The Basis of Vacuum – CERN Basic Vacuum 2012 Lecture*. <https://www.scribd.com/presentation/347263083/CERN-Basic-Vacuum-2012-Lecture.2012>.
- [92] M Vogel et al. “Resistive and sympathetic cooling of highly-charged-ion clouds in a Penning trap”. In: *Physical Review A* 90.4 (2014), p. 043412.
- [93] W8JI. *Loading Inductors*. https://www.w8ji.com/loading_inductors.htm. c. 2010.
- [94] T. R. Weber, J. R. Danielson, and C. M. Surko. “Creation of finely focused particle beams from single-component plasmas”. In: *Physics of Plasmas* 15.1 (2008), p. 012106.
- [95] Robert Wilson. *Propagation Losses through Common Building Materials*. https://www.am1.us/wp-content/uploads/Documents/E10589_Propagation_Losses_2_and_5GHz.pdf. 2002.
- [96] D. J. Wineland and H. G. Dehmelt. “Principles of the stored ion calorimeter”. In: *Journal of Applied Physics* 46.2 (1975), pp. 919–930.